ABSTRACT

MULTI-FUNCTIONAL, SELF-SENSING AND AUTOMATED REAL-TIME NON-CONTACT LIQUID DISPENSING SYSTEM

by
Qiong Shen

Liquid dispensing in the order of pico-liter has become more and more important in biology, electronics and micro-electronic-mechanical-system (MEMS) during the past two decades due to the rapid progress of researches on the deoxyribonucleic acid (DNA) microarray, compact and low-cost direct write technology (DWT), organic semiconductors and nano-particles.

The existing approaches, commercialized or experimental, to liquid dispensing in minute amounts have one common shortcoming: open loop control, i.e., they have no direct control on the quality of dispensed liquid. In contrast, the SmartPin has intrinsic self-sensing capability to not only control the process of liquid dispensing, but also the results of the dispensed liquid in real time. The dual purpose fiber optics sensor/plunger is able to detect the status of liquid morphology under dispensing, in real time, by the internal light sensor and control both the amount and the manner of liquid dispensing by its plunger-like movements.

This dissertation work has implemented, with the SmartPin technology, a fully automated DNA microarrayer based on the first generation prototype developed at NJIT's Real Time Control Laboratory. This new DNA microarrayer fulfills all requirements in each step of DNA microarray fabrication, such as thorough cleaning to avoid cross contamination and clogging, aspiration of tiny amount of DNA samples, spotting on multiple slides, and flexible in stream change of DNA samples. Experiment

results shows that this DNA microarrayer compares favorably with its commercialized counterpart OmniGrid 100 with SMP3 pins. As a verification of robust implementation and on-the-fly control of spot morphology, high volume of spots (120 K) have been made, from which the corresponding experiment data has been obtained, categorized and normalized as template database. In addition, this dissertation research explores the patterned microline-drawing capability of the SmartPin. Two approaches, spot sequence and liquid-column sweeping, are proposed and implemented. Experiment results show that the SmartPin is promising in the area of patterning of large area organic electronics. Besides the experimental research, computational fluid dynamics (CFD) simulation of the liquid dispensing process has been done by utilizing GAMBIT and FLUENT, which are state-of-the-art computer programs for modeling fluid flow and heat transfer in complex geometries. The CFD simulation results, validated by experimental results, offer a guide to the design of control system for different tasks of liquid dispensation, such as fabrication of protein microarray.

MULTI-FUNCTIONAL, SELF-SENSING AND AUTOMATED REAL-TIME NON-CONTACT LIQUID DISPENSING SYSTEM

by
Qiong Shen

A Dissertation
Submitted to the Faculty of
New Jersey Institute of Technology
in Partial Fulfillment of the Requirements for the Degree of
Doctor of Philosophy in Mechanical Engineering

Department of Mechanical Engineering

August 2008

APPROVAL PAGE

MULTI-FUNCTIONAL, SELF-SENSING AND AUTOMATED REAL-TIME NON-CONTACT LIQUID DISPENSING SYSTEM

Qiong Shen

8/5/08

Dr. Zhiming Ji, Dissertation Co-Advisor — Date
Associate Professor of Mechanical Engineering, NJIT

8/5/2008

Dr. Timothy N. Chang, Dissertation Co-Advisor — Date
Professor of Electrical and Computer Engineering, NJIT

Dr. Rajpal S. Sodhi, Committee Member — Date
Professor of Mechanical Engineering, NJIT

8/5/08

Dr. Chao Zhu, Committee Member — Date
Professor of Mechanical Engineering, NJIT

8/5/08

Dr. Sui-hoi E. Hou, Committee Member — Date
Associate Professor of Electrical and Computer Engineering, NJIT

BIOGRAPHICAL SKETCH

Author: Qiong Shen

Degree: Doctor of Philosophy

Date: August 2008

Undergraduate and Graduate Education:

- Doctor of Philosophy in Mechanical Engineering,
  New Jersey Institute of Technology, Newark, NJ, 2008
- Master of Science in Mechatronics Engineering,
  Donghua University, Shanghai, P. R. China, 2002
- Bachelor of Science in Mechatronics Engineering,
  China Textile University, Shanghai, P. R. China, 1999

Major: Mechanical Engineering

Patent, Presentations and Publications:

Chang, T. N. & Shen, Q. (2007). Delivery and Sensing of Metered Amounts of Liquid Materials, Patent (pending).

Shen, Q., Ji, Z., & Chang, T. N. (2008). CFD simulation and prediction on liquid dispensing process with VOF multiphase model (in preparation).

Shen, Q., Chang, T. N., & Yu, L. (2008). Automated Real-Time Spotting System for DNA/Protein Microarray Applications, IEEE Transactions on Industrial Electronics, Vol. 55, (in press).

Shen, Q. & Chang, T. N. (2007). SmartPin: An automated liquid dispensing system, IEEE Seminar, NJIT, Newark, New Jersey.

Shen, Q. & Chang, T. N. (2007). Automated Multi-Function Liquid Handling System, BioTech '07 – A Joint Symposium of BioNJ & Pennsylvania Bio, Philadelphia, Pennsylvania.

Shen, Q. & Chang, T. N. (2007). SmartPin: An automated liquid dispensing system, The 4th Annual New Jersey Biomedical Engineering Showcase, Newark, New Jersey.

Shen, Q. & Chang T. N. (2007). SmartPin – An Automated Multi-Function Liquid Dispensing System, Proceedings of the 33rd Annual Conference of the IEEE Industrial Electronics Society (IECON'07), 2146-2151.

Shen, Q., Chang, T. N., & Yu, L. (2007). Automated Real-Time Spotting System for DNA/Protein Microarray Applications, Proceedings of the 2007 IEEE International Symposium on Industrial Electronics (ISIE'07), 281-286.

To my beloved father, Youlin Shen, mother, Mantian Wang, father in law, Anshi Qiu, mother in law, Guilin Zong, older brother, Bin Shen, twin sister, Jin Shen, and wife, Lili Qiu.

献给我至亲的父亲，申友林，母亲，王满田，岳父，仇安石，岳母，宗桂琳，兄，申斌，姊（与我为龙凤胎），申瑾，以及妻子，仇丽莉。没有你们始终如一的关怀和照顾，就没有我的今天。

ACKNOWLEDGMENT

I would like to express my earnest gratitude to Prof. Timothy N. Chang, who supported my research not only financially, but also academically and spiritually. Without his constant encouragements, ambitious vision and optimistic attitude on difficulties, I could not finish my research work. Beyond the academic achievements, I have also learned much about cooperation with others, organization of intertwined tasks and management of a group of persons from Prof. Chang's rich experiences in industry, management and professional careers. Special thanks are given to Dr. Zhiming Ji for advising and guiding me in the research on computational fluid dynamics (CFD) simulation. Also, I would like to thank Dr. Rajpal S. Sodhi, Dr. Chao Zhu and Dr. Sui-hoi E. Hou for actively participating in my dissertation committee, and Dr. Herli Surjanhata for constantly giving me hints on how to use CFD softwares effectively.

This dissertation work is supported in part by National Science Foundation Grant 0243302, "High Resolution, High Density Microarrays for Genetic Research", and a New Jersey Commission on Science & Technology gap fund.

All of my fellow graduate students in the Real-Time Control Laboratory, Dr. Biao Cheng, Dr. Ding Yuan, Suganya Parthasarathy, and Lan Yu are deserving of recognition for creating a friendly and harmonic environment of the lab.

Last but not least, I give my thanks to my beloved wife, Lili Qiu who always supports me with her love and understanding in my daily life.

TABLE OF CONTENTS

TABLE OF CONTENTS
(Continued)

Chapter **Page**

TABLE OF CONTENTS
(Continued)

Chapter **Page**

LIST OF TABLES

LIST OF FIGURES

LIST OF FIGURES
(Continued)

LIST OF FIGURES
(Continued)

LIST OF FIGURES
(Continued)

CHAPTER 1

INTRODUCTION

1.1 Objective

The last two decades have witnessed dramatic improvements in researches on DNA/protein microarray, organic electronics and nanotechnology which have profound impacts on our society. Although there exist many approaches to support the operations of such research effort, a critical step: pico-liter level liquid handling; has not been implemented satisfactorily to fulfill many important requirements for industry automation and applications. Such requirements include real time dispensation quality analysis and control, low cost of manufacturing, operations and maintenance. Furthermore, most of the current dispensing technologies are essentially open loop operations that suffer from the inherent limitations associated with open loop processes. The SmartPin technology is devised to overcome this issue through the self-sensing and active metering of liquid volume via a plunger-like optical fiber sensor assembly. With proper real-time hardware and software control, this SmartPin technology can be realized as a low-cost, multifunctional, closed looped and automated real-time liquid dispensing system.

The objective of this dissertation is to implement, with the SmartPin technology, a fully automated DNA microarrayer on top of the primary prototype done by Suganya Parthasarathy in 2005 and Timothy N. Chang et al. in 2006. As an alternative to commercialized DNA microarrayer, this new DNA microarrayer should fulfill all requirements in each step of DNA microarray fabrication, such as thorough cleaning to avoid cross contamination and clogging, aspiration of tiny amount of DNA samples, spotting on multiple slides, and change of DNA samples without interrupt. Experiment

results under comparable environment are required to compare this new DNA microarrayer with its commercialized counterpart OmniGrid 100 with SMP3 pins. To prove it is capable of not only quality control but also robust high volume throughput, spotting experiments for high volume of spots is to be carried out. Besides, exploration of the potentials of this self-sensing device, such as patterned microline-drawing capability is to be done. Two possible approaches, spot sequence and liquid-column sweeping, were proposed and are to be implemented. Beyond the experimental research, computational fluid dynamics (CFD) simulation of the liquid dispensing process is a less expensive way to guide the design of control system for different tasks of liquid dispensation, such as fabrication of protein microarray. The CFD simulation is to be done by utilizing Gambit and Fluent, which are state-of-the-art computer programs for modeling fluid flow and heat transfer in complex geometries.

1.2 Background

1.2.1 On the SmartPin Technology

The SmartPin technology is based on the invention: "Delivery of Metered Amounts of Liquid Materials" (Chang and Tolias in 2006) which teaches techniques utilizing a light transmissive pin, to deliver predetermined amounts of liquid materials onto a surface by means of integrated sensing and control.

Figure 1.1 illustrates the principle of such liquid delivery system. The positioning of the entire liquid delivery apparatus is accomplished by synergic control on the coupled three-degree-of-freedom (3-DOF) course stage, horizontal X-Y stage and vertical Z microstage. The vibration sensor coupled to the Z microstage offers feedback to

vibration suppression control. The subassembly of pin and the optical sensor, driven by the coupled pin actuator, slide vertically like a piston in the cylindrical bore in the housing. The pin includes an optical fiber with diameter in the range of 5 to 50 microns depending on factors such as the spot size of dispensed liquid material and the electrical characteristics of the optical sensor. The optical sensor not only generates light but also senses the light reflected from the target surface through the pin. The liquid material to be delivered is stored in the reservoir.

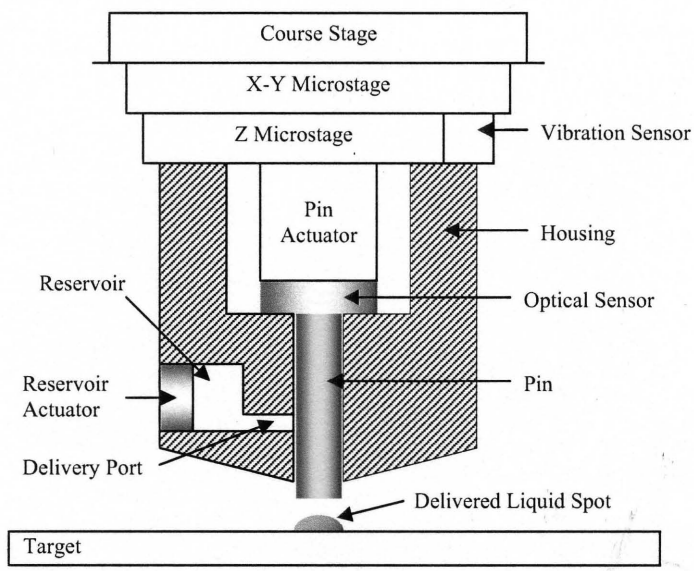

Figure 1.1 Cross section diagram of the liquid delivery system.

The delivery procedure is as follows:

- The apparatus is positioned to the desired distance above the target spot (determined by signal level of the optical sensor).
- The pin is pulled upwards until the bottom of the pin is above the delivery port.
- Precisely metered amount of liquid material is pushed by the reservoir actuator into the cylindrical bore through the delivery port.
- The pin is pushed downwards towards the target surface without directly contacting the target surface: the liquid material adhered to the bottom of the pin contacts the target surface to form a spot.

- The pin can be driven by the pin actuator into high-frequency vibration to separate the liquid droplet from the pin tip if necessary.

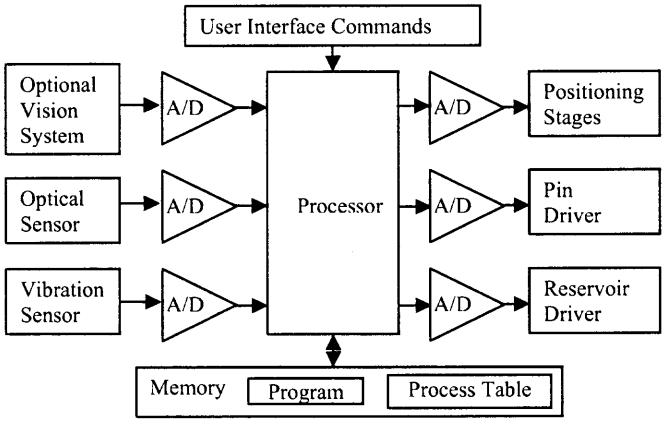

Figure 1.2 Control system for operation of the liquid delivery system.

Shown in Figure 1.2 is the block diagram of the control system of the liquid delivery process. The process table includes light intensity data corresponding to different time intervals which the processor can use during a process cycle to determine the position of the pin.

Due to the complexity and novelty of this liquid delivery system, development of a prototype is a technologically challenge task. This doctoral research is supported by an NSF grant (Chang and Soteropolous 2003) for the development of such a prototype with fully automated operations. The proposed system is a new generation of microarray spotter capable of depositing aqueous samples of various types (DNA, protein, etc.). The system has the flexibility and cost advantage of the printing approach, and can be operated remotely via the Internet. The key enabling features include a composite piezoelectric device with nanometer precision in spot size and position.

The prototype developed Suganya Parthasarathy in 2005 and Timothy N. Chang et al. in 2006 is extended and improved in this dissertation work and will be studied in Chapter 2.

1.2.2 Applications of the SmartPin

A major advantage of the SmartPin is it self-sensing capability which translates into contactless dispensation. Not having the pin come into contact with the target surface avoids expensive replacement and maintenance of pin as in the conventional contacting printing pins. Moreover, the size and morphology of the delivered liquid spot can be easily controlled by using microstages to control the operation of the pin and the precise position of the pin over the target surface. This makes possible the efficient and economic use of precious liquid materials. Such techniques can be applied to the areas of microarrays, microscopic markers, micro-surgery or pharmaceutical processing and drug discovery manipulations.

1.2.2.1 On the Microarray Technology. Since the discovery of the double-helical structure of DNA, which laid the foundation for all hybridization based technologies, a series of discoveries and inventions have propelled our knowledge from the recognition that DNA is the genetic material to a basic molecular understanding of ourselves and the living world around us. The discoveries of restriction enzymes, ligases, polymerases, combined with key innovations in DNA synthesis and sequencing ushered in the era of biotechnology as a new science with profound sociological and economic implications.

Medical researchers and biologists have long recognized the tremendous genotypic and phenotypic heterogeneities in biological systems. Genotype-phenotype

correlation studies have attempted to link characteristics as a basis for translating findings into practical applications, including individualized diagnosis and therapy. In the past, technology and methodology addressed only individual candidate genes or small groups of genes; global genotype-phenotype correlation was not possible.

A major opportunity to achieve the goal of individualization appeared with the development of high throughput genomic technologies, especially microarrays, with which thousands of genes can be evaluated simultaneously to generate a transcriptome profile or portrait for each individual. Now the aim is to establish a correlation between these genetic portraits and specific phenotypes, such as propensity for certain diseases or the response of a disease to treatment. In recognition of the opportunity to fulfill this goal, many institutions and commercial entities have established genomics core facilities to produce microarrays and generate microarray data from biological materials.

Twelve years ago (Schena et al., 1995), microarray technology emerged as a new and powerful tool to study nucleic acid sequences in a highly multiplexed manner, and has since found equally exciting and useful applications in the study of proteins, metabolites, toxins, virtues, whole cells and even tissues. Although still relatively early in its evolution, microarray technology has already superseded the now well known Polymerase Chain Reaction (PCR) technology not only in the breadth of applications, but also in the speed with which this evolution has taken place. By allowing simultaneous measurement of the expression of thousands of genes, microarray technologies have marked a defining moment in biological research. Indeed, many publications have now shown the power of gene expression profiling in the diagnosis and prognosis of disease and the identification of gene targets. In conjunction with bioinformatic tools to process

and analyze the large amounts of data they generate, microarrays have spawned new approaches to systems biology described with the 'omics' suffix: genomics, transcriptomics, and proteomics etc.

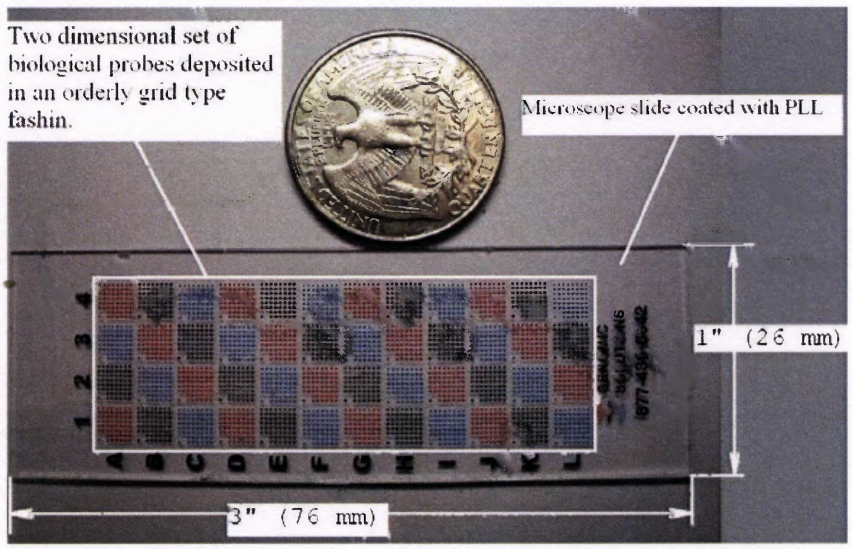

Figure 1.3 A typical microarray.

Traditionally, arrays have consisted of collections of distinct capture molecules – typically cDNAs or oligonucleotides – attached to a substrate – usually a glass slide – at predefined locations within a grid pattern. However, today's formats are more diverse and can be grouped into several categories. The classes of capture molecules used in microarrays include not only DNA, but also proteins (Schweitzer et al., 2002), carbohydrates (Love et al., 2002), drug-like molecules (Lam et al., 2002), cells (Wu et al., 2002), tissues (Fejzo et al., 2001) and the like.

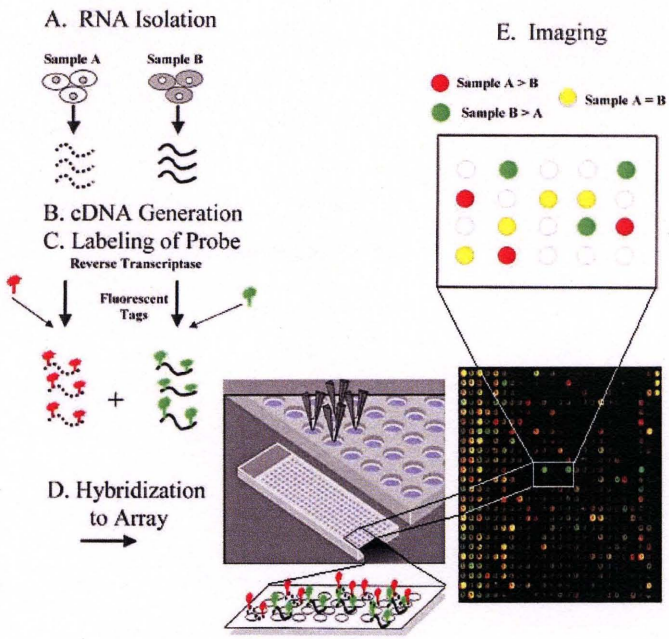

Figure 1.4 Procedures involved in microarray technology.
(Source: http://www.genome.gov/10000533)

Figure 1.4 illustrates the procedures involved in a complete microarray experiment. Once high-fidelity DNA (cDNA or long oligos) is available and cleanly coated slides are ready, microarrays are ready to be printed with a robotic printer or spotter. There are a number of different printers on the market and there are different issues specific to each approach.

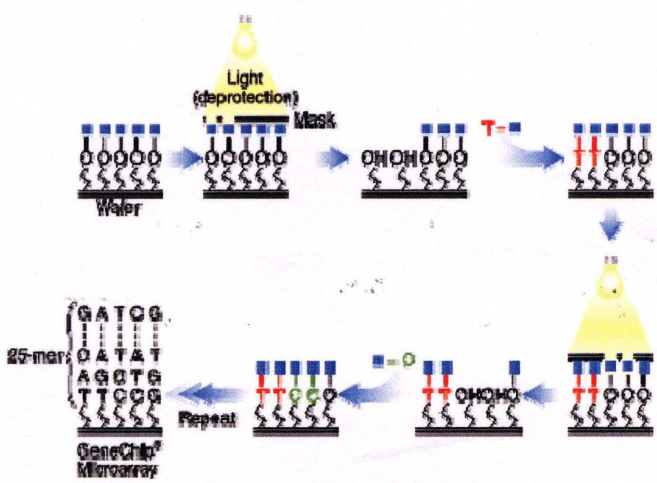

Figure 1.5 Procedures of Affymetrix GeneChip production.
(Source: http://www.affymetrix.com/technology/manufacturing/index.affx)

Affymetrix GeneChip microarray is produced by a photolithographic process in which semiconductor fabrication techniques, solid phase chemistry, combinatorial chemistry, molecular biology, and sophisticated robotics are integrated (Figure 1.5). The first step is coating a 5″ x 5″ quartz wafer with a light-sensitive chemical compound. The coated wafer is exposed to light which is grated by lithographic masks. The surface is then flooded with a solution containing either adenine, thymine, cytosine, or guanine. The coupling between nucleotide and the surface only occurs in those regions that have been exposed to illumination. Since the nucleotides also bear a light-sensitive protection the microarray is built as the probes are synthesized through repeated cycles of light-exposure and coupling. Commercially available arrays are typically manufactured at a density of over 1.3 million unique features per array. Each quartz wafer may need to be diced into tens or hundreds of individual arrays according to the demands of the experiment and the number of probes required per array. Although it can make very high density microarrays, the process is expensive and inflexible for small to medium sized research lab or institute.

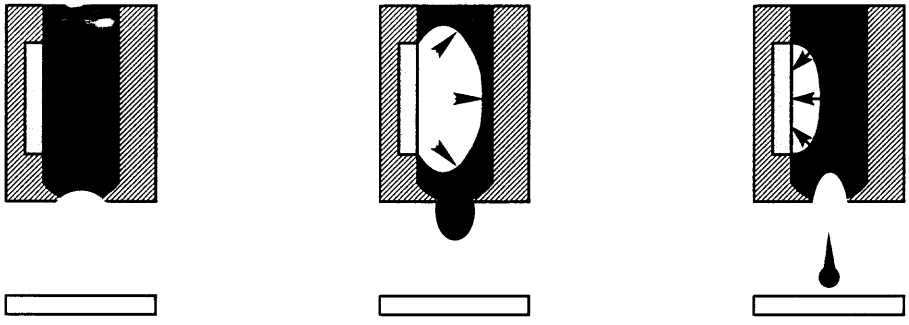

(a) (b) (c)

Figure 1.6 Thermal-based jets.

Reagen Jetting techniques borrow features and technology developed for commonly used ink jet based desktop printers (Le, 1998). These printers are typically drop-on-demand devices that use thermal, piezo or solenoid based actuation mechanisms.

Thermal jets, often referred to as bubble jet, eject droplet by superheating a small volume of liquid near the dispensing orifice (Figure 1.6). Typically, a resistive heating element is controlled such that the application of current causes rapid heating of the liquid. This generates a vapor bubble, forcing liquid from the nozzle (Figure 1.6(b)). Upon cooling, the bubble collapses, pinching the liquid stream and allowing for the channel to refill (Figure 1.6(c)). Successful examples of adapting commercial printers for dispensing DNA or protein solutions have been published. The printed spots can be as small as few tens of microns with consistent dispensed volume of a few tens of picoliters. Nevertheless, the ink cartridge must be carefully rinsed out and replaced with the biochemical in a solution of similar viscosity and surface tension as the original ink. As such, addition of various reagents such as ethanol (de Wildt et al., 2000), glycerol (Hughes et al., 2001) or a detergent such as sodium dodecyl sulfate (Hicks et al., 2001) is required. Furthermore, the rapid heating, which can reach temperature of 200-300 degrees Celsius, could cause protein degradation and low protein activity. Clogging of the nozzle is another problem involved in using this approach.

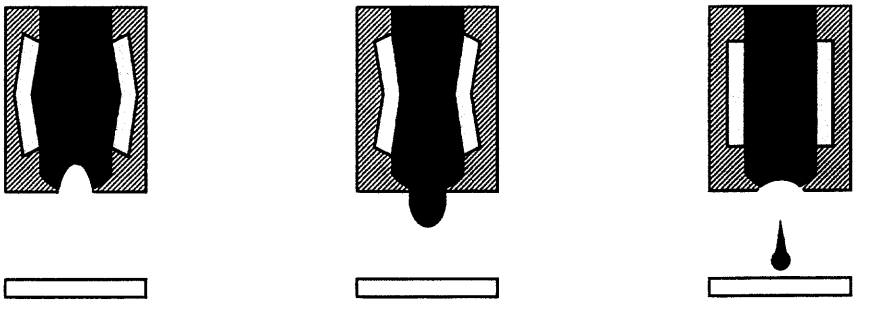

Figure 1.7 Piezo-based jets.

Piezo-based jet operates by mechanically inducing a pressure wave into the liquid. Rapid dimensional changes of a piezoelectric material can induce this pressure pulse to eject a single droplet (Figure 1.7). In contrast to thermal jet printers, single channel piezo-based dispensers are commercially available for applications other than desktop printing. A number of different designs are employed in desktop printers, with the piezoelectric material operating in either a push, pull, shear or squeeze tube mode (Roda et al., 2000). Instruments or components from manufacturers such as MicroFab Technologies, Microdrop GmbH, and Perkin Elmer Life Sciences are commonly used for biomedical applications including microarray construction. The printed spots are on the order of tens of microns in diameter and hundreds of picoliters in volume when dispensed onto a glass slide (Blanchard et al., 1996). However, the dispense nozzle must be filled with the desired reagent and a specific fluid pressure must be maintained for dispensing. Appropriate pressure in the fluid tube is necessary for preventing the reagent from dripping out the nozzle and for optimal performance of the device. Further, small nozzle diameters can lead to clogging.

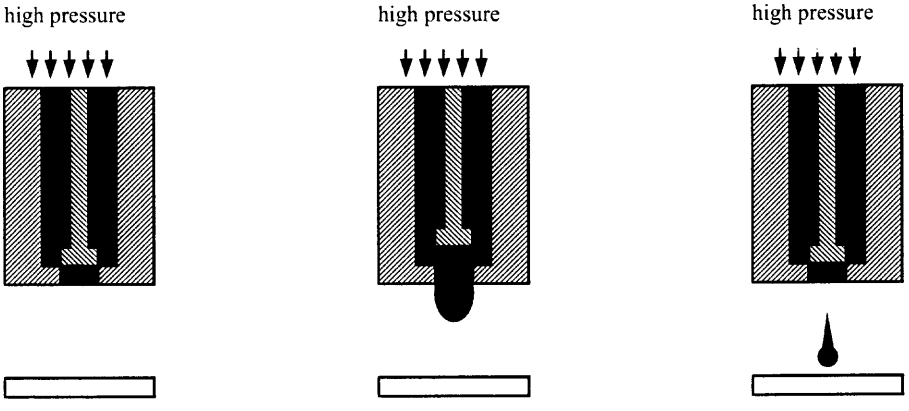

Figure 1.8 Solenoid-based jets.

Unlike the aforementioned jetting techniques which function as fluid pumps, the solenoid-based technique exploits high speed valves. In operation, the valve is positioned between a pressurized fluid source and a nozzle (Figure 1.8). Rapid actuation of the valve causes fluid to stream from the nozzle. Several fluid dispensing devices based on solenoid valve technology have been reported by Papen et al., 1998, Valvert, 2001, and Cooley et al., 2001 etc.Commercial systems based on solenoid valve technology are available from Cartesian Engineering and Innovadyne Technologies. Although the system can be used for microarraying, the typical lower limit on droplet volume (~ 1 nanoliter) is too large to produce high density microarrays. When used as a reagent dispenser, care must be taken not to expose the valve to harsh solvents as this can lead to degradation of the valve seals.

Impact Pin-Based printing technologies deliver certain volumes of biological materials to a substrate with pins, hollow needles or capillaries (Figure 1.9) by means of contact or tapping between the transfer device (pin) and the receiving surface (substrate). Commonly used pins include solid pins, ring and pin (used on Affymetrix GMS417), micro-fabricated pin array (from Corning), split or quill pin, stealth pin from TeleChem, Hitachi X-cut pin, capillary pin (from Genomic Solutions), massively parallel fiber-optic capillary (from GenoSpectra), and disposable pins (from VP-Scientific). One disposition starts with dipping the pin into the liquid material reservoir. An impact between the pin tip and the substrate surface forces the liquid in the pin onto the substrate surface. The spot is formed when the pin moves away from the substrate pinching off the liquid.

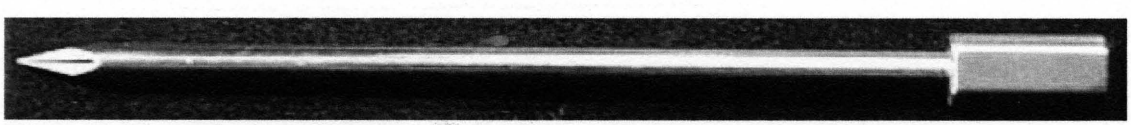

Figure 1.9 A typical capillary pin.

While the pin is the core of an impact pin-based printing system, other system components and environmental factors influence its reliability and reproducibility. Proper monitoring, maintenance, calibration and minor adjustments of these can make the difference between optimal performance and bad arraying. Key factors include pin holders, multiple pins, environmental control, positional robotic control, and washing system. Despite the fact that this technique has been popular, there are still some unsolved problems involved. The over-immersion of the pin in sample reservoir will result in loading too much sample. It can also lead to unwanted carry-over in subsequent cycles. Due to the nature of impact, the substrate must be hard enough to sustain the impact, and there is inevitable damage on the substrate surface, the tip of the pin and even the biological samples. Clogging of the orifice of the pin is another big problem.

1.2.2.2 On Large Area Electronics. Over the past two decades, development of constantly smaller and tighter packed components has become the need-driven trend in electronics manufacturing. Alongside this trend is the increasing importance of low cost in determining commercial success and marketability in many electronic devices, such as large area displays, radio frequency identification (RFID), adaptive distributed antennas, etc. Since these electronic devices require either a large area substrate or flexibility, polymeric materials have advantages over expensive and hard, rigid substrates, such as silicon and quartz. In addition, it is important to fabricate low resistance conductors because the signal has to propagate a long distance and RC delays should be minimized (Chung et el. in 2005).

Take cellular phone manufacturers as example, they are continuously striving to improve capital utilization, to reduce downtime associated with changeover and to obtain higher yields and output of their products (Szczech et el. in 2002).

Corresponding to these requirements, additive process using direct write technologies (DWT) has gained significant interest as an alternative approach to conventional, subtractive integrated circuit (IC) processes (Szczech et el. in 2002). In the additive process, either thin organic semiconductor film polymer is deposited onto insulator (dielectric) layer or nanoparticles were deposited onto polymer substrate.

Since Tsumura et al. (1986) demonstrated the first organic field-effect transistor (FET), there has been tremendous progress in the field of organic electronics with thin-film transistor (TFT). All-organic and all-polymer transistor circuits with a performance suitable for certain applications have been demonstrated by Jackson et al. (1998), Gelinck et al. (2000), Edzer et al. (2002), Crone et al. (2002). Although the reported performance of organic transistors is still considerably lower compared to that of silicon transistors, a new market is open for organic devices, where the excellent performance of silicon technology is not required. Such commercial applications include: flat panel display (FPD) based on organic light emitting devices (OLEDs), biosensors, solar cells, cell phones, computerized clothing, laptops, luggage tags, digital cameras, radio frequency identification (RFID) tags.

The biggest advantage of organic semiconductors, among others, is their intrinsically compatibility with low-cost processing. Being plastics, they combine the mechanical properties, such as flexibility, toughness, malleability elasticity, etc., of plastics with the high electrical conductivities. These properties have drawn increasing

interests from researchers and manufactures to do flexible prototyping and reduce manufacturing cost of electronics devices.

In addition, the emergence of consistent manufacturing methods of nanoparticles is creating a vivid activity related to the utilization of these particles. Several studies related to printing and curing of nanoink using a hot plate or a curing oven have been carried out. Since nanoparticles melt at low temperature, there is great potential for producing microconductors at low processing temperature suitable for polymeric substrate.

The existing technologies for the productions of electronics based on printing methods include microcontact, ink-jet printing, screen printing, thermal imaging, line patterning, and offset printing.

Microcontact printing (μCP) is based on the selective transfer of an organothiol or silane to a substrate via a flexible polymer stamp, thus resulting in exposed and covered regions of the substrate (Kumar and Whitesides in 1993). The stamp is usually fabricated by casting an elastromer solution on the master. After curing, the elastomeric stamp is peeled from the master, giving a negative replica of its surface topography. Etching, electroless plating or area-selective electropolymerization are three major ways for patterning flexible electronics after μCP (Wilbur et al. in 1994, Xia et al. in 1996).

μCP is a strong candidate for industrial patterning of source and drain electrodes with resolution in the range of 1-20 microns (Leufgen et al. in 2004). Although several approaches for automated sheet-to-sheet or reel-to-reel production process have been realized (Rogers et al. in 1999, Decre et al. in 2004, and Schellekens et al. in 2004), a problem in the automation of μCP could be the elastic modulus of the stamp and, as a

result, the limited applicable pressure on the stamp. Candidate materials must be robust, retaining their electrical properties through the numerous fabrication steps. In addition the material must be suitable for delivery to the substrate in a patterned high throughput mode eliminating many slow serial delivery methods and most postimaging processing.

Ink-Jet Printing technologies provide opportunities both for significant cost reduction in existing organic devices and for new device configurations (Hayes et al. in 2002). This method works the same way as in fabrication of DNA microarray described in section 1.2.2.1.

Rozenberg et al. (2002) successfully patterned low-temperature copper-rich deposits on glass substrates by using a piezoelectric drop-on-demand ink-jet print head. With the use of ink-jet printing techniques, TFTs with top-gate configuration (Kawase et al. in 2001), high-resolution patterning of an all-polymer TFT (Sirringhaus et al. in 2000), enhancement-load and resistor-load type inverters (Kawase et al. in 2001), both contact electrodes in the electronic devices and the semiconducting layer (Ridley et al. in 1999, Paul et al. in 2003, and Elrod et al. in 1989), high-quality conducting and dielectric films (Molesa et al. 2003) have been reported. The typical lateral resolution achievable with this method is in the range from 50 to several hundred microns though Elrod (1989) reported drops with diameter of only 5 microns.

Ink-jet printing makes easily possible printing of contacts, semiconductors, and dielectrics on large substrates. A common problem in ink-jet printing is clogging of the ejector or nozzle. For the thermal-type head, heat damage of the functional organic material is possible.

Screen Printing is a conventional printing process in which liquid materials are transferred by capillary action to the substrate surface through porous fabric (screen). Dhingra et al. (1991), Chung et al. (1995), and Valencia et al. (2003) investigated deposition of inorganic composites. The fabrication of organic TFTs has been reported by Gray et al. (2001), Garnier et al. (1994), Bao et al. (1997), and Knobloch et al. (2001).

With screen printing, patterning of both inorganic and organic layers is possible. Screen printing is disadvantageous from the viewpoint of resolution being restricted by the screen mesh (approximately 100 um and above).

Thermal imaging has been invested by Blanchet et al. (2003) and Lefenfeld et al. (2003). This method involves the pixelized transfer of a thin solid layer, encompassing a digital image, from a donor film onto a flexible receiver. The sequential transfer of images from different solid layers could be used to build multilayer devices. A 40 W 780 nm infrared diode laser, split into 250 2.7 mm35 mm individually addressable spots, is focused through the donor base at a thin metal layer. The efficient conversion of light to heat at this interface decomposes a thin layer of adjacent organics into gaseous products while heating and softening the remaining film. Their expansion of the gaseous decomposition products thus propels the thin conducting layer onto the receiver film. The desired conducting pattern is printed by selectively transferring the individual 5 mm32.7 mm pixels comprising the image from the donor layer onto the receiver.

Maintaining the conductivity of the composites throughout the laser driven printing process is difficult since deprotonation with loss of conductivity, occurs at fairly modest temperatures.

Line patterning (Lu et al. in 2002, and MacDiarmid in 2001) uses the different responses of a substrate and insulating lines which have been printed on it by a conventional copying or printing process towards a fluid (or vapor) to which they are both simultaneously exposed. The substrate and printed lines react differently or at different rates with the fluid (or vapor) to which they have been exposed. This results in a nonuniform deposition on the substrate as compared to the printed lines. If the fluid contains a conducting polymer, which remains as a film after evaporation of the solvent, a pattern of conducting polymer results. A pattern is first designed on a computer and is then printed on, for example, an overhead transparency using a standard, unmodified office laser printer. The printed (insulating) lines can be removed by ultrasonic treatment in toluene, dissolving the printed lines and leaving a clean pattern of deposited material on the substrate whose shape was originally defined by the now nonexistent printed lines.

Line patterning has the following advantages: no photolithography is involved; no printing of conducting polymer is involved; it uses only a standard office laser printer; commercially available flexible, transparent plastic or paper substrates can be used; solutions of commercially available conducting or nonconducting polymers can be used from which the polymers may be deposited on substrates; it is inexpensive; rapid development of customized patterns (within hours) from a computer-designed pattern to product is routine. Nevertheless, it is difficult to automate the whole process.

Offset Printing is a widely used printing technique where the inked image is transferred (or "offset") from a plate to a rubber blanket, then to the printing surface. When used in combination with the lithographic process (Mikami et al. in 1994, and Walton et al. in 1999), which is based on the repulsion of oil and water, the offset

technique employs a flat (planographic) image carrier on which the image to be printed obtains ink from ink rollers, while the non-printing area attracts a film of water, keeping the non-printing areas ink-free.

However, an offset printing ink must have a special chemical property, i.e., a selective affinity for the pattern on the intaglio, which narrows the range of transfer properties suited to fine pattern printing. Also, the resolution is not so high.

1.2.2.3 On Micro-Electro-Mechanical System (MEMS). Microfabrication of electronic and mechanical structure at the submillimeter scale is typically a time-consuming and expensive process. Lithographic techniques for silicon micromachining, used to fabricate integrated circuits and MEMS, typically take several weeks to go from drawings to completed chips, and require expensive facilities and extreme processing conditions. An alternate approach in which multiple small volumes of metallic, semiconducting, or insulating material are deposited at computer-defined positions could enable the all-additive fabrication of such devices on a much faster and less expensive basis.

Fuller et al. (2002) demonstrated the ability of ink-ject printing to build circuit-like devices and MEMS. Structures include a high-Q inductive resonant coil, linear and rotary electrostatic drive motors, and in-plane and vertical heatuators. The devices with a 100-micron feature size were made out of silver and gold material with high conductivity and feature as many as 400 layers, insulators, 10:1 vertical aspect ratios, and etch-released 3-D mechanical structure.

1.2.2.4 On Micro-Soldering. Solder dispensing, construction of three-dimensional ceramic structures (Lahiri et al., 2001). Techniques that involve expelling

small droplets of molten metal onto a substrate have been investigated (Priest et al. in 1994, Hayes et al. in 1992, 1998 and 2001, and Duthaler in 1995). However, these researches have met with mixed success, primarily due to the difficulty of adhering droplets to previously solidified layers. Other problems include oxidation of the liquid metal and the difficulty of fabricating a droplet-expulsion mechanism compatible with the melting temperatures of most high-quality metals beyond low-temperature solders. Other approaches for droplet deposition, called ink-jet printing, as a route to silicon-like device fabrication have included printing metallo–organic decomposition inks (Teng and Vest in 1988), dry powders (Perçin et al. in 1998), organic light-emitting materials (Bharathan and Yang in 1998, and Hebner in 1998), photonics and solders (Priest et al. in 1994), and printing resin binders into successive layers of loose powder (Williams in 1990). However, to date, such processes have been limited in terms of electrical conductivity, feature complexity and thickness, resolution, or material quality, and none have been able to fabricate active MEMS devices.

1.2.2.5 On Nano-Transfer. Loo et al. (2002) have extended the μCP concept to nanoscale dimensions in an additive process referred as nanotransfer printing in which metallic structures was transferred directly onto a substrate surface.

1.3 Conclusion

Each technique discussed in Section 1.2.2 has its own advantage and disadvantage. Although different approaches and solutions have been developed to overcome these shortcomings, there is still one common problem left unsolved in all these techniques – open loop. In another word, all these techniques have no integrated way of evaluating the

quality of dispensed spots on the fly, not to mention the capability of re-spotting on faulty ones. Taking the Affymetrix GeneChip for example, the whole process ends with a comprehensive series of quality control tests consisting of hybridizations and quantitative test. These independent sampling tests take time and extra biological materials only to find out whether the sampled arrays are good or not. Chances are that arrays delivered to customers are bad in quality.

Therefore, it is of importance to implement a system not only can handle liquid material, but also has an integrated way of detecting and further controlling the quality of delivered liquid in real-time manner according to certain specification. The work in this dissertation is to implement such a system based on the SmartPin technology.

CHAPTER 2

EXPERIMENTAL SYSTEM

The experimental system is comprised of a pin assembly, positioning system, a fiber optic sensing system, a control system, and various auxiliary components such as vision system, ultrasonic cleaner, and a GeneTac 4 scanner (Figure 2.1).

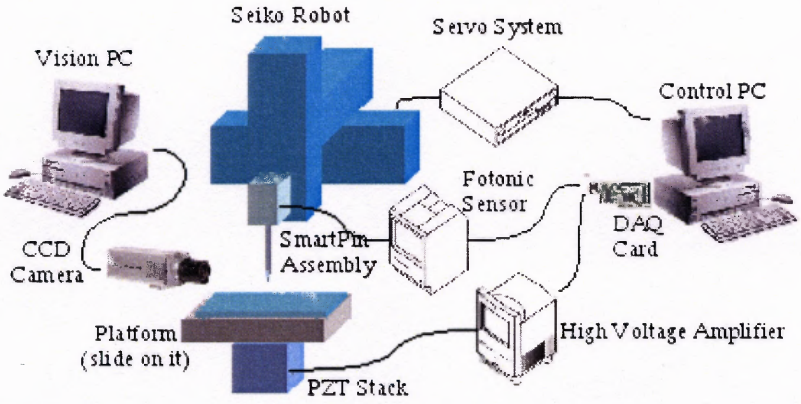

Figure 2.1 Construction diagram of experimental system.

2.1 The Pin Assembly

As the core part of the SmartPin technology, the pin assembly consists of pulled glass pin, fixture, optical fiber, fiber support, and plunger (Figure 2.2).

The borosilicate glass tubes with 600 microns inner diameter and 840 microns outer diameter are readily available commercially. The PUL-1 micropipette puller with NI15 Ni/Cr heating ribbon of 1.5 mm width is used to pull each glass tube into two tapered glass pins (Figure 2.3). The raw pulled pins with blind filaments are then dipped into 25% - 35% de-ionized water (DI) solution of hydrofluoric (HF) for 30 – 45 seconds at room temperature. Before checking the etched pins, thorough cleansing is necessary in which the pin is rinsed by and in the order of: DI water, warm acetone, and DI water

along with drying out by heat gun. The cleansing liquid and the hot air should be directed from the bigger opening of the pin to the smaller side (Figure 2.4). To achieve desired size of pin orifice, several cycles of etching-cleansing-drying operations is needed.

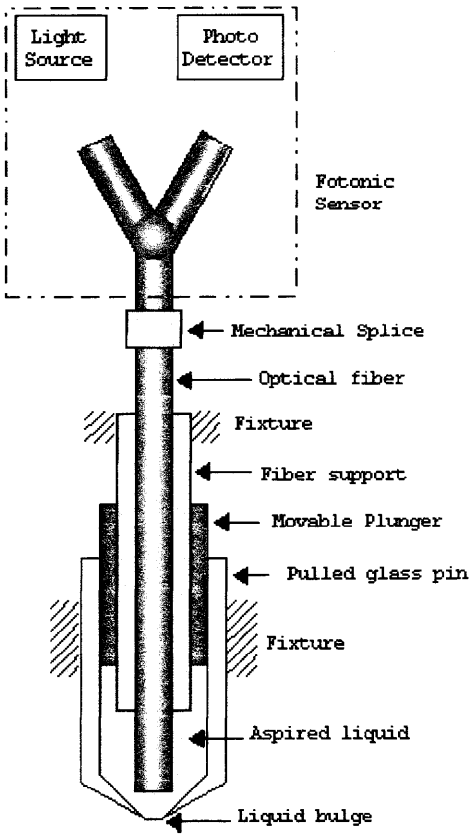

Figure 2.2 Cross section diagram of the liquid delivery system.

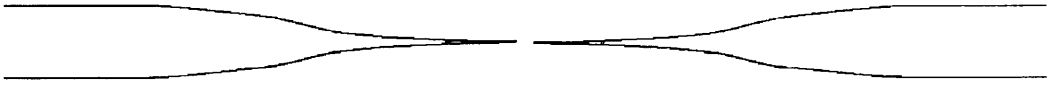

Figure 2.3 Pulled glass pins with blind filaments.

Figure 2.4 Direction of cleansing and drying out operations.

The assembling starts from the most inner part. A single strand of acrylic polymer unjacketed optical fiber of 250 microns diameter is inserted into a tiny cylindrical steel tube which functions as protection and support of the optical fiber. The gap between the fiber and the inner of the tube is stuffed with epoxy to form a sealed rigid object. Another tiny cylindrical steel tube is engineered to fit in between of the fiber support and inner of the glass pin resulting in a plunger. As such, the bottom ends of the optical fiber, fiber support, plunger, and the inner of the cone-shaped pin tip form a sealed reservoir for liquid materials to be dispensed.

The pin assembly is then attached to moving part of the positioning sub-system by specially designed fixture to not only keep its upright stature without any slipping, but also protect it from breaking (Figure 2.5). The cylindrical main part has a concentric cylindrical hole inside to guide the inserted pin. When the main part is fixed vertically, the inserted pin is fixed vertically too. The smaller end of the main part is a threaded stud with cone-shaped hole inside. When the threaded cap is wrenched tight to the stud, the press part will push the two rubber o-rings toward the smaller side of the cone-shaped whole, thus squeeze the o-rings to wrap tightly around the glass pin. The friction between the rubber o-rings and the outside of the glass pin prevents the glass pin from relative axial movement, while the elasticity of the rubber o-ring cushions the clamping force around the glass pin to prevent it from breaking.

A linear actuator (Zaber T-LA28A) is also attached to the same moving part of the positioning sub-system. The movable plunger of the pin assembly is attached to the driving head of this linear actuator. Thus, actuation of Zaber will be turned into the linear

movement of the plunger relative to the glass pin resulting in aspiration and deposition of liquid materials.

Figure 2.5 Fixture for the pin assembly.

Figure 2.6 Linear actuator (Zaber T-LA28A) for plunger.
(Source: Zaber Technologies Inc., 2007)

Zaber T-LA28A is a computer controlled linear actuators with 0.1 um resolution and up to 28 mm travel. It is a standalone unit requiring only a standard 12 V unregulated AC/DC transformer for power. Multiple units can be daisy-chained to the RS-232 port of any computer. Convenient 6-pin mini din cables on the unit allow for direct interconnection between units in close proximity. Table 2.1 lists some of the specifications of this linear actuator.

Table 2.1 Specifications of Zaber T-LA28A Linear Actuator

Range (mm)	Resolution (um)	Repeatability (um)	Accuracy (um)	Backlash (um)	Min speed and resolution (mm/sec)	Max Spped (mm/sec)
28	0.1	< 0.4	< 12	< 4	.0009302	4

(Source: Zaber Technologies Inc., 2007)

2.2 The Positioning System

The positioning sub-system consists of a Seiko D-TRAN XY-3000 robot and a PZT-stack, the former of which is for positioning along X-, Y-, and Z-axis, while the latter is for fine positioning along Z-axis.

2.2.1 Seiko D-TRAN XY-3000 Robot

The Seiko D-TRAN XY-3000 robot package include a four axis, closed-loop DC servo robot in Cartesian configuration, a dual Z-80 based controller, a Teach-Terminal, and a powerful robot language named DARL which is similar to BASIC in syntax. Each of the four axes provides a different motion and contributes to the degree of freedom of the robot. The alpha axis or A-axis provides rotation to the end-effector, the Z-axis provides the vertical stroke, the X-axis provides a back and forth stroke, and the Y-axis provides the lateral stroke (Figure 2.7). Motion is point-to-point and the axes can move simultaneously. Table 2.2 lists the specifications of all the axes used in experiments.

The controller is compact, modular and contains the software that allows powerful communications through an RS-232C port to vision systems, peripheral equipment or host computers. It can also allow the operator to interface with it directly via the Teach-terminal or remote areas (such as a systems control panel).

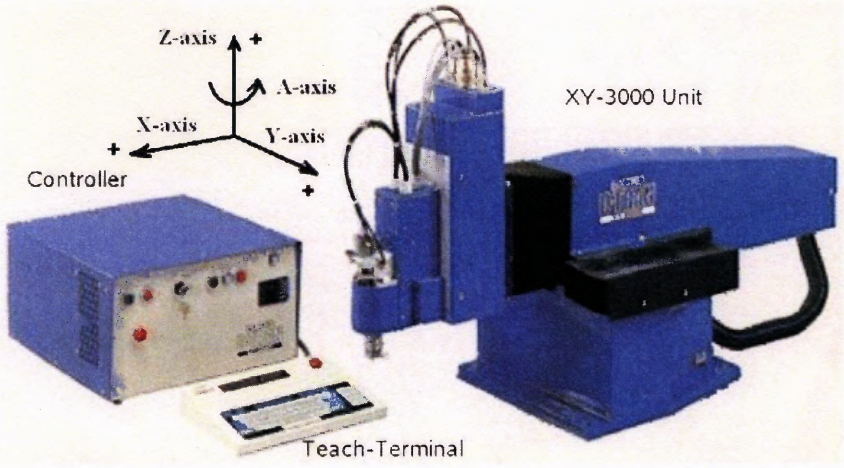

Figure 2.7 Parts and configuration of Seiko D-TRAN XY-3000 robot package.
(Source: Seiko Corp., 1990)

Table 2.2 Specifications of Seiko D-TRAN XY-3000 Robot

	Stroke (mm)	Resolution (mm)	Repeatability (mm)	Max Speed (mm/sec)	Dimensions (deep x wide x high) (mm)
X-axis	300	0.010	± 0.008	1000	140 x 210 x 872
Y-axis	200	0.010	± 0.008	1000	333 x 554 x 470
Z-axis	100	0.010	± 0.008	500	100 x 150 x 441

(Source: Seiko Corp., 1990)

2.2.2 The Micro-Stage with Lead Zirconate Titanate (PZT) Stack

Since the resolution and accuracy are relative big (0.010 mm and 0.030 mm respectively) compared to dimension requirement of microarray, a compensating positioning device with more fine displacements is required. A PZT-stack (P-844.40) is employed due to its high precision, bandwidth and linearity.

Figure 2.8 shows the PZT-stack used in experiments. It is a low voltage piezoelectric stack with monolithic ceramic construction of many thin piezoceramic layers which are connected in parallel electrically. The principal characteristics of the stack are: high energy conversion efficiency, low voltage operation, large force, low motion, fast response, and no electromagnetic interference (EMI). Motion may be

increased, at the expense of force, by mechanical amplification. The stack offers a high energy density in a small package. Due to its superior compressive strength, it provides a high load bearing capability. However, it is relatively weak in tension. Generally, excitation should be applied only in the direction of polarization. Hysteresis is typically about 15% in static applications. Table 2.3 and 2.4 list the specifications and performance of P-844.40 PZT-stack.

To actuate the PZT-stack, a HP 6827A high voltage amplifier is employed which can amplify the input of -10V~+10V into -100V~+100V within maximum frequency response of 30 kHz.

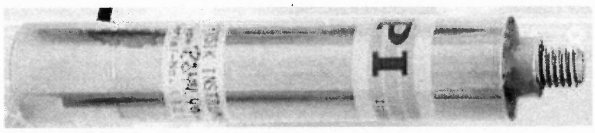

Figure 2.8 PZT-stack used for fine positioning.
(Source: Physik Instrumente GmbH & Co. KG, 2008)

Table 2.3 Specifications of P-844.40 PZT-stack

Travel Range (open-loop) (μm)	Rated DC Voltage (V)	Length (mm)	Base Diameter (mm)	Tip Diameter (mm)	Weight (g)	Push/Pull Force Capacity (N)	Max. Torque at Tip (N·m)
60	100	101	19.8	12	156	3000/700	1

(Source: Physik Instrumente GmbH & Co. KG, 2008)

Table 2.4 Performance of P-844.40 PZT-stack

Resolution (open-loop) (nm)	Static Large-Signal Stiffness (N/ μm)	Electrical Capacitance (μF)	Dynamic Operating Current Coefficient (μA/Hz×μm)	Resonant Frequency (unloaded) (kHz)
0.6	57	24	50	7.5

(Source: Physik Instrumente GmbH & Co. KG, 2008)

2.3 The Fiber Optic Sensing System

The fiber optic sensing system consists of MTI-2100 Fotonic Sensor, MTI-2020R probe module (Figure 2.9), mechanical splicer, and the spliced optical fiber extension.

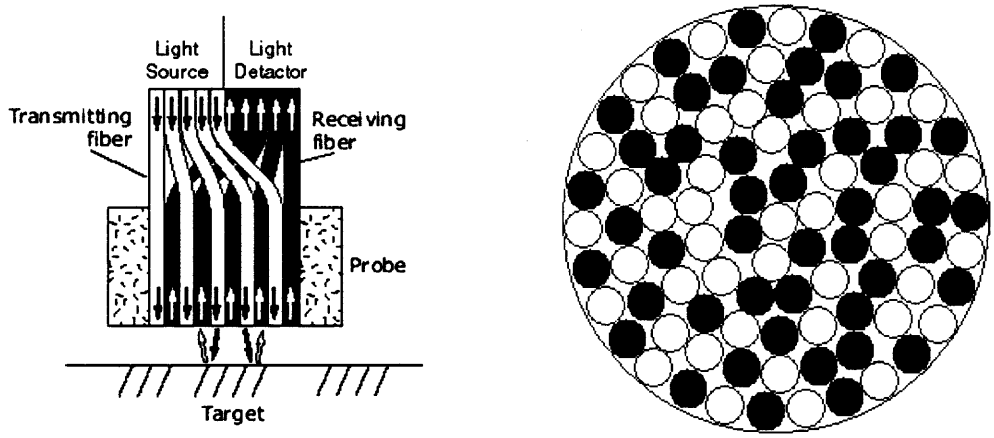

Figure 2.9 Side view (left) and cross section (right) of the MTI-2020R probe.
(Source: MTI Instruments Inc., 2007)

The MTI-2100 Fotonic Sensor is dual-channel, fiber-optic measurement system that performs noncontact displacement and vibration measurements on reflective surfaces. By using fiber-optic technology, the MTI-2100 imposes no load on the measurement target and is not affected by magnetic and electrical fields. It is able to measure displacement motion ranging from 0.25 nm to 5.08 mm at frequencies ranging from DC to over 150 kHz. The collimated light beam generated by a controlled light source is carried by the transmitting fibers toward the probe tip and the target while the reflected light is carried back to a photo-detector through the receiving fibers. The displacement information is inferred ratiometrically from the intensity of the reflected light by a digital signal processor. The distribution of the transmitting and receiving fibers at the probe tip is in random manner. The total and active diameters of the probe

tip are 0.508 mm and 0.305 mm respective. Table 2.5 lists specifications of MTI-2020R probe module.

Table 2.5 Specifications of MTI-2020R Probe Module

Max Freqency Response (-3dB) kHz	Output Singal Noise (mV p-p)	Meter Resolution (μm)		Range 1 Characteristics		
		Range 1	Range 2	Sensitivity $\left(\frac{\mu m}{mV}\right)$	Linear Range (mm)	Standoff (mm)
120	30	0.01	0.1	0.016	0.102	0.127

Range 2 Characteristics			Optical Peak (mm)	
Sensitivity $\left(\frac{\mu m}{mV}\right)$	Linear Range (mm)	Standoff (mm)	Mid-Point	Range
0.076	0.305	0.508	0.305	0.127

(Source: MTI Instruments Inc., 2007)

To prevent the probe tip from possible damage, a strand of plastic optical fiber is mechanically spliced at the tip of the probe to extend the probe into the pin assembly. The core of the fiber is made of acrylic polymer PMMA (poly-methl-methacrylate) and is sheathed with a special thin layer of fluorine polymer which has a lower refractive index than the fiber core. Table 2.6 list specifications of this fiber.

Table 2.6 Specifications of Unjacketed Optical Grade Fiber Strand

Core Diameter (μm)	Outer Diameter (μm)	Max Attenuation (dB/m) @650 nm	Core Refractive Index (n_1)	Clad Refractive Index (n_2)	Numerical Aperture (NA) $(n_1^2-n_2^2)^{1/2}$	Acceptance Angle (2sin[NA])
240	250	0.30	1.492	1.402	0.51±0.03	61°

(Source: Edmund Optics Inc., 2007)

Figure 2.10 illustrates the construction of fiber splicing and coupling. The MTI-2020R probe, the plastic fiber, and the ball lens are fixed collinearly along the center line

of the mechanical splicer. To decrease the signal loss, the sealed chamber inside the splicer is filled with LS-1246-10 index-matching optical gel which has refractive index of 1.46. Due to the diameter difference between the probe and the fiber, a Φ0.5 mm ball lens, which is made of AL_2O_3 sapphire with refractive index of 1.77, is used to couple light into the fiber. The NA of the ball lens must be less than or equal to the NA of the fiber to ensure that all the light will be coupled. The gap between the probe tip and the ball lens is about 0.1 mm and the gap between the fiber tip and the ball lens is the back focal length (BFL) which can be calculated by Equation (0.1) and (0.2) from geometrical optics of ball lens.

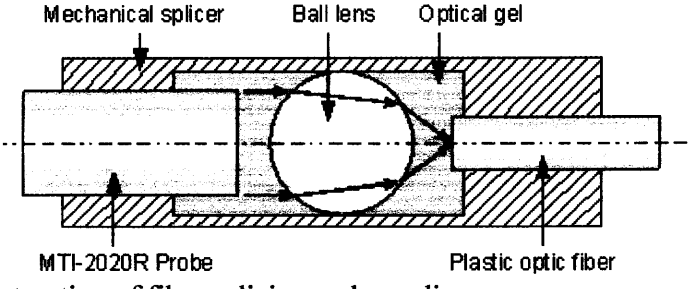

Figure 2.10 Construction of fiber splicing and coupling.

$$\mathrm{EFL} = \frac{Dn_1}{4(n_1 - n_2)} = \frac{0.5 \times 1.77}{4 \times (1.77 - 1.46)} = 0.71\,\mathrm{mm} \tag{0.1}$$

$$\mathrm{BFL} = \mathrm{EFL} - \frac{D}{2} = 0.71 - 0.25 = 0.46\,\mathrm{mm} \tag{0.2}$$

$$\mathrm{NA} = \frac{2d(n_1 - n_2)}{Dn_1} = \frac{2 \times 0.305 \times (1.77 - 1.46)}{0.5 \times 1.77} = 0.21 \tag{0.3}$$

where the D is the diameter of the ball lens, d is the diameter of the incident light beam, n_1, n_2 are refractive indices of the ball lens and the surrounding optical gel respectively, EFL stands for effective focal length, BFL stands for back focal length, NA stands for numerical aperture. Figure 2.11 explains these concepts.

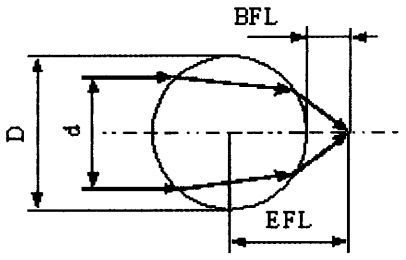

Figure 2.11 Geometrical optics of ball lens.

2.4 The Control System

The control system is based on a PC which is built upon a 3.4GHz Pentium 4 Hyper-Threading technology enabled processor and 1GB double-data-rate two synchronous dynamic random access memory (DDR2 SDRAM). The interfaces to the Seiko robot and Zaber actuator are two independent RS-232 serial communication ports. The interface to the Fotonic sensor and the high-voltage amplifier is a NI PCI-6024E DAQ card. The control software will be discussed in Chapter 3.

2.5 The Auxiliary Components

Besides the aforementioned sub systems, there are several auxiliary components used for results verifications, system maintenance, or demos.

2.5.1 The Vision System

Since the pin is too tiny, it is helpful to have a vision system to show what is happening during the liquid dispense on the run for purpose of demo. The captured and saved images or videos are helpful for out-of-lab presentations.

The vision system consists of a SONY XCD-SX910CR ½" type progressive scan IT transfer CCD camera, a 4X DIN achromatic microscope objective lens, C-mount lens

adapter, a halogen lamp, an IEEE1394A card, and a video capture software named Coriander running on Linux. Table 2.7 lists the specifications of the CCD camera.

Table 2.7 Specifications of SONY XCD-SX910CR CCD Camera

Number of effective pixels	Unit cell size (μm)	Max transfer speed (Mbps)	Protocol	Image format	Frame rate (fps)
1392 (H) x 1040 (V)	4.65	400	IIDC (ver. 1.3)	1280x960 Mono8/16 1024x768 Mono8/16 800x600 Mono8/16 640x480 Mono8/16	Up to 15

(Source: Sony Corp., 2003)

It is of value to measure geometrical parameters by counting number of graphic pixels in the captured images. The sensor size of a ½" type CCD camera is 6.4 x 4.8 mm. The field of view (FOV) will be decreased to 1.6 x 1.2 mm by use of the 4X microscope objective lens. The resolution of each graphic pixel is obtained by dividing the decreased FOV by effective pixels 1392 x 1040.

$$\text{Horizontal Resolution}=\frac{1600}{1392}\doteq 1.15\ \mu\text{m/pixel} \tag{0.4}$$

$$\text{Vertical Resolution}=\frac{1200}{1040}\doteq 1.15\ \mu\text{m/pixel} \tag{0.5}$$

2.5.2 The Ultrasonic Cleaner

To avoid cross contamination, it is required to have pin cleaned in between of two consecutive spotting of different liquid materials. Bransonic 220 ultrasonic cleaner is used. Ultrasonic cleaning is a fast, safe way of cleaning for many small, difficult to clean items. It has been used by laboratories, dentists, jewelers, and industry for years.

The ultrasonic cleaner uses high frequency sound waves to create literally millions of tiny, microscopic bubbles in the solution. These bubbles expand and then rapidly collapse. As they collapse, they release a significant amount of energy creating an intense "scrubbing" action which is effective on visible surfaces as well as small crevices and even blind holes. Dirt can be loosened and removed from any surface that the liquid touches. This action, called "cavitation", occurs thousands of times every second to quickly produce clean parts.

2.5.3 The Microarray Scanner

For purpose of establishing relationships between experiment data and morphology of dispensed spots, GeneTAC UC-4 microarray scanner with GeneTAC Integrator Version 3.3 is introduced during the data analysis stage of research.

The GeneTAC UC-4 microarray scanner offers high resolution (up to 5 microns) scanning across the surface of standard microarray substrates. It is the first two-color system to offer a Universal Slide Carrier (USC). Each USC holds four slides allowing to scan multiple microarrays at one time. The two-color system includes green and lasers coupled with high performance optics that maximize the collection of fluorescent signals while minimizing the damage caused by photobleaching. The scanner includes a workstation with powerful software named Integrator that automates the identification and quantification of microarray data.

2.5.4 The Clean Chamber

Since the pin is sensitive on the ambient air, a clean local environment with constant temperature and humidity is necessary to obtain high quality spotting.

The skeleton of the clean chamber is built by structural aluminum material covered with transparent plastic sheets. One side of the sheet can be roll up to allow manual operation of the devices inside the chamber. A two in one air purifier and humidifier is placed inside the chamber to create the required dust-free, constant temperature and humidity local environment. The core experimental system is shown in Figure 2.12. Not shown in the figure are the GeneTac 4 scanner and the Fotonic sensor console.

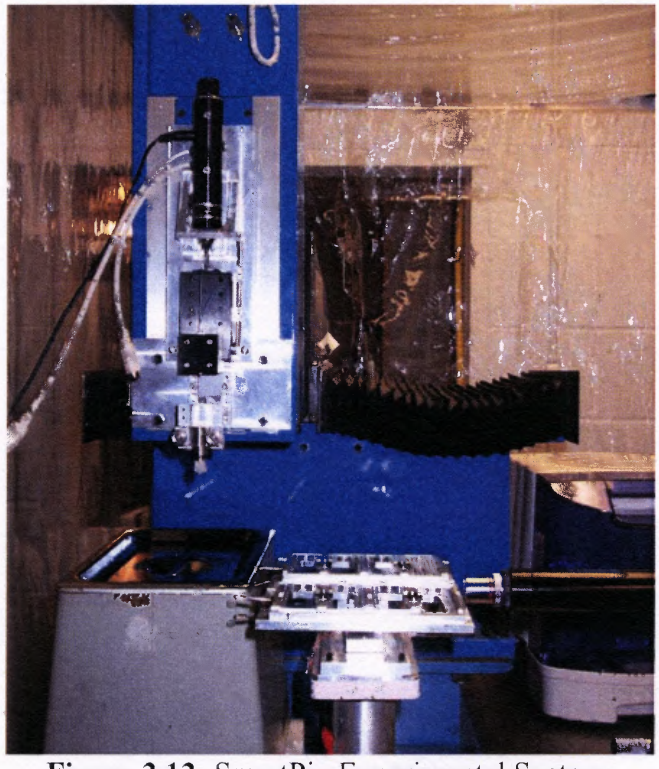

Figure 2.12: SmartPin Experimental System.

CHAPTER 3

SOFTWARE DEVELOPMENT

3.1 Interfacing Control PC with External Devices

There are three external devices that are subjected to the commands of the control PC – the Seiko robot, the Zaber linear actuator, and the high-voltage amplifier. There is also the Fotonic sensor from which the signal data is to be acquired through the DAQ card for decision-making of control loop.

3.1.1 RS-232C

The hardware interfaces between Seiko robot and control PC, and Zaber and control PC are RS-232C serial communication ports and the corresponding cables. Since the control PC has only one RS-232C serial communication port, it is necessary to either install extension card with extra RS-232C serial communication ports or USB-to-RS-232C converter. The latter option is used in this work.

The electrical specifications of the serial port are defined in the Electronics Industry Association (EIA) RS-232C standard. The connector for RS-232C serial port on PC is usually male D-type 9 pin connector which was defined by EIA-574. Figure 3.1 illustrates the layout of such pin out, and Table 3.1 lists the definitions of the pin out.

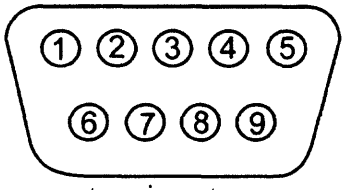

Figure 3.1 Layout of D-type 9 connector pin out.

Table 3.1 Definition of D-type 9 Connector Pin Out

Pin No.	Abbreviation	Full Name	Function
1	TD	Transmit Data	Serial Data Output (TXD)
2	RD	Receive Data	Serial Data Input (RXD)
3	RTS	Request To Send	This line informs the Modem that the UART is ready to exchange data.
4	CTS	Clear To Send	This line indicates that the Modem is ready to exchange data.
5	DSR	Data Set Ready	This tells the UART that the modem is ready to establish a link.
6	SG	Signal Ground	
7	CD	Carrier Detect	
8	DTR	Data Terminal Ready	This is the opposite to DSR. This tells the Modem that the UART is ready to link.
9	RI	Ring Indicator	Goes active when modem detects a ringing signal from the PSTN.

RS-232C was originally developed for communications between data communications equipment (DCE) such as modem and data terminal equipment (DTE) such as PC. However, there are many cases in which the communications take place between two DTEs (in this work, they are Seiko robot terminal, Zaber, and PC). The Null Modem connection is commonly used for such cases. Table 3.2 shows the Null Modem connection.

Table 3.2 Null Modem connection.

DTE 1 Pin Out			DTE 2 Pin Out	
3	TD	———	RD	2
2	RD	———	TD	3
5	SG	———	SG	5
4	DTR	⌐¬	DTR	4
6	DSR	⌐¬	DSR	6
1	CD	⌐¬	CD	1
7	RTS	⌐¬	RTS	7
8	CTS	⌐¬	CTS	8

RS-232 communication is asynchronous, i.e., a clock signal is not sent with the data. Each word is synchronized using its start bit, and an internal clock on each side, keeps tabs on the timing.

Figure 3.2 shows the expected waveform from the RS-232 port when using the common 8N1 format. 8N1 signifies 8 data bits, no parity and 1 stop bit. RS-232C logic levels uses +3 to +25 volts to signify a "Space" (logic 0) and -3 to -25 volts for a "Mark" (logic 1). Any voltage in between these regions (i.e. between +3 and -3 Volts) is undefined. The RS-232C line is in the mark state (logic 1) when idle. A transmission starts with a start bit (logic 0). Then each bit is sent down the line, one at a time. The least significant bit (LSB) is sent first. A stop bit (logic 1) is then appended to the signal to make up the transmission.

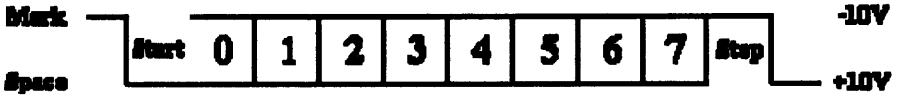

Figure 3.2 RS-232C Logic waveform.

The diagram also shows the next bit after the stop bit to be logic 0. This must mean another word is following, and this is its start bit. If there is no more data coming then the receive line will stay in its idle state (logic 1). There is also a "break" signal which happens when the data line is held in a logic 0 state for a time long enough to send an entire word. Therefore if the line is not put back into an idle state, then the receiving end will interpret this as a break signal.

The data sent using this method is said to be framed. That is the data is framed between a start and stop bit. If a log 0 is received at the stop bit spot, a framing error will

occur. This error is not uncommon when both sides are communicating at different speeds.

3.1.2 NI PCI-6024E Card

The NI PCI-6024E card is PnP (Plug and Play) compatible multifunction analog, digital, and timing I/O card for the PCI (Peripheral Component Interconnect) bus computers. It features 12-bit ADCs with 16 analog inputs, 12-bit DACs with 2 analog voltage outputs, eight TTL-compatible digital I/O, and two 24-bit counter/timers for timing I/O. It can be easily configured and calibrated by user program. This feature is made possible by the National Instruments MXI Interfaces To Everything) (MITE)bus interface chip to connect the card to the PCI I/O bus. The MITE implements the PCI local bus specification so that the DMA, interrupts, and base address are all software configurable.

As shown in Figure 3.3, the PCI-6024E card consists of the following major components:

- PCI bus interface circuitry with Plug and Play capability (MITE)
- Analog input circuitry
- Analog trigger circuitry
- Analog output circuitry
- Digital I/O circuitry
- Timing I/O circuitry (DAQ-STC)
- RTSI bus interfa

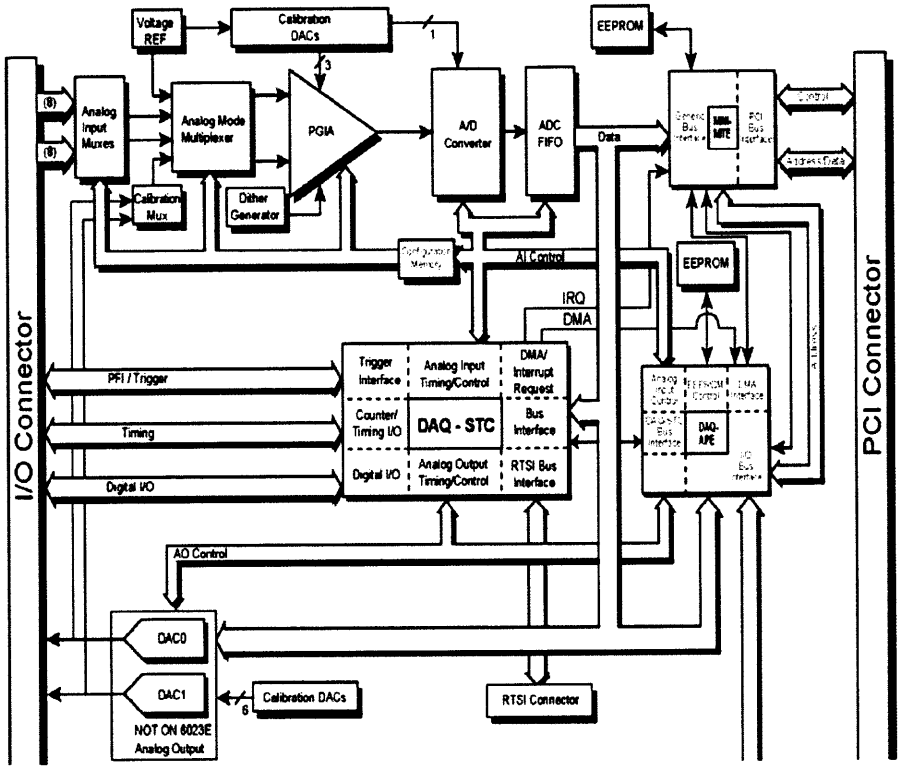

Figure 3.3 Block diagram of PCI-6024E.
(Source: National Instruments Corp., 1998)

The internal data and control buses interconnect the components. The DAQ-STC (Data Acquisition System Timing Controller), an ASIC (Application-Specific Integrated Circuit), is the timing engine that provides precise timing signals for the analog input and output operations. The DAQ-STC consists of three timing groups that control analog input, analog output, and general-purpose counter/timer functions. These groups include a total of seven 24-bit and three 16-bit counters and a maximum timing resolution of 50 ns.

The interface circuitry consists of a PCI interface chip and a digital control logic chip. As shown in Figure 3.4, the PCI interface chip provides a mechanism for the PCI E Series to communicate with the PCI bus. The digital control logic chip connects the PCI interface chip with the rest of the card. It is fully compliant with PCI local bus

specification, revision 2.0. Therefore, the base memory address and the interrupt level for the card are stored inside the PCI interface chip at power on. The PCI bus is capable of 8-bit, 16-bit, or 32-bit transfers, but PCI 6024E card uses only 6-bit transfers.

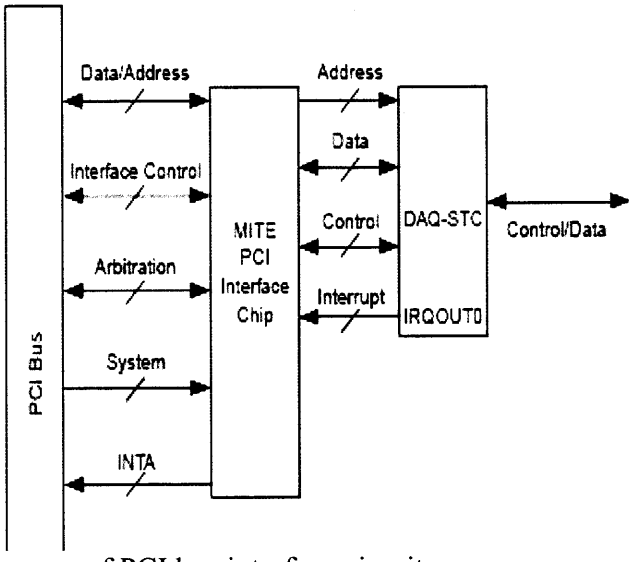

Figure 3.4 Block diagram of PCI bus interface circuitry.
(Source: National Instruments Corp., 1998)

The bus-mastering capability of the MITE provides high-speed data transfer between the card and system memory. The MITE contains three DMA channels that can be used simultaneously for data transfer with analog input, analog output, and the general-purpose counters. The MITE can control the PCI bus and transfer the data without interrupting the host processor.

The DAQ-STC can generate interrupts from over 20 sources and can route these interrupts to the INTA line on the PCI bus interface. Since DAQ-STC IRQOUT0 line is connected to the MITE interrupt input, all interrupts are routed through IRQOUT0.

The PCI-6024E card has 16 analog input channels and a dedicated timing core within the DAQ-STC. Figure 3.5 shows a general block diagram for the analog input circuitry. It includes input multiplexer, multiplexer mode selection switches, a software-

programmable gain instrumentation amplifier, calibration hardware, a sampling ADC, a 16-bit wide data FIFO, and a configuration memory.

The configuration memory defines the parameters to use for each conversion. Each entry in the configuration memory includes channel type, channel number, bank, gain, polarity, dither, general trigger, and last channel. The configuration memory is a 512-entry deep FIFO that is initialized prior to the start of the acquisition sequence. It can be incremented after every conversion, allowing the analog input configuration to vary on a per conversion basis. Once the FIFO is empty, the DAQ-STC asserts the FIFO retransmit signal, which restores the FIFO data to its original state.

The channel type field indicates the resource type to be used during the conversion and controls the multiplexer mode selection switches. These resources include calibration channels, analog input channels in differential, referenced single-ended, or non-referenced single-ended mode, or a ghost channel. The ghost channel type indicates that a conversion should occur but that the data should not be stored in the data FIFO. This type is useful for multi-rate scanning.

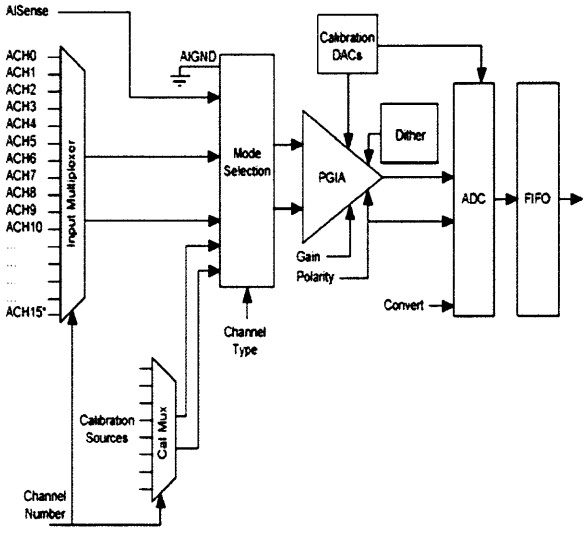

Figure 3.5 Block diagram of analog input and data acquisition circuitry.
(Source: National Instruments Corp., 1998)

The channel number indicates which channel of the specified type will be used during the conversion, while the bank field indicates which bank of 16 channels is active. These bits control the input multiplexers.

The PGIA (Programmable Gain Instrumentation Amplifier) serves two purposes on the PCI-6024E card The PGIA applies gain to the input signal, amplifying an analog input signal before sampling and conversion to increase measurement resolution and accuracy. This gain is determined by the gain field in the configuration memory. It also provides polarity selection for the input signal, which is also controlled by the configuration memory. In unipolar mode, the input range includes only positive voltages. In bipolar mode, the input signal may also be a negative voltage. The PGIA provides gains of 0.5, 1, 10, and 100.

The dither circuitry adds approximately 0.5 LSB RMS (Root Mean Square) of white Gaussian noise to the signal being converted by the ADC. This addition is useful for applications, such as calibration, involving averaging to increase the resolution of the card to more than the resolution of the ADC. Dither should be disabled for high-speed applications not involving averaging because it would only add noise.

The last channel bit is used to indicate that this is the last conversion in a scan. The DAQ-STC will end the scan on the conversion with this bit set.

The PCI-6024E card uses sampling, successive approximation ADCs with 12 bits of resolution with maximum conversion rate of 5 μs. The converter can resolve its input range into 4,096 different steps for the 12-bit ADC. The input range of the 12-bit cards is ±5 V in bipolar mode and 0 to +10 V in unipolar mode. These modes correspond to ranges of –2,048 to 2,047 in unipolar mode and 0 to 4,095 in bipolar mode.

The PCI-6024E card include a 16-bit wide FIFO to buffer the analog input data. This buffering will increase the maximum rate that the analog input can sustain during continuous acquisition. The FIFO is 512 words deep. The DAQ-STC shifts the data into the FIFO from the ADC when the conversion is complete. This buffering allows the ADC to begin a new conversion even though the data has not yet been read from the card. This buffering also provides more time for the software or DMA to respond and read the analog input data from the card. If the FIFO is full and another conversion completes, an error condition called FIFO overflow occurs and the data from that conversion is lost. The FIFO not empty, half-full, and full flags are available to generate interrupts or DMA requests for the data transfer.

Measurement reliability is assured through the onboard calibration circuitry of the card. This circuitry uses an internal, stable 5 V reference that is measured at the factory against a higher accuracy reference; its value is then stored in the EEPROM (Electrically Erasable Programmable Read-Only Memory). With this stored reference value, the card can be recalibrated at any time under any number of different environmental conditions in order to remove errors caused by time and temperature drift. The EEPROM stores calibration constants that can be read and then written to calibration DACs that adjust input offset, output offset, and gain errors associated with the analog input section. When the card leaves the factory, the upper one-fourth of the EEPROM is protected and cannot be overwritten. The lower three-fourths is unprotected, and the top fourth of that can be used to store alternate calibration constants for the different conditions under the card is used.

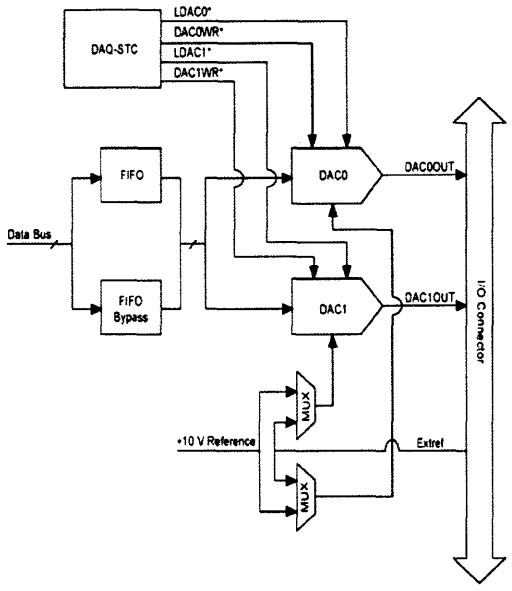

Figure 3.6 Block diagram of analog output circuitry.
(Source: National Instruments Corp., 1998)

The PCI-6024E card has two analog output channels and a dedicated timing core within the DAQ-STC. Figure 3.6 shows block diagram for the analog output circuitry.

The analog output on the card includes two channels of double-buffered analog output with programmable polarity, reference source, and re-glitch circuit, as well as a FIFO to buffer the data.

Each analog output channel contains a 12-bit DAC, an amplification stage, and an onboard voltage reference. The output voltage will be proportional to the voltage reference (Vref) multiplied by the digital code loaded into the DAC. The polarity, reference source, and re-glitch circuit are all configured in the AO configuration register. The onboard reference is fixed at +10 V. For unipolar output, the voltage is simply attenuated. Four-quadrant multiplication occurs in bipolar output, where the signal will not only be attenuated but also inverted for negative digital codes.

The DAC output can be configured to produce either a unipolar or bipolar output range. A unipolar output has an output range of 0 to +Vref –1 LSB V. A bipolar output has an output voltage range of –Vref to Vref –1 LSB V). For unipolar output, the data written to the DAC is interpreted in straight binary format. For bipolar output, the data is interpreted as two's complement format. One LSB is the voltage increment corresponding to an LSB change in the digital code word. For a 12-bit DAC, 1 LSB = (Vref)/4,096 in unipolar mode, and 1 LSB = (Vref)/2,048 in bipolar mode.

Using the 12-bit DAC and onboard 10 V reference will produce an output voltage range of 0 to 9.9976 V in steps of 2.44 mV for unipolar output and an output voltage range of –10 to +9.9951 V in steps of 4.88 mV for bipolar operation.

PCI-6024E has a zero-depth virtual FIFO for analog output. This buffering will increase the maximum rate that the analog output can sustain for waveform generation. It can also be used to store a complete waveform which can be output repetitively without any further data transfer to the FIFO.

3.1.3 Software Drivers

Software drivers are pieces of program in form of modules that encapsulate the details of hardware and offer high-level, more understandable interfaces to applications. Take serial communication for example, the applications send commands such as "move", "stop" to external devices, and read replies from them through software driver without considering the details such as "what does the command consist of", or "how is the command transmitted".

The settings of RS-232 for Seiko Robot is 9600 bps baud rate, 8-bit data bit, 1-bit stop bit, no parity, and full duplex. The message package consists of ASCII string ending with CR, and LF. One example of command to have the Robot move is

"DO SPEED 10:T1=20.5 10.2 -40.3 0.0:MOVE T1\r\n"

The response from the Robot may contain several lines each of which ends with "\r\n". So the test for the end of response is a different character ">".

The settings of RS-232 for Zaber is 9600 bps baud rate, 8-bit data bit, 1-bit stop bit, no parity, and full duplex. The message package consists of binary codes with constant length of 6. The format for message package is

UNIT_ID(1 byte), COMMAND_ID(1 byte), CONTENT(4 bytes)

To drive the PZT stack, the driving voltage should be refined to a smooth slope consisting of sequence of tiny steps. The linear model of the PZT stack is used to interpret the displacement command into required driving voltage.

3.2 Quasi-realtime on PC

Although PC plus Windows platform is not a candidate for real-time control, we can still utilize low-level functionalities offered by this platform to prototype a quasi-realtime system for proof of concept.

3.2.1 Multi-Threading on Windows XP

A thread is basically a path of execution through a program. It is also the smallest unit of execution that Win32 schedules. A thread consists of a stack, the state of the CPU registers, and an entry in the execution list of the system scheduler. Each thread shares all of the process's resources.

A process consists of one or more threads and the code, data, and other resources of a program in memory. Typical program resources are open files, semaphores, and dynamically allocated memory. A program executes when the system scheduler gives one of its threads execution control. The scheduler determines which threads should run and when they should run. Threads of lower priority may have to wait while higher priority threads complete their tasks. On multiprocessor machines, the scheduler can move individual threads to different processors to "balance" the CPU load.

Each thread in a process operates independently. The threads execute individually and are unaware of the other threads in a process. Threads sharing common resources, however, must coordinate their work by using semaphores or another method of IPC (Inter-Process Communication). Each thread has its own stack and its own copy of the CPU registers. Other resources, such as files, static data, and heap memory, are shared by all threads in the process. Threads using these common resources must be synchronized. Win32 provides several ways to synchronize resources, including semaphores, critical sections, events, and mutexes.

When multiple threads are accessing shared data, the program must provide solutions for possible resource conflicts. Take the sampling program for an example, the DAQ thread updates a static data structure containing the x, y coordinates of the Seiko

robot for items to be displayed by the main graphical user interface (GUI) thread. If the DAQ thread alters the x coordinate and is preempted before it can change the y coordinate, the GUI thread may be scheduled before the y coordinate is updated. The item would be displayed at the wrong location. This problem can be avoided by using semaphores to control access to the structure.

A mutex (short for mutual exclusion) is a way of communicating among threads or processes that are executing asynchronously of one another. This communication is usually used to coordinate the activities of multiple threads or processes, typically by controlling access to a shared resource by "locking" and "unlocking" the resource. To solve this x, y coordinate update problem, the DAQ thread would set a mutex indicating that the data structure is in use before performing the update. It would clear the mutex after both coordinates had been processed. The GUI thread must wait for the mutex to be clear before updating the display. This process of waiting for a mutex is often called "blocking" on a mutex because the process is blocked and cannot continue

Screen displays and shared data are only two of the resources requiring careful management. For another example, the program has multiple threads accessing the same file data file which is to be used by future analysis. Because another thread may have moved the file pointer, each thread must reset the file pointer before reading or writing. In addition, each thread must make sure that it is not preempted between the time it positions the pointer and the time it accesses the file. These threads should use a semaphore to coordinate access to the file by bracketing each file access with WaitForSingleObject() and ReleaseMutex() calls.

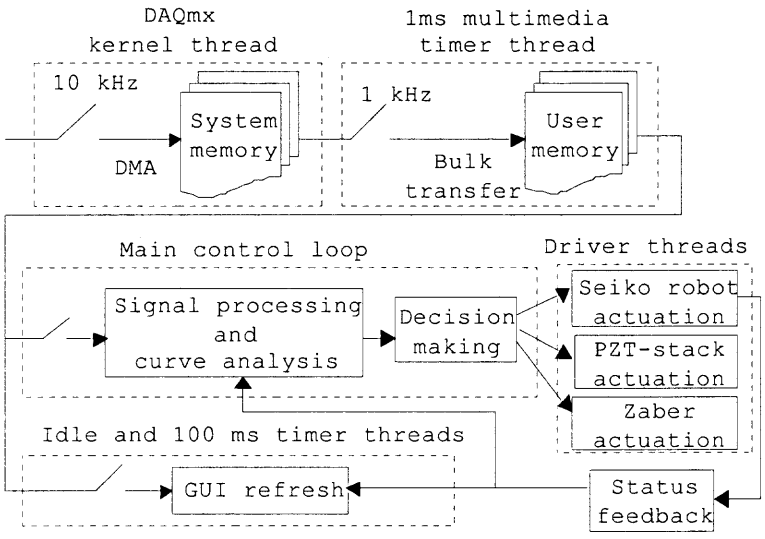

Figure 3.7 Multi-threading scheme of the control software.

The multiple threads in the control software are: GUI, main control loop, data acquisition, and actuations of PZT stack, Zaber and Seiko Robot. All these threads are executed strictly in order yet fast through multi-threading and double-buffering technique as shown in Figure 3.7.

To keep strict synchronization through different devices, the cycle time of the main control loop varies from 0.1 to 100 milliseconds depending on which device is driven after each decision making. To keep the user being informed of current status, a GUI updating thread is invoked at either idle periods or 100 milliseconds interval.

The main control loop retrieves and analyzes all available data since end of last loop from the user memory.

3.2.2 Quasi-Realtime with High Performance Timer

The DAQmx kernel thread works in system space and uses DMA mode to transfer data so that it can achieve up to 200 kHz sampling rate. However, the threads working in user space are not able to access to the sampled data with such high frequency. To avoid data loss and system memory overflowing, another user data buffer is employed. A thread invoked by 1 ms high-performance multimedia timer is in charge of transfer all available sampled data from system memory to user memory.

3.2.3 Direct Memory Access (DMA)

Besides the multithreading and high performance timer techniques, the DMA is used to do bulk data transfer between the DAQ card and the memory directly without interrupting CPU.

DMA (also referred to as bus mastering) is a technique that some components and devices use to transfer data directly to and from memory without passing through the Central Processing Unit (CPU). DMA reduces CPU overhead by providing a mechanism for data transfers that do not require monitoring by the CPU. The number associated with DMA indicates the direct memory access channel that the component or device uses to transfer data to and from memory.

The PCI-6024E DAQ card can be configured as DMA mode as shown in Figure 3.8. Figure 3.9 is a screenshot of the running program.

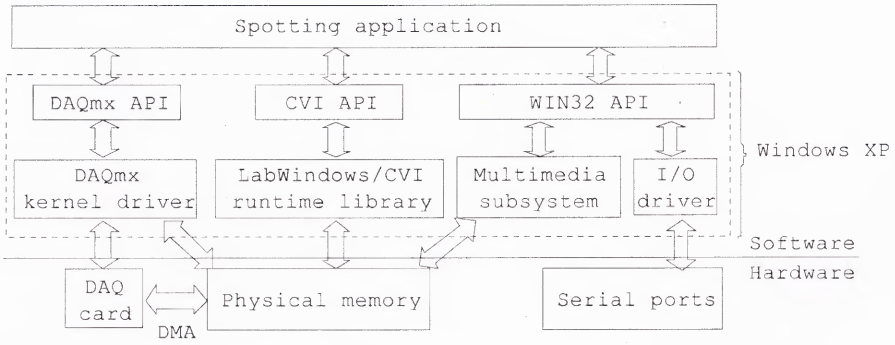

Figure 3.8 Software configuration.

3.3 Integrated Control of the Spotting Process

Primary application of the SmartPin is microarray fabrication which consists of liquid aspiration, preparation, spotting in certain matrix-patterned locations, and cleaning. The self-sensing property of the SmartPin makes it feasible to automate all these steps.

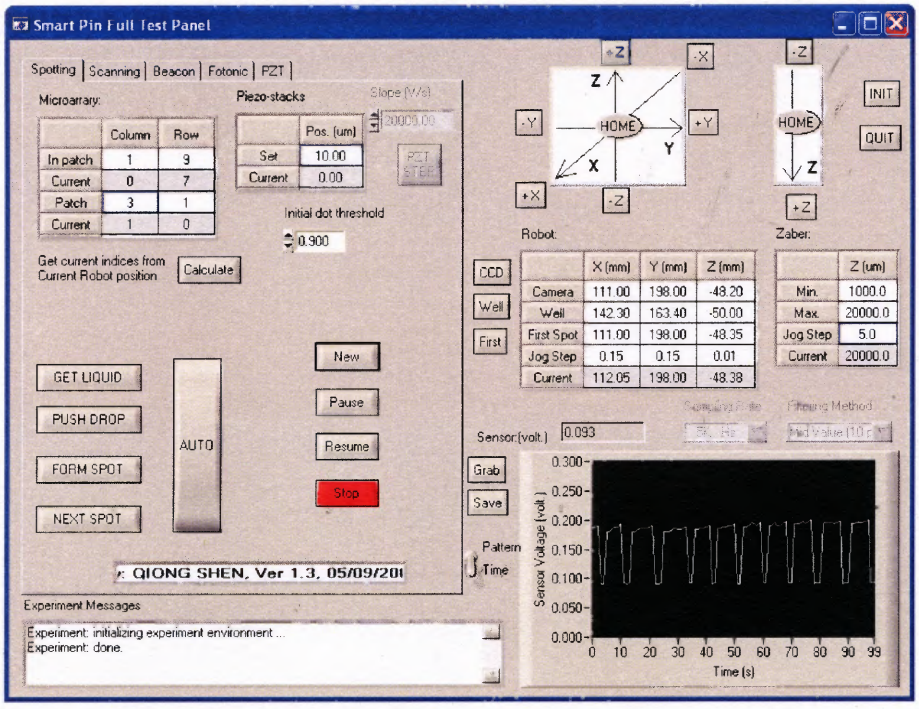

Figure 3.9 Screenshot of the control software.

When the pin is about to aspire liquid, due to the absence of the liquid inside pin tip, the light ray can travel through the orifice thus sensing any reflective surface near the pin tip. That means the pin can scan over the micro-well plate where the liquid samples are, and locate the specified liquid sample. After dipping into the liquid, the pulling of the plunger can aspire the liquid into the pin cavity during which the increasing liquid top surface causes increasing sensor signal. The sensor signal will drop down when the liquid top surface surpass the optical fiber tip, i.e. when the reflective surface is gone (as shown in Figure 3.11) For a pin with 60 micron orifice, at least 22 nanoliters of liquid can be aspired. Since the aspiration will leave some liquid residue on the exterior sidewall of the pin tip which usually results in bigger spot size, an initial spotting 10-20 dots on a preparation area is usually carried out. The spotting starts as soon as the pin assembly is moved to the spotting area. The plunger is pushed with a small displacement to form a liquid bulge at the bottom of glass pin tip. For a typical glass pin with 60 micron opening, the plunger has to move 0.1 micron to form a liquid bulge with 10 micron height. Each spotting is a sequence of pin approaching to and departing from the slide surface. At the end of spotting for each type of liquid material, the pin assembly is

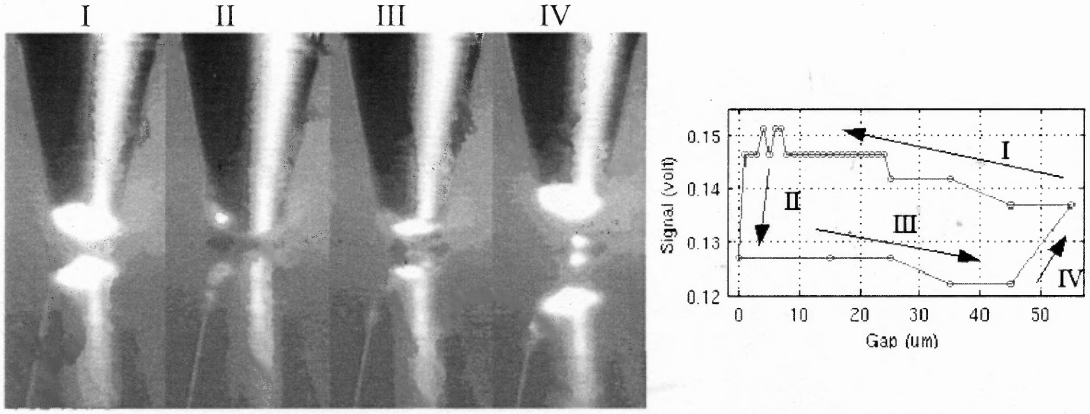

Figure 3.10 Photos (left) and sensor curve (right) of liquid dispensing process.

moved to a ultrasonic cleaner, several turns of push-and-pull movements of the plunger is performed to clean both the inner and outer areas of the glass pin. During this step, the signal similar to the aspiration step repeats with each push-and-pull cycle.

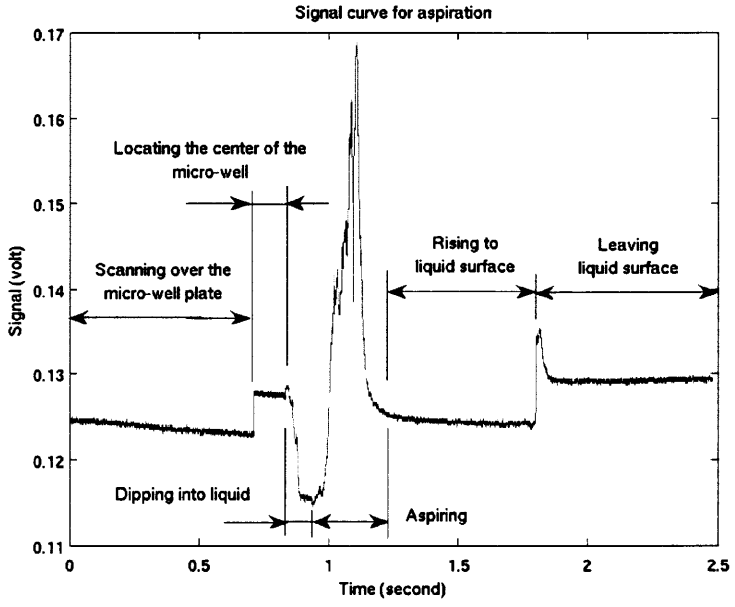

Figure 3.11 Signal curve for aspiration.

Based on the curve in Figure 3.10 (right), different actuations will be made. During the early stage of Phase I, the Seiko robot is driven to move down as fast as possible while the PZT stack is kept stationary. When 10% or more increase of signal level is detected, actuation of PZT stack is introduced. Each movement of the Seiko robot is followed by a sequence of fine movements of the PZT stack with a step size of 1 micron and maximum range of 15 microns. If no spot is formed during the final movement of the PZT stack, the PZT stack will be driven back to its initial length. This is followed by another cycle of 10 micron step movement of the Seiko robot and 1 micron movement of the PZT stack. As soon as 10% or more signal drop is detected, i.e., the spot is formed, Phase III begins. The Seiko robot and the PZT stack are driven back

simultaneously in a step-by-step manner which results in elongation of the liquid column. A signal intensity increase exceeding a predefined threshold (average value of intensities over the spotting cycle) indicates the pinch-off of the liquid column. For a successful spotting cycle, Phase IV ends at the initial position of Phase I thereby completing the process.

3.4 Integrated Control of Micro-Line Drawing Process

The spotting mechanism can be extended to draw micro-line based pattern by two approaches: spot-sequence approach and liquid-column sweeping approach.

3.4.1 Spot-Sequence Approach

On possible way to draw a line is to generate a sequence of spots with small enough position offset along the line direction.

In this way, drawing a line is actually making a condensed microarray with an overlapping path planning function. This approach is similar to the inkjet method and has the same disadvantages of low drawing inefficiency and non-uniform object morphology especially when the object to be draw has sharp corners and features.

Due to the resolution of the Seiko robot on the directions of the line to be drawn (X- and Y- axis), the minimum achievable center-to-center distance between two consecutive spots is 10 um. For a pin with orifice of 60 um diameter to draw a 2 mm line in this way, about 200 spots need to be made. To avoid the negative effect of precedent liquid spot on next spot, there should be a certain amount of time between two consecutive spotting actions for the precedent liquid spot to dry out (typically 10 seconds

for spot made by 3XSSC buffer and of 65 um diameter). Therefore, the time to draw a good quality 2 mm long line is about 34 minutes. However, the time for each liquid spot to dry out is not a constant, which means there may be time waste for some spots, and the other spots may cause damages to the uniformity and continuity of the whole line.

3.4.2 Liquid-Column Sweeping Approach

Based on observations, during the early stage of the elongation phase of the liquid column when the internal force among layers of the liquid column is strong enough to generate a strong shear stress to overcome the shear stress between the liquid and the substrate surface, the tangential (or horizontal) movement of the pin will bring the liquid column into sweeping (or sliding) motion along the substrate surface thus leave a trace of footprint on the substrate surface depending on path of the pin. The concept is shown in Figure 3.12.

To draw a uniform straight line, the key is to keep the footprint constant throughout the whole drawing. Factors to disturb the process are non-flat surface, non-parallel between the motion of the pin and the substrate surface, non-uniform shear stress between liquid column and the substrate surface, and disturbance in speed of the motion of the pin (the DC servo system of the Seiko robot takes care of this issue). Any of these factors will cause change of shape of the liquid column and consequent change of signals from the Fotonic sensor. Adjusting the position of the substrate through driving the PZT stack will compensate these disturbances. Therefore, the control of the footprint of the liquid column is changed into the control of the PZT stack to keep the signal from the Fotonic sensor constant.

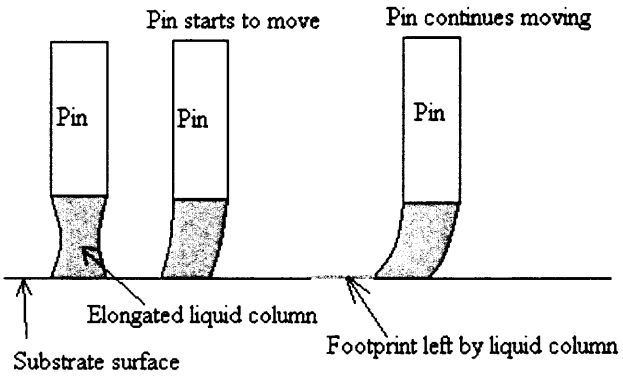

Figure 3.12 Illustration of liquid-column sweeping method.

Figure 3.13 shows the block diagram of the PI control system. To avoid pinching off of the liquid column, the Seiko robot is commanded to move the pin horizontally at constant speed of 1 mm/s. The P and I constants used are 0.1. The time for drawing a 2 mm straight line is about 2 seconds.

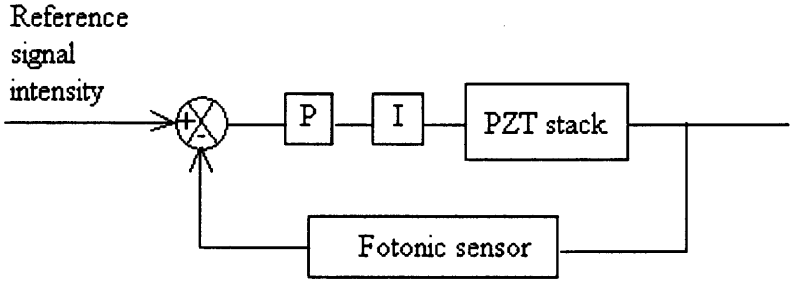

Figure 3.13 Block diagram of control system for liquid-column sweeping method.

CHAPTER 4

EXPERIMENTS AND RESULT ANALYSIS

A series of experiments have been carried out to find out the relationship between SmartPin signal intensity and morphology of spots and to explore the potential capability of the spotting system in patterning of large area organic electronics.

4.1 120K Spots Deposition

A slide with 120,000 spots is sufficient to analyze the entire set of protein coding genes which at present are estimated to be about 20000. The materials used in this test are 0.3%, 0.6%, 1.2% and 2% Cy3 random 9-mer oligonucleotides in 3X SSC solution. The substrate is one standard 1x3 inches microscope slide with poly-L-lysine (PLL) coating. Ambient temperature and humidity are 25 degrees Celsius and 70. The orifice of the pin tip is 60 microns. The slide is scanned by GeneTAC UC-4 scanner with 595BP green laser of 30 intensity and 5-micron resolution. Material consumption on each spot is about 40 pico-liter. The 120K spots are composed of 60 patches of spots, each patch is in the form of 10x200 matrix, and each patch is made by one material. Four materials are used alternatively in the ascending order of Cy3 concentrations and cyclically every four patches until the last patch (the 60th patch). During each switch of materials, a thorough cleaning of the pin by ultrasonic cleaning system is performed to eliminate cross contamination (the extent of the cleaning is evaluated by the statistics on the intensities of spots from the scanned image). Figure 4.1, 4.2 show the layout and magnified scan image

of a portion of nominal spots from the 120k spots. Table 4.1 shows statistics on some critical parameters of the 120k spots.

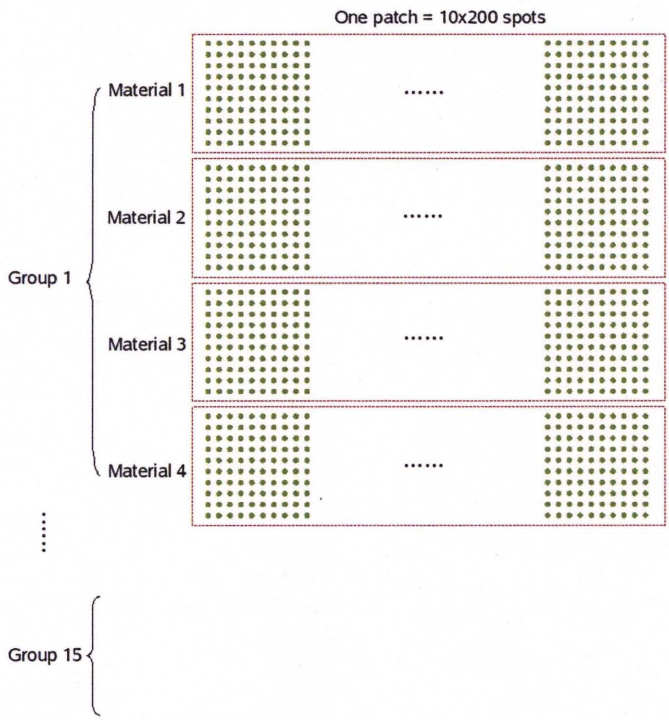

Figure 4.1 Layout of 120K spots.

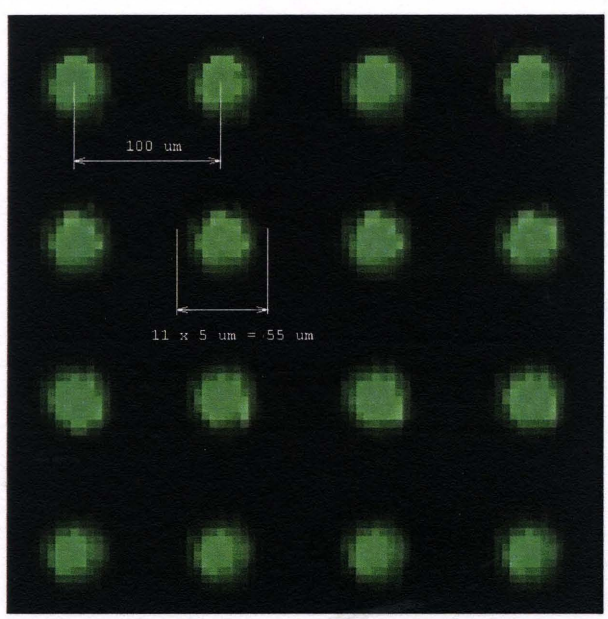

Figure 4.2 Magnified scan image of a portion of nominal spots.

It is of interest to generate a diagnostic template to correlate the spot quality and sensor signal. The "normal spot" data are averaged to generate the diagnostic template curve as shown in Figure 4.3. The error bars indicate that, statistically, the normal spot do fall within a well defined range of variations.

Table 4.1 Statistics of Scan Results of 120K Spots

		0.3 % Cy3	0.6% Cy3	1.2% Cy3	2.0 % Cy3
Number of spots		30,000	30,000	30,000	30,000
[1]Area	Min	105	101	112	111
	Max	120	118	125	119
	Mean	113	109	116	115
	Std Dev	3.5	3.1	4.4	4.1
[2]Target Total Intensity	Min	815001	1520911	3020524	4508537
	Max	987973	2002221	3822943	5965021
	Mean	910472	1816455	3512354	5345838
	Std Dev	36486	40655	80242	85375
[3]Target Std Dev	Min	7461	10058	12257	14571
	Max	7830	10534	13011	15213
	Mean	7633	10293	12563	14801
	Std Dev	174	211	267	310

[1] is the number of Cy3 pixels inside the assigned circle (Φ65 um). Radius of spot equals $\sqrt{\frac{25\text{Area}}{\pi}}$ micron.

[2] is the sum of all the Cy3 pixel intensities inside the assigned circle.

[3] is the standard deviation of the Cy3 pixel intensities inside the assigned circle.

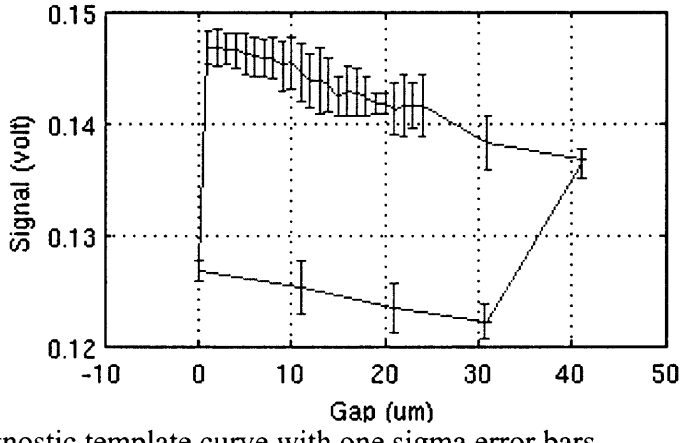

Figure 4.3 Diagnostic template curve with one sigma error bars.

Based on the statistics from the scanner software, three types of abnormal spots are presently detected. Such abnormal spots should be avoided during DNA/protein microarray fabrication. A spot is considered as abnormally big if its area is bigger than double the median spot area. A spot is misshaped when its scanned center location deviates from the pre-defined center location more than 1/8 of the spot diameter. Finally, the criterions for extremely dim or missing spot is met if the spot total intensity is lower than 1/10 of median total intensity. These abnormal spots are discussed below.

Right after the aspiration of liquid, there is residue on the side wall of the tip of pin, resulting in bigger spots at the beginning of the process. Such spots can be easily avoided by spotting on a preparation area until all the residue is consumed out. As shown in Figure 4.4, the initial bigger spot has higher Phase I signal level, bigger high peak signal value, lower Phase III intensity and shorter phase III when compared to the diagnostic template curve.

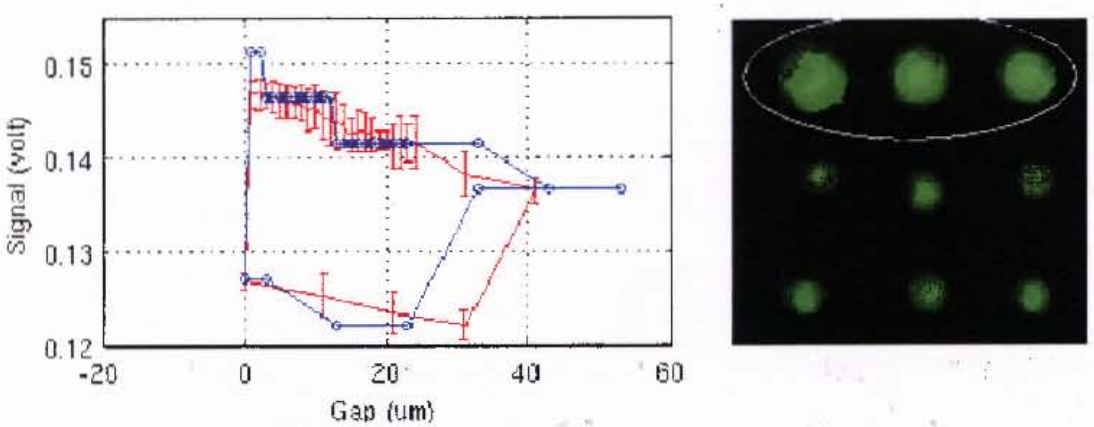

Figure 4.4 Initial bigger spots compared with nominal spots.

Due to the mobility of liquid material, mechanical disturbance during the phase III makes the distribution of Cy3 uneven in the dispensed spot. The prominent feature in the curve of such spots (shown in Figure 4.5) is the incompleteness of the curve at the

end of phase IV. This incompleteness corresponds to the incorrect shape (i.e. not a good circle) of the spot.

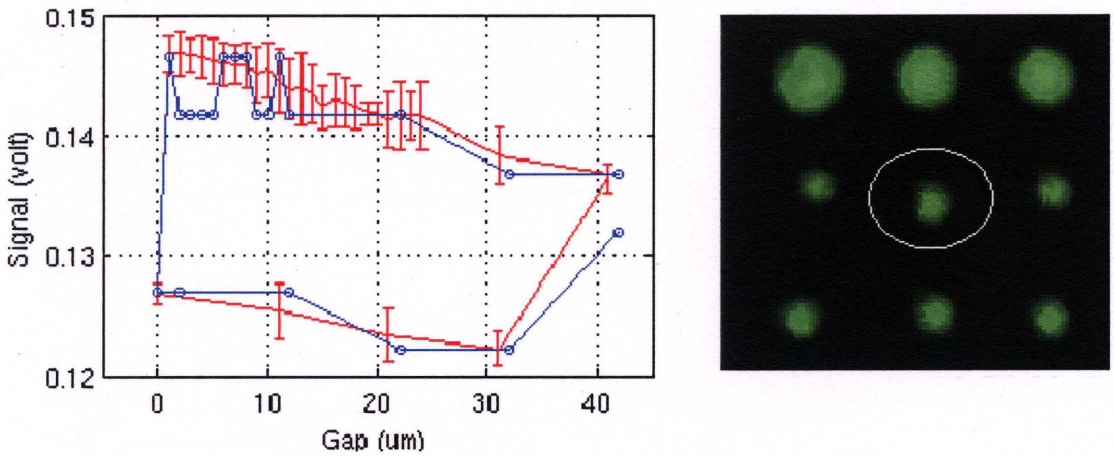

Figure 4.5 Misshaped spots compared with nominal spots.

Strictly speaking, the spots may exist yet they are too dim to be of further use. Such spot results from failure to form a good liquid bulge with enough volume at the pin tip. During the spotting under this circumstance, the glass pin tip gets very close to the surface of slide which attributes to the bigger high peak signal intensity, higher Phase II signal intensities and delayed Phase IV as shown in Figure 4.6.

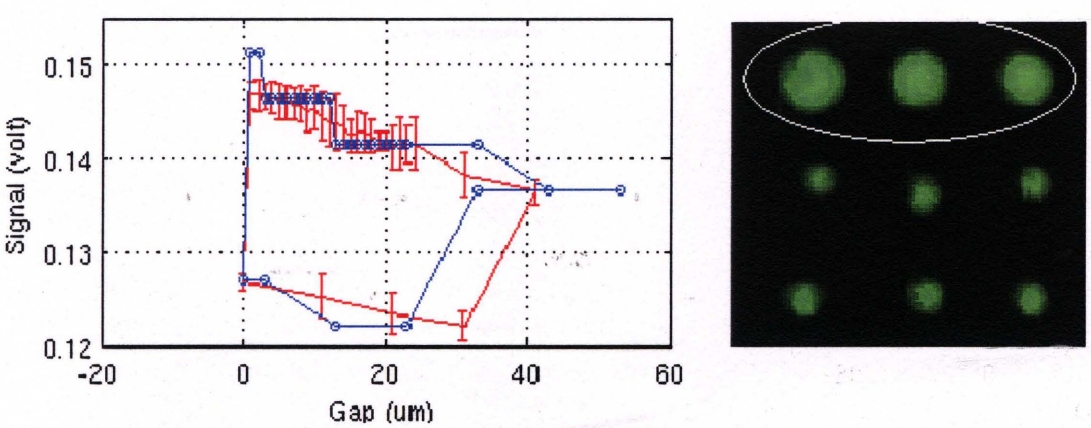

Figure 4.6 Extremely dim/ Missing spots compared with nominal spots.

4.2 DNA Microarray of 14 Oligonucleotides

To evaluate the performance of SmartPin in real-world microarray fabrication, side-by-side comparison of the hybridization data generated from expression arrays printed by the SmartPin and the OmniGrid 100 with SMP3 pins has been conducted.

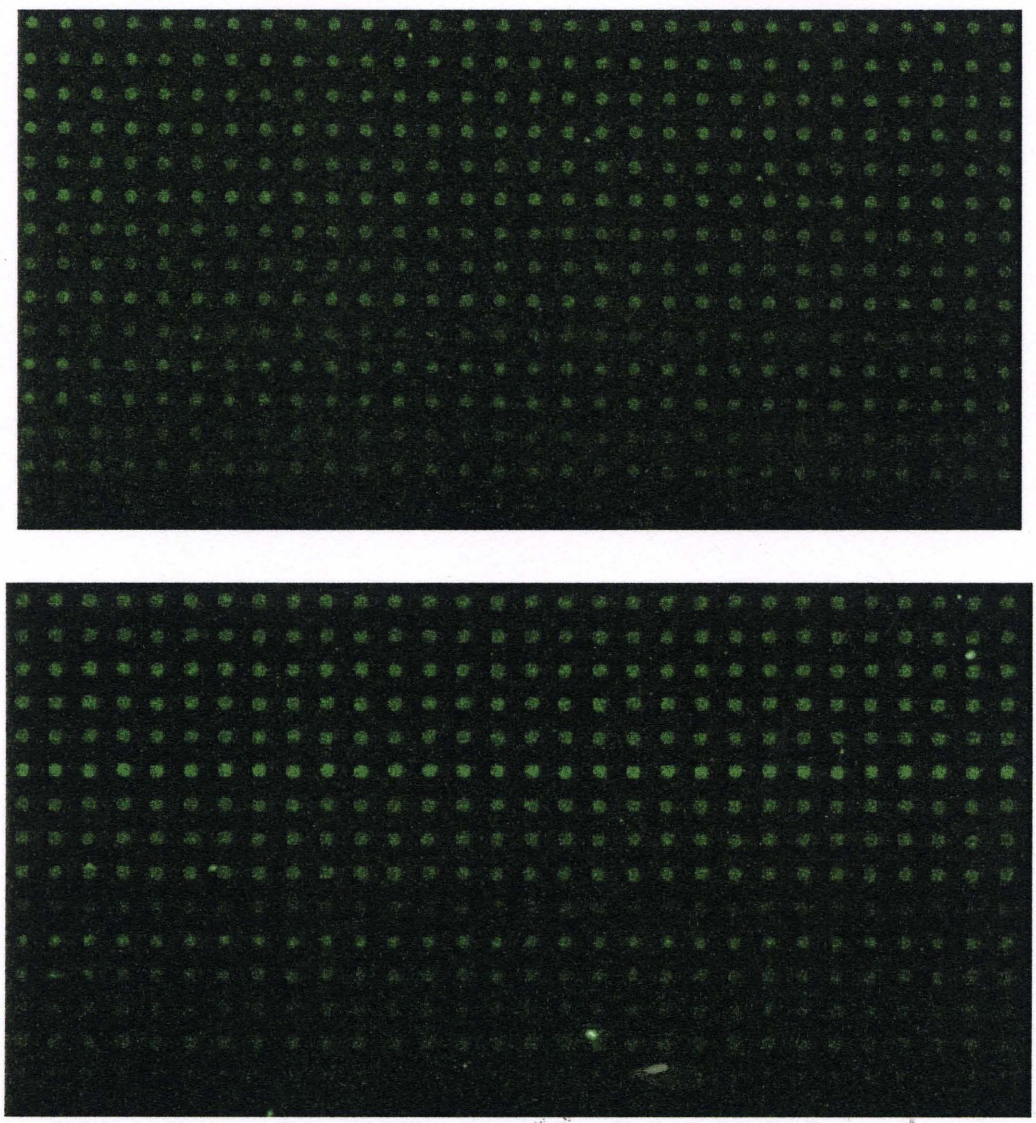

Figure 4.7 Scan images of the 6th slide (array at top is made by the SmartPin, the bottom one is made by the OmniGrid).

In order to obtain statistically robust data, spotting and hybridization were performed on a set of six slides with the SmartPin and the OmniGrid 100 in same day.

The orifice of the pin tip of the SmartPin is 80 microns. The slides are standard 1x3 inches glass microscope slides coated with PLL. The materials were 14 DNA oligonucleotides (30 uM in concentration, five representing human DNA sequences, and nine complimentary DNA to control mRNAs). Each material was spotted 30 times in a row by the SmartPin and the OminiGrid 100 respectively in different areas of each of the slide. The final layout of spots on each slide consists of two patches with each patch in the form of 14x30 matrix. The upper patch was made by the SmartPin and the lower patch by the OmniGrid 100 (as in Figure 4.7).

Spotted slides were post processed following standard protocol: the slides were stored in a dessicator with 30% relative humidity overnight, steam-rehydrated for about 5 seconds, snap-dry for another 5 seconds on a hot plate and then UV-crosslinked using 60 milli Joules of energy. Slides were then washed in a 500 ml solution consisting of 478 ml 1-methyl-2-pyrollidinone, 8 g of succinic anhydride and 22 ml of 1M boric acid (PH 8.0) for 15 minutes with gentle shaking. After vigorous washing in deionized water, the slides were spun dried at 500g for 3 minutes and ready for hybridization. Total RNA labeling and microarray hybridization were performed using Genisphere Array 350 kit.

Briefly, human kidney and liver RNA were combined with control mRNAS and labeled with Cy3 and Cy5, respectively. Six reactions were performed for each of the two RNA samples. First strand cDNA was synthesized from a combination of 2.5 ug of total RNA sample and 1ul control mRNA. The RNA in the DNA/RNA hybrid was denatured, the cDNAs of the two samples to be compared were then combined and purified and concentrated using Millipore Microcon YM-30 centrifugal filter device. The six reactions were then pooled, split again into six and hybridized to the arrays. First, the concentrated

cDNAs in hybridization solution were applied to the microarray and incubated overnight at 42 °C. Post cDNA hybridization washes were performed and 3DNA capture reagents loaded onto the array and incubated for 3 hours at 50 °C. After post 3DNA hybridization washes, the microarray was spun dried at 1000 rpm for 2 minutes. The microarrays were scanned with a GenePix 4000B scanner. Feature intensities were extracted from scanned images using GenePix Pro 5.1.

The following parameters were compared: Spot diameter, F635 CV, F532 CV, Ratio of Medians, 635 channel Signal-to-Noise ratio (SNR), 532 channel SNR, 635 Median Intensity CV, 532 Median Intensity CV. All these parameters were calculated by the GenePix Pro 5.1 software except for 635 Median Intensity CV and 532 Median Intensity CV. The 635 Median Intensity CV and 532 Median Intensity CV were calculated using the standard deviation of 635 or 532 Median Intensity divided by the average of 635 or 532 Median Intensity, where 635 or 532 Median Intensity were extracted using the GenePix Pro 5.1 software. All of the above parameters were computed from either 30 data points (intra- slide) or 180 data points (inter- slide).

Spot diameter combined with F635 or F532 CV is a measurement of spot homogeneity and uniformity in microarray technology. SmartPin generated array resulted in smaller spot diameter, smaller F635 CV and F532 CV, suggesting that SmartPin can make more uniform and homogeneous spots (Figures 4.8 and 4.9).

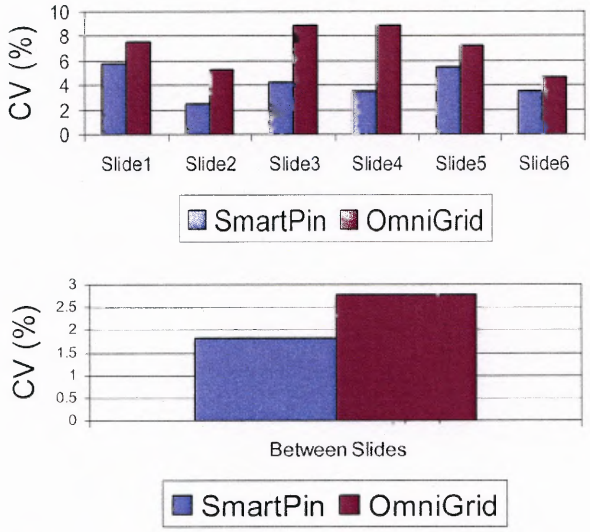

Figure 4.8 CVs of spots diameters on each slide (top) and between slides (bottom).

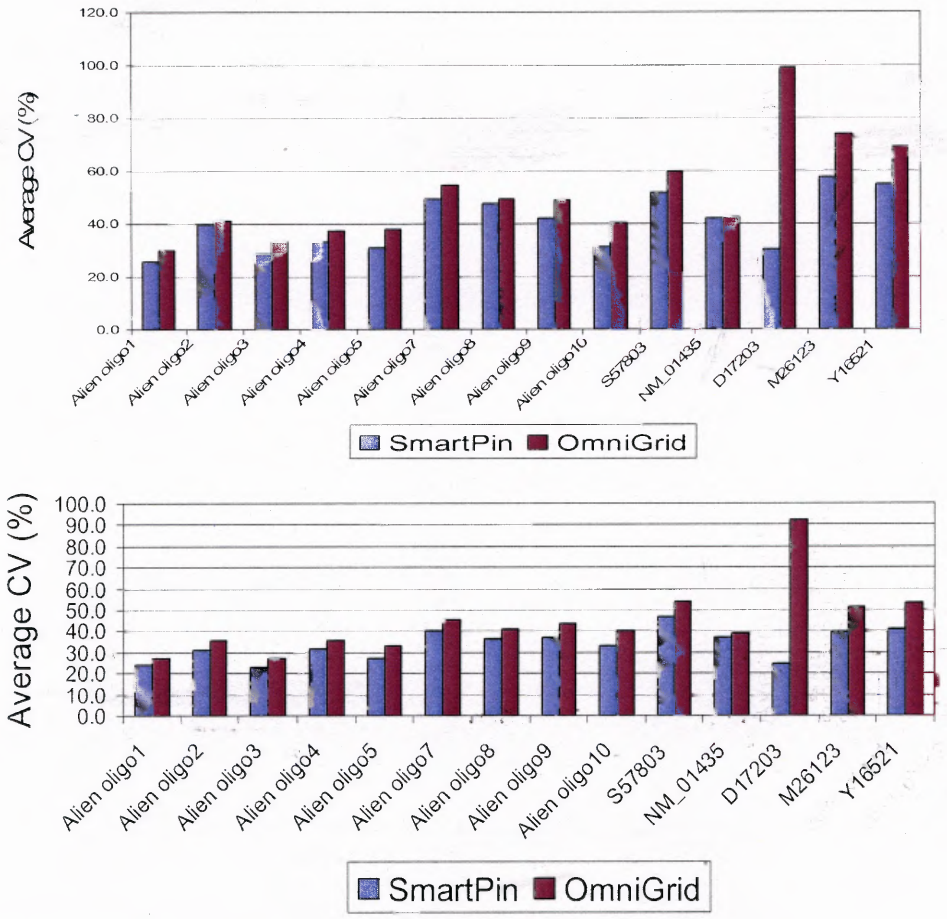

Figure 4.9 Average F635 (top) and F532 (bottom) CVs of 6 slides.

Ratio of Medians can be used to indicate the reliability of microarray data. The Ratio of Medians from both approaches show only a slight difference, suggesting the SmartPin can generate as reliable data as conventional printing methods (Figure 4.10).

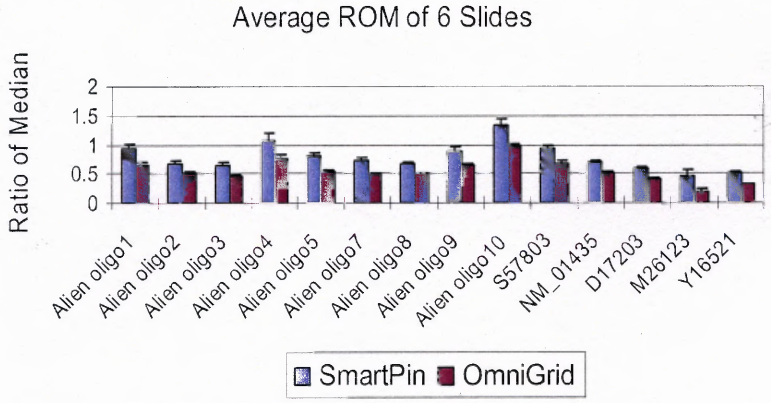

Figure 4.10 Average ROMs of 6 slides.

The signal-to-noise ratio (SNR) is defined by (Mean Foreground - Mean Background) / (Standard deviation of Background). The SmartPin seems to perform better on SNR of F635 channel among all the oligos tested (Figure 4.11 top), and for about half of those tested oligos, the SmartPin also generated higher SNR on F532 channel (Figure 4.11 bottom).

The CV of the Median Intensity was used to measure the data reproducibility in our comparison. A smaller Median Intensity CV means smaller variation among replicate spots thus better reproducibility. For some oligos, the SmartPin produced array produced spots with a smaller Median Intensity CV. However, for some other oligos, we found that OmniGrid100-made arrays had smaller Median Intensity CV (Figure 4.12). Further development of automation on SmartPin in the future will eliminate some variation in the data and improve data reproducibility.

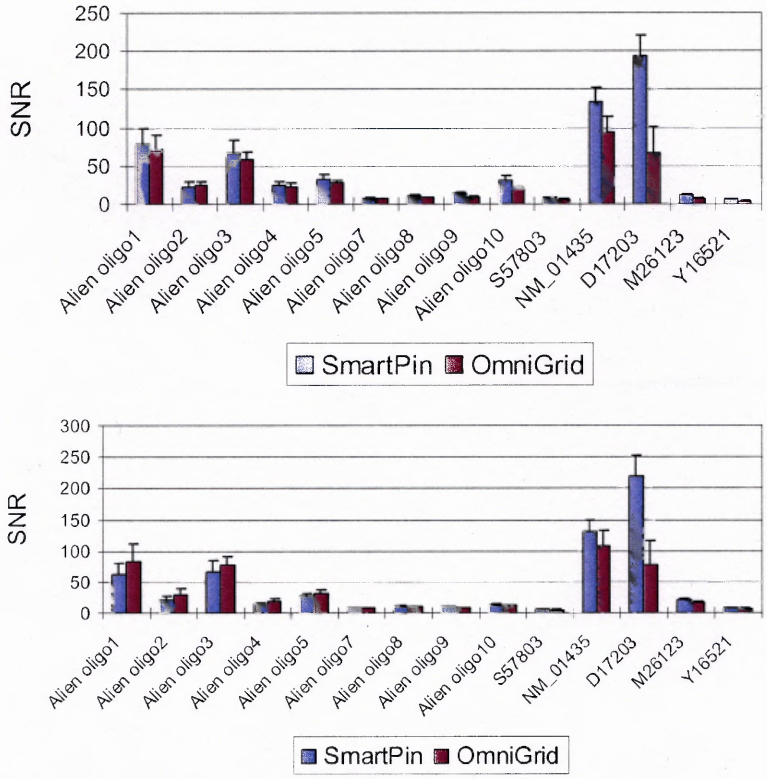

Figure 4.11 Average SNR F635 (top) and F532 (bottom) of 6 slides.

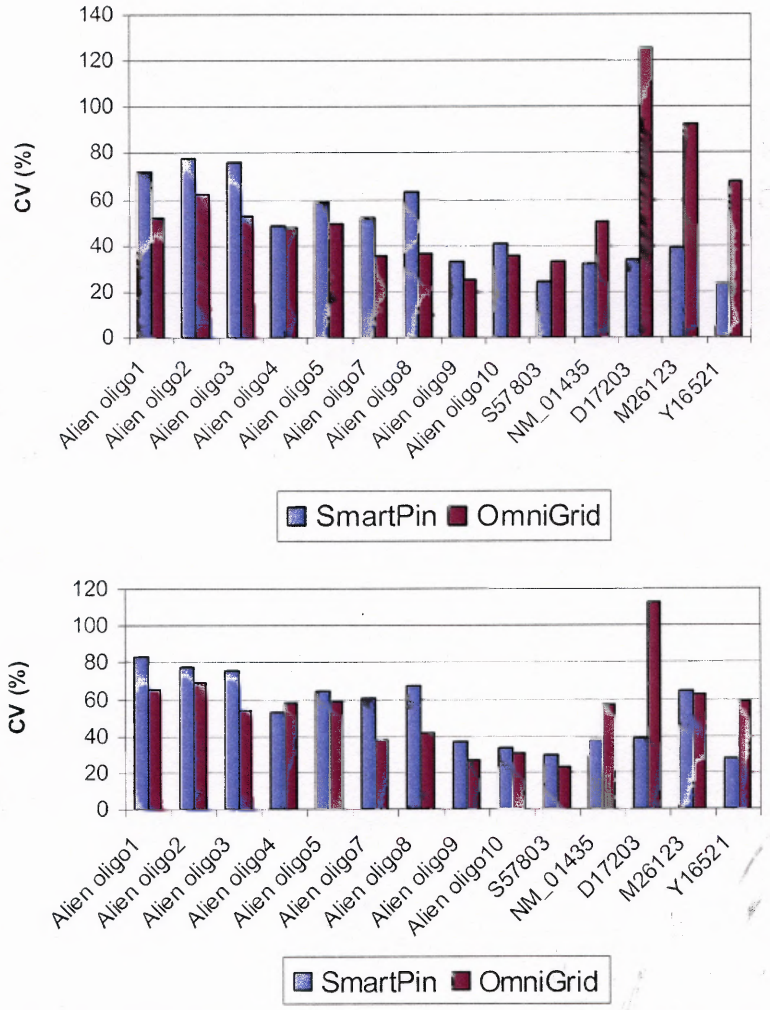

Figure 4.12 F635 (top) and F532 (bottom) median intensity CVs of 6 slides.

4.3 Micro-Lines and Micro-Squares

To verify the performance of the SmartPin in line formation, two types of line-drawing experiments have been carried out for each of the abovementioned approaches. In the first experiment, the SmartPin draws a 2 millimeter straight line while in the second experiment; the SmartPin draws a 1mm side square. In both cases, the opening of the pin tip is 60 microns. The sample liquid is 3X SSC salt buffer solution with 0.3% of fluorescent Cy3 dye. The humidity and temperature is kept at 60% and 24 degree Celsius.

The step size along the line direction is 10 micron. The results are scanned by a GeneTAC UC-4 microarray scanner with green laser set at intensity level of 30 and resolution at 10 micron.

The line and square scan images are shown in Figure 4.13 and Figure 4.14, respectively. It is observed that the squares drawn by the spot-sequence method is not as uniform as those by the liquid-column-sweeping method. It is also observed that both of these two approaches can achieve the same level of line width and constancy.

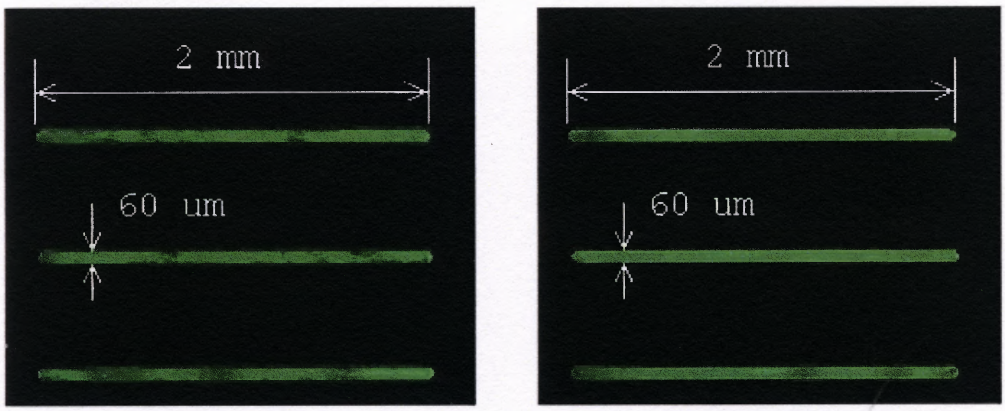

Figure 4.13 Scan images of micro-lines drawn by spot-sequence (left) and liquid-column-sweeping approaches.

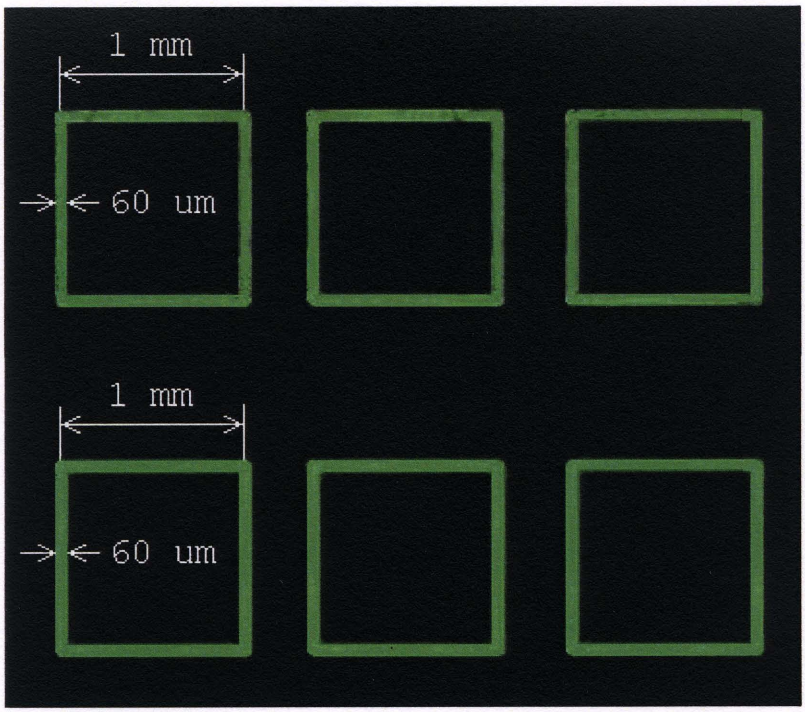

Figure 4.14 Scan images of micro-squares drawn by spot-sequence (top) and liquid-column-sweeping approaches.

Shown in Figure 4.15 and Figure 4.16 are the time history of the spot-sequence approach and the sweeping approach for drawing a 1mm-side square. It is readily noted that spot-sequence approach is less time efficient. While Figure 4.15 only shows one tenth of the entire curve for spot-sequence method, the total time for this method is 400 seconds while that for the liquid-column method is only 65 seconds. For the aspect of material usage, the spot-sequence method consumes 7.2 nanoliter for each square while the liquid-column-sweeping method only consumes about 40 picoliter.

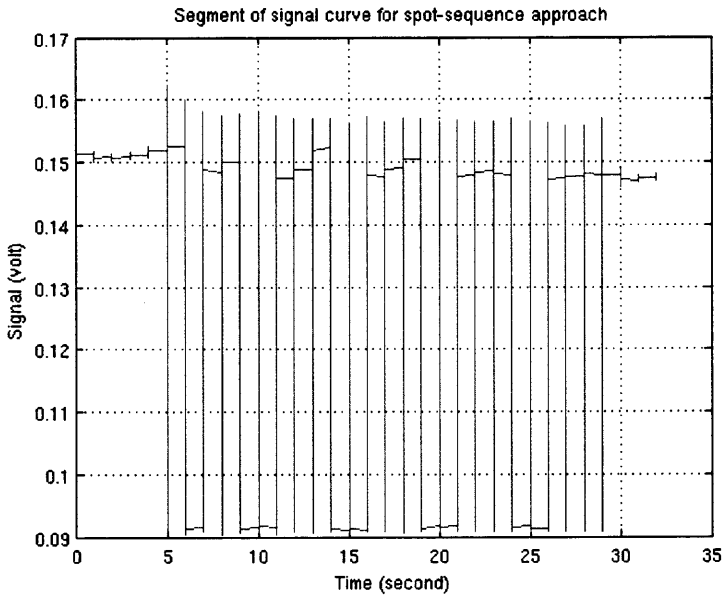

Figure 4.15 A segment of signal curve for spot-sequence approach when drawing a 1x1 mm square.

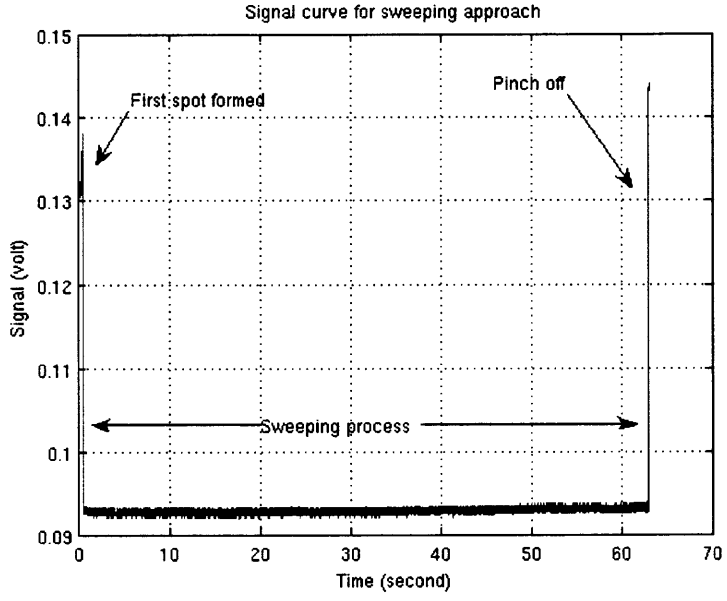

Figure 4.16 Signal curve for liquid-column-sweeping approach when drawing a 1x1 mm square.

To evaluate the quality of the micro-line and micro-squares quantitatively, Figure 4.13 and Figure 4.14 were converted into grayscale images as shown in Figure 4.17 through Figure 4.20 (left side images). The pixel intensity profiles were calculated from these grayscale images (right side images).

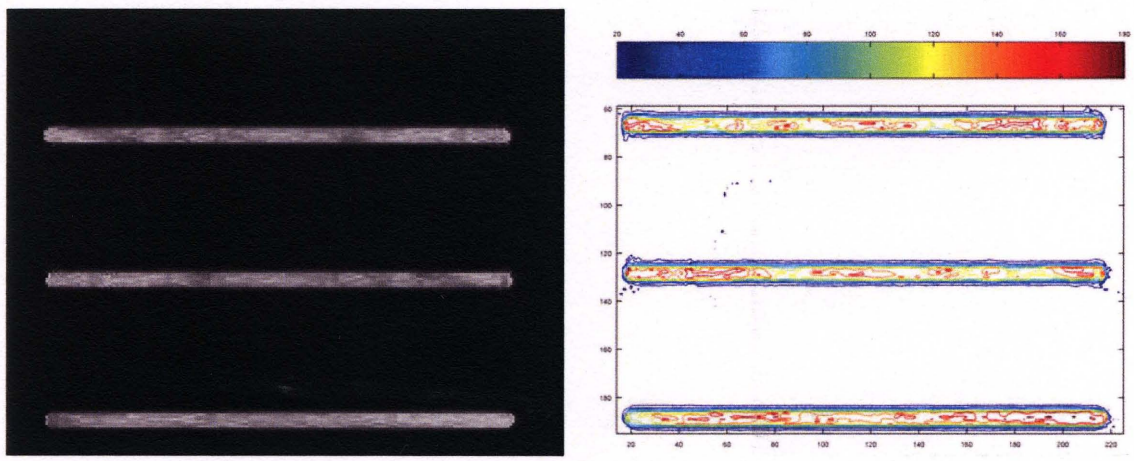

Figure 4.17 Grayscale image (left) and pixel intensity profile (right) of micro-lines drawn by spot sequence method.

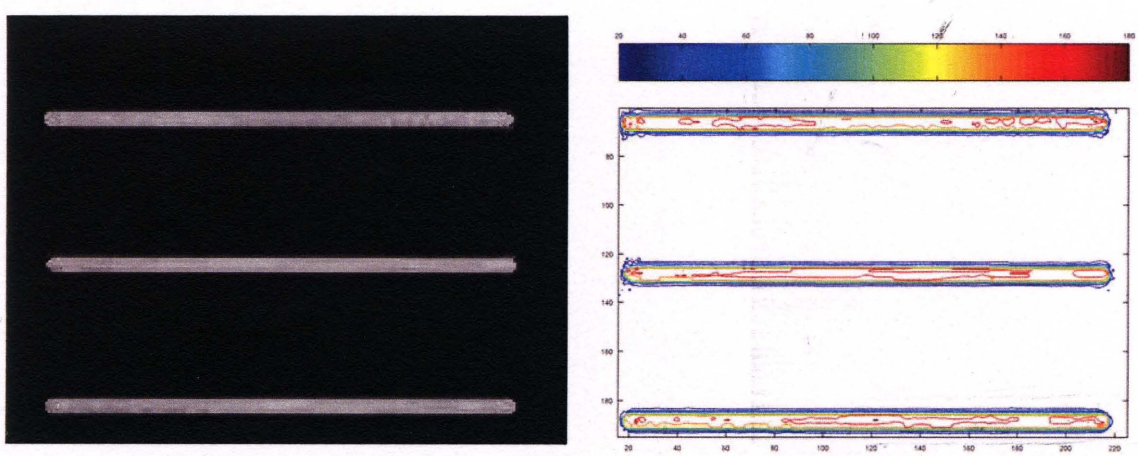

Figure 4.18 Grayscale image (left) and pixel intensity profile (right) of micro-lines drawn by liquid column sweeping method.

Table 4.2 Comparison of Average and Standard Deviation of Pixel Intensity of Micro-lines

	Spot Sequence Method		Liquid Column Sweeping Method	
	Average Intensity	Std. Deviation	Average Intensity	Std. Deviation
Line 1	26.89	53.21	30.49	45.19
Line 2	23.38	48.17	32.24	44.15
Line 3	30.69	57.77	37.14	46.27

Table 4.3 Comparison of Average and Standard Deviation of Pixel Intensity of Micro-squres

	Spot Sequence Method		Liquid Column Sweeping Method	
	Average Intensity	Std. Deviation	Average Intensity	Std. Deviation
Square 1	25.37	54.42	33.21	44.13
Square 2	24.41	49.23	35.33	42.85
Square 3	31.35	58.64	39.73	47.29

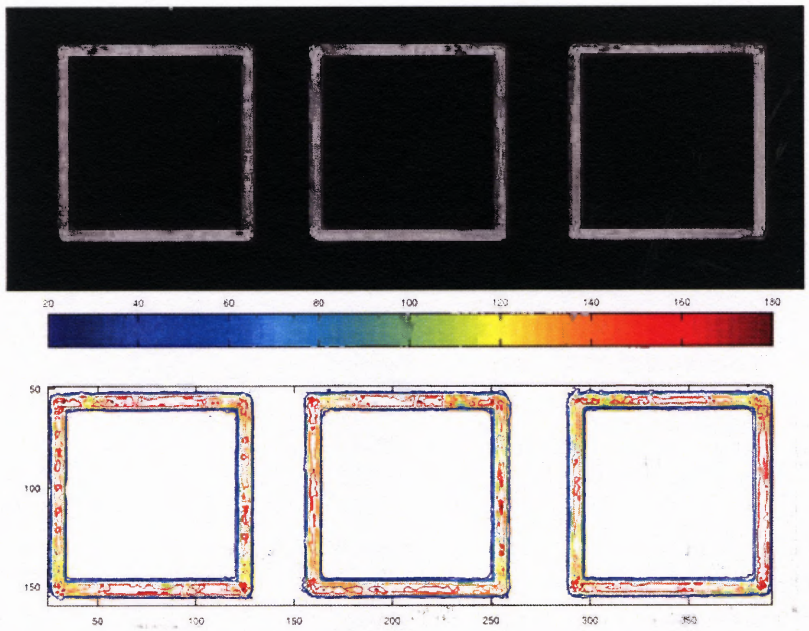

Figure 4.19 Grayscale image (top) and pixel intensity profile (bottom) of micro-squares drawn with spot sequence method.

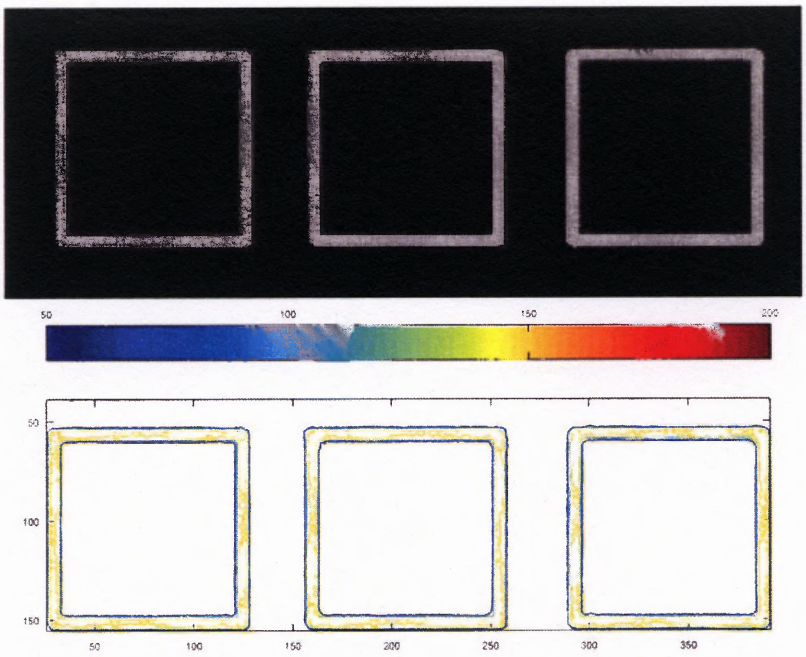

Figure 4.20 Grayscale image (top) and pixel intensity profile (bottom) of micro-squares drawn with liquid column sweeping method.

CHAPTER 5

SIMULATION OF LIQUID DISPENSING PROCESS

Through extensive experiments with saline solution (primarily the 3xSSC type), fundamental knowledge on the liquid dispensing process of has been established not only as template database for diagnostic purpose but also as guide for design of control system. However, to further explore scalability and applications of the SmartPin, knowledge on liquid dispensing process of multiple types of liquids on different types of substrates is necessary. Although exhaustive experiments, as before, on each possible combination of liquid and substrate can be conducted, it is time consuming and expensive in terms of cost on materials. Therefore, study on the use of computational fluid dynamics (CFD) software for simulating the spotting process is of interest. In this chapter, detailed procedure and related theoretical background of GAMBIT and FLUENT, which are state-of-the-art computer programs for modeling fluid flow and heat transfer in complex geometries, are studied and utilized effectively on liquid dispensing process involved in the SmartPin system.

5.1 Literature Survey

Recent researches on droplets of non-Newtonian fluids include: Belblidia et al. (2008) considered compatibility of function spaces for stress/velocity-gradient approximation under subcell discretisation for viscoelastic flow. Matallah et al. (2006) analysed the transient viscoelastic response of strain-hardening fluids in filament stretching flows by utilizing an arbitrary Lagrangian/Eulerian temporal approach (ALE). Matallah et al.

(2007) did a computational investigation of filament stretching at high Hencky-strains, extending the predictions on the multi-mode side through advance in Hencky-strain and single-mode predictions via rheological variation, with the additional consideration of linear versus exponential stretching configurations using the Oldroyd-B model. Sujatha et al. (2006) investigated the consequences of employing both finite-element and finite-volume spatial discretisations within an incremental pressure-correction scheme, considering various mesh movement and free-surface tracking techniques for dynamics of filament stretching of viscoelastic liquids. Sujatha et al. (2008) discussed the numerical modeling of capillary break-up extensional rheometer procedures (CaBER) using arbitrary Lagrangian/Eulerian (ALE) methods. Webster et al. (2008) addressed the modelling of filament-stretching/step-strain deformation under viscoelastic capillary break-up configurations of the CaBER-type. Deng et al. (2006) put forward an idea of phasing study fluid transferring mechanism and dividing the fluid transferring process into four different phases in contact dispensing dot.

Recent researches on droplets of Newtonian fluids include: Korlie et al. (2008) developed a volume of fluid (VOF) type code for the direct numerical simulation of two-fluid configurations of magnetic fluids with dynamic interfaces. Kerboua et al. (2008) developed a computational model in order to analyze the dynamic behavior of coupled fluid-structure systems such as liquid containers and a set of parallel or radial plates. Ding et al. (2007) investigated numerically the axial symmetric droplet spreading at relatively large rates of spreading, such that inertial effects become important. Khatavkar et al. (2007) studied the spreading of a liquid droplet on a smooth solid surface in the partially wetting regime by using a diffuse-interface model based on the Cahn - Hilliard

theory. Krogmann et al. (2006) presented an opto-electrowetting system allowing both pushing and pulling a droplet. Bayer et al. (2006) revealed the dynamic behavior of the apparent (macroscopic) contact angle θ and its dependence on contact line velocity VCL at various degrees of surface wetting. Purvis et al. (2004) studied the nonlinear integro-differential system for the evolution of the interface and induced pressure for pre-impact surface tension effects, which significantly delay impact, and for post-impact interaction phenomena which include significant decrease of the droplet spread rate. Hong et al. (2003) compared numerical solutions and analytical solutions of fluid dynamics. Reznik et al. (2002) studied spreading of a drop on a plane dry wall due to gravity and capillarity in the the inertialess approximation for arbitrary Bond number. Yildirim et al. (2001) investigated the role of shearing-thinning in suppressing long threds. Kim et al. (2001) studied the recoiling behavior of different liquid droplets (water, ink, and silicone oil) on different solid surfaces (polycarbonate and silicon oxide). Chen (2000) developed a model for the time-pressure fluid dispensing process, by which the flow rate and shape can be established. Zhang (1999) developed a numerical model to predict the evolution of the drop shape and its breakup based on the volume-of-fluid/continuum-surface-force method. Fuchikami et al. (1999) simulated a dripping faucet system.

Despite the above mentioned researches, the fluid dynamics of a pico-liter volumed droplet, while still hanging on the outlet of a tiny pin tip, in the process of spreading onto a glass surface and elongated by motion of glass surface till pinch-off are still left unanswered. Therefore, it is of interest to investigate such process by computational fluid dynamics method.

5.2 On the Computational Fluid Dynamics (CFD)

The governing equations to describe the transport of mass and momentum for Newtonian fluids ($\tau \propto \frac{\partial u}{\partial y}$) are Navier-Stokes Equations which have vector forms of

$$\rho\left(\frac{\partial v}{\partial t}+\mathbf{v}\cdot\nabla\mathbf{v}\right)=-\nabla p+\nabla\cdot\left\{\mu\cdot\left[\nabla\mathbf{v}+(\nabla\mathbf{v})^{T}\right]\right\}+\nabla(\lambda\nabla\cdot\mathbf{v})+\mathbf{f} \tag{5.1}$$

$$\frac{\partial\rho}{\partial t}+\nabla\cdot(\rho\mathbf{v})=0 \tag{5.2}$$

$$\rho\frac{Dh}{Dt}=\frac{Dp}{Dt}+\nabla\cdot(k\nabla T)+\Phi \tag{5.3}$$

$$\begin{aligned}\Phi=\mu\Bigg[&2\left(\frac{\partial u}{\partial x}\right)^{2}+2\left(\frac{\partial v}{\partial y}\right)^{2}+2\left(\frac{\partial w}{\partial z}\right)^{2}\\&+\left(\frac{\partial v}{\partial x}+\frac{\partial u}{\partial y}\right)^{2}+\left(\frac{\partial w}{\partial y}+\frac{\partial v}{\partial z}\right)^{2}+\left(\frac{\partial u}{\partial z}+\frac{\partial w}{\partial x}\right)^{2}\Bigg]+\lambda(\nabla\cdot\mathbf{v})^{2}\end{aligned} \tag{5.4}$$

where

ρ is the density of the fluid.

$\mathbf{V} = (u, v, w)$ is the velocity vector of the fluid.

p is the pressure.

μ is the first coefficient of viscosity.

λ is the second coefficient of viscosity.

$\mathbf{f}$ is other forces such as gravity force.

$\frac{D(*)}{Dt}$ is convective derivative operator defined as $\frac{\partial}{\partial t}(*)+\mathbf{v}\cdot\nabla(*)$.

h is enthalpy.

T is the temperature.

Φ is a function representing the dissipation of energy due to viscous effects.

The Navier-Stokes equations consists of a time-dependent conservation of momentum Equation (5.1), a time-dependent continuity equation for conservation of mass (5.2) and a time-dependent conservation of energy Equation (5.3). These equations describe how the velocity, pressure, temperature, and density of a moving fluid are related. There are four independent variables: the Cartesian coordinates x, y, and z, and the time t; six dependent variables: the pressure p, density ρ, temperature T, and the three components of the velocity vector u, v, and w. Although, in theory, these coupled partial differential equations could be solved for a given flow problems using methods from calculus, it is too difficult to solve them analytically in practice.

As the computer technology and numerical mathematics have developed rapidly, a new branch of fluid mechanics, computational fluid dynamics (CFD), that uses numerical methods and algorithms to solve and analyze problems that involve fluid flows has emerged and developed rapidly as well. In brief, CFD is the science of predicting fluid flow, heat and mass transfer, chemical reactions, and related phenomena by solving numerically the set of governing mathematical equations (conservation of mass, conservation of momentum, conservation of energy, conservation of species, etc.) The results of CFD analyses are relevant in conceptual studies of new designs, detailed product development, troubleshooting, and redesign. And the CFD analysis complements testing and experimentation in that it reduces the total effort required in the experiment design and data acquisition.

Among numerous CFD preprocessors and solvers, GAMBIT and FLUENT, , which are state-of-the-art computer programs for modeling fluid flow and heat transfer in

complex geometries, are chosen in this work because they have been used in academic institutes for many years and have very good support services.

5.3 Problem Description of the Liquid Dispensing Process

Since the pin is axially symmetrical, the problem can be simplified as a 2-D problem. The schematic of the problem is shown in Figure 5.1. The very tip portion of the pulled glass pin is placed in ambient air. The pin is filled with water which forms a downwardly concaved bulge. The diameter of the orifice of the pin tip is 60 um, the diameter of the upper side of the pin tip is 70 um, and height of the pin tip is 30 um. Thus, the taper angle of the pin tip is of 9.46 degree. The height of the liquid bulge is 10 um. The air domain is a 120 by 65 um rectangle. The glass slide is defined as a 110 by 5 um rectangle.

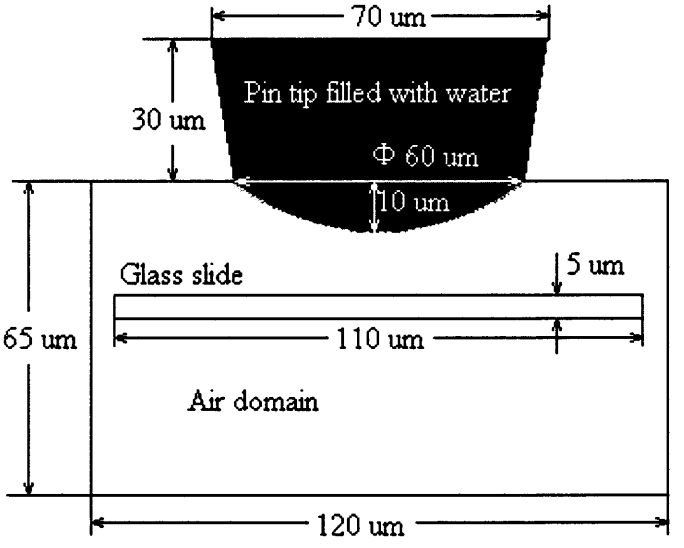

Figure 5.1 Schematic of liquid dispensing process.

The motion of the glass slide is divided into three periods. In the first period, the glass slide moves upwardly with speed of 0.5 m/s (i.e., 0.5 um/us). The second period

starts when the surface of the glass slide touches the tip of the liquid bulge. In this period, the glass slide stays put for 20 us. Then, the third period of motion of the glass slide begins by departing from the liquid with speed of 0.5 m/s (i.e., 0.5 um/us) until the elongated liquid column pinches off.

Since the interest of simulation is focused on the deformation of the liquid bulge, the first period of the motion of the glass pin is skipped in the simulation.

5.4 CFD Preprocessing in GAMBIT

As the first step of the CFD analysis, the geometry and associate mesh must be created before any further processing.

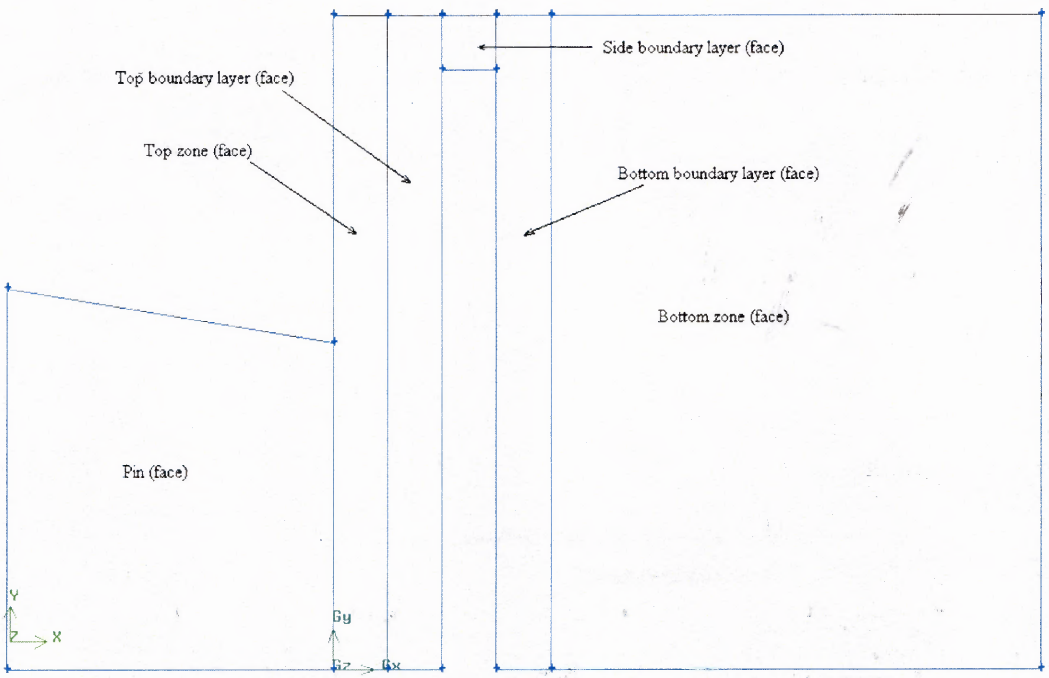

Figure 5.2 Geometries of fluid/solid domains created in GAMBIT (Unit: um).

5.4.1 The Geometries of Fluid/Solid Domains

Since the problem is defined as 2-D axial symmetric problem, only half of the complete geometries of fluid/solid domains have to be created (as shown in Figure 5.2). The symmetry axis must lie along the X-axis of the coordinate system. Each face has to be constructed by atomic lines, i.e., there must not be any third point on a line in between the two end points. This construction will make FLUENT to consider the border between each two adjacent faces as fluid continuity. The reason to create boundary layers is that finer mesh can be created in these zones to get more precise results on the critical locations where the liquid deformation takes place mostly. The glass slide is actually a solid domain enclosed by fluid. Therefore, there is no need to create dedicated face for it.

5.4.2 The Meshes of Fluid/Solid Domains

Each face is meshed separately to get structural mesh as shown in Figure 5.3. The interval size of mesh for the pin face, top zone, and bottom zone is 0.5 um by 0.5 um. The interval size of mesh for the boundary layers is 0.5 um by 0.2 um. The element type for mesh is "Quad", meshing type is "Map", and no smoother. However, nodes must be created on the smaller side of the pin face to force grids on both side of it continuous. So do the sides of boundary layers where the mesh interval size is 0.2 um.

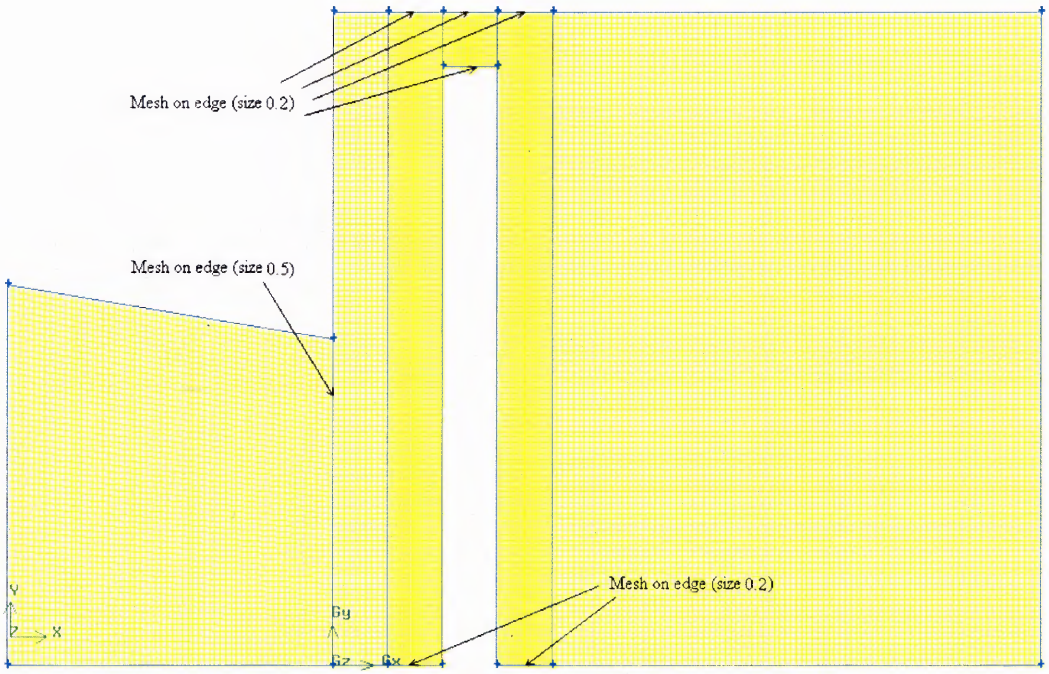

Figure 5.3 Meshes of fluid/solid domains created in GAMBIT (Unit: um)

5.4.3 The Boundary Types and Zones

As the last step of preprocessing, boundaries and zones have to be defined for CFD processor to identify each entity. Figure 5.4 shows the boundary types and zones created in this work.

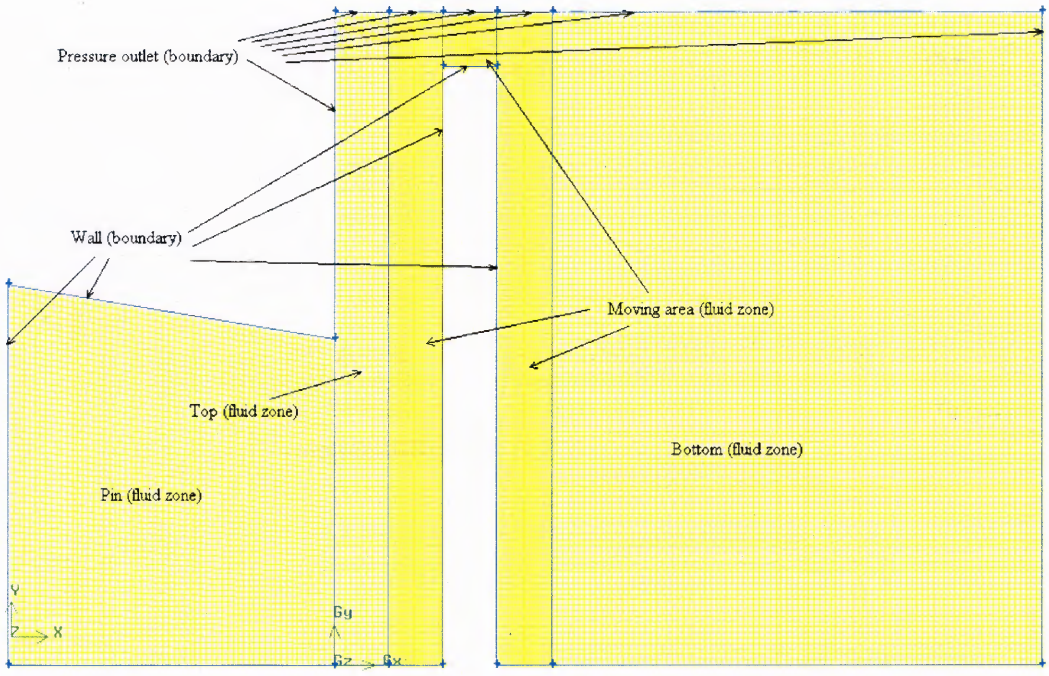

Figure 5.4 Boundary types and zones defined in GAMBIT

The boundary types defined in GAMBIT are superficial because their purpose is for identification, not for computation. In FLUENT, there will be detailed settings on each boundary. The top fluid zone and bottom fluid zone must be defined separately otherwise FLUENT cannot generate the interior border between top zone and moving area, and interior border between bottom zone and moving area.

5.5 CFD Analysis in FLUENT

5.5.1 The Basic Preparation

Since the scale of the problem to be solved is in the order of micron, the double precision 2d version of FLUENT is needed. Some routine steps are necessary to get the solver ready. First, the mesh file exported from GAMBIT has to be read, scaled, and plotted. The scale for this problem is 1e-6 for both X- and Y-direction. The units for length and

surface tension are mm and dyn/cm respectively. To view the grid properly, the mirroring about the axis is enabled, and the camera has to be rotate counterclockwise to output the geometry upwards (as shown in Figure 5.5).

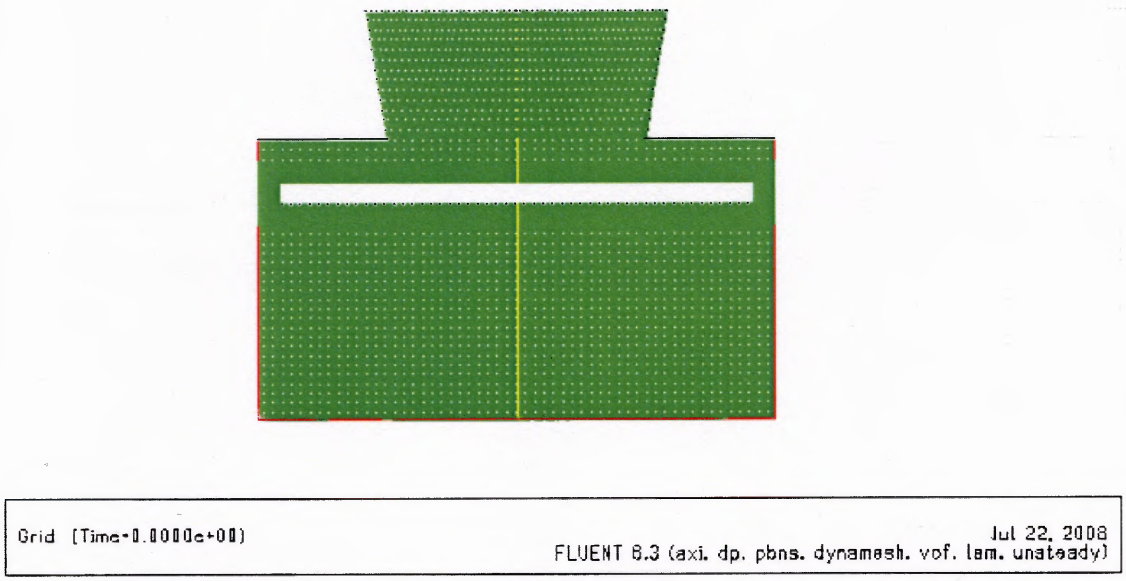

Figure 5.5 Boundaries and zones defined in FLUENT

Table 5.1 and 5.2 list the physical properties of air and water from the material library of FLUENT.

Table 5.1 Physical Properties of Air

Density (kg/m^3)	1.225	Cp (j/kg-k)	1006.43
Thermal Conductivity (w/m-k)	0.0242	Viscosity (kg/m-s)	1.7894e-5
Molecular Weight (kg/kgmol)	28.966	L-J Characteristic Length (angstrom)	3.711
L-J Energy Parameter (k)	78.6	Thermal Accommodation Coefficient	0.9137
Momentum Accommodation Coefficient	0.9137		

Table 5.2 Physical Properties of Water

Density (kg/m^3)	998.2	Cp (j/kg-k)	4182
Thermal Conductivity (w/m-k)	0.6	Viscosity (kg/m-s)	0.001003
Molecular Weight (kg/kgmol)	18.0152	Standard State Enthalpy	-2.858412e+8
Standard State Enthropy (j/kgmol-k)	69902.21	Reference Temperature (k)	298
Latent Heat (j/kg)	2263073	Vaporization Temperature (k)	284
Boiling Point (k)	373	Volatile Component Fraction	100%
Binary Diffusivity (m^2/s)	3.05e-5	Saturation Vapor Pressure (Pa)	2658
Droplet Surface Tension (dyn/cm)	71.9404	Equilibrium Species Phase for PDF model	1

The operating conditions are: 101325 Pa operating pressure, reference pressure location is at (0, 0.06) mm, gravitational acceleration is (9.81 m/s^2, 0).

5.5.2 The User Defined Function (UDF) for Moving Parts

The user defined function (UDF) is a piece of C language program which will be compiled, loaded into and called by FLUENT solver during each iteration. Appendix A lists the source code and comments of the UDF defining motion of glass slide.

5.5.3 Dynamic Meshing

The dynamic mesh model in FLUENT can be used to model flows where the shape of the domain is changing with time due to motion on the domain boundaries. The dynamic layering method, among others, is used in this work to implement dynamic mesh. In prismatic mesh zones, this method adds for remove layers of cells adjacent to a moving boundary, based on the height of the layer adjacent to the moving surface. The dynamic mesh model in FLUENT allows to specify an ideal layer height on each moving

boundary. The layer of cells adjacent to the moving boundary (layer *j* in Figure 5.6) is split or merged with the layer of cells next to it (layer *i* in Figure 5.6) based on the height (*h*) of the cells in layer *j*.

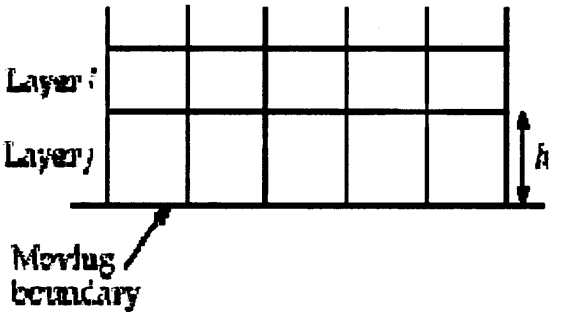

Figure 5.6 Schematic of layering method for dynamic meshing.

If the cells in layer j are expanding, the cell heights are allowed to increase until

$$h_{\min} > (1+\alpha_s) h_{\text{ideal}} \tag{5.5}$$

where $h_{\min}$ is the minimum cell height of cell layer *j*, h_{ideal} is the ideal cell height, and α_s is the layer split factor. When this condition is met, the cells are split based on the specified layering option. With the constant height option, the cells are split to create a layer of cells with constant height h_{ideal} and a layer of cells of height h-h_{ideal}.

In this work, the constant height option is selected, the split factor is 0.4, the collapse factor is 0.04, and the ideal cell height is 0.5 um. Figure 5.7 shows the dynamic mesh zones defined in this work.

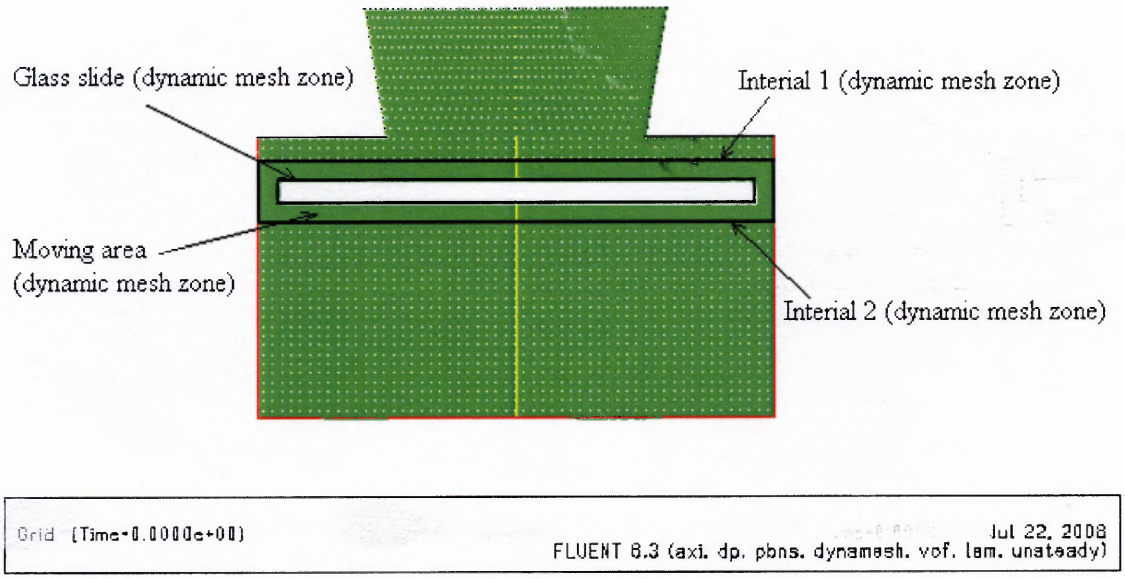

Figure 5.7 Zones that need dynamic meshing.

After UDF is compiled, loaded, and dynamic mesh parameters and zones are defined, FLUENT allows previewing the dynamic mesh results before solving the problem. Figure 5.8 and Figure 5.9 show the state of mesh at 70 us and 90 us. The mesh states in the preview match the motion of glass slide defined in UDF.

5.5.4 Volume of Fluid (VOF) Model for Multiphase Flow

A phase is a class of matter with a definable boundary and a particular dynamic response to the surrounding flow/potential field. Phases are generally identified by solid, liquid or gaseous states of matter. Multiphase flow is simultaneous flow of materials with different states or phases (i.e., gas, liquid or solid), or materials with different chemical properties but in the same state or phase (i.e., liquid-liquid, such as, oil-water).

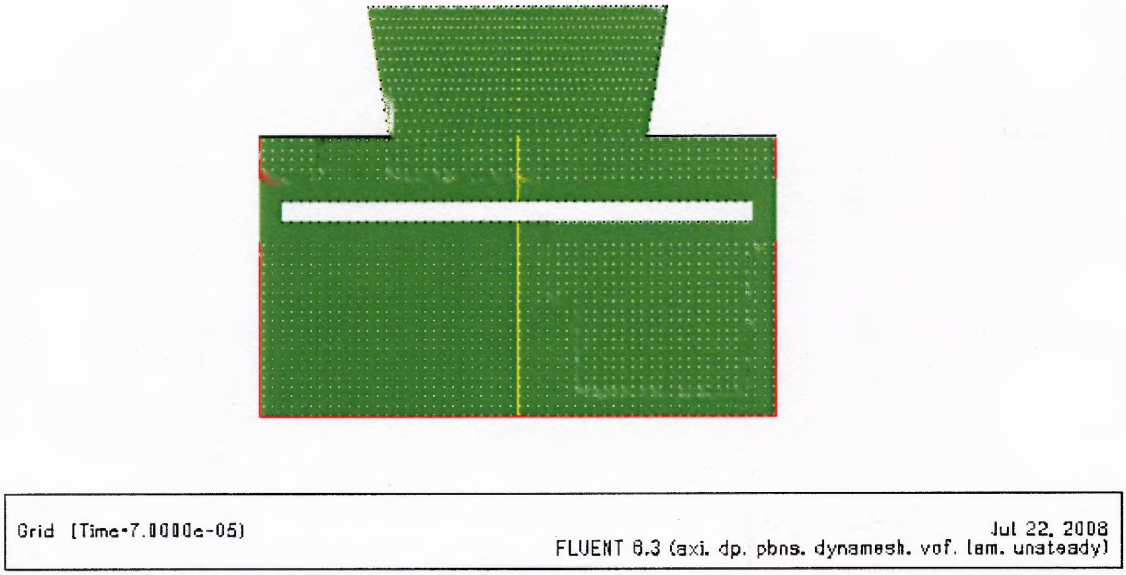

Figure 5.8 Mesh preview at 70 us

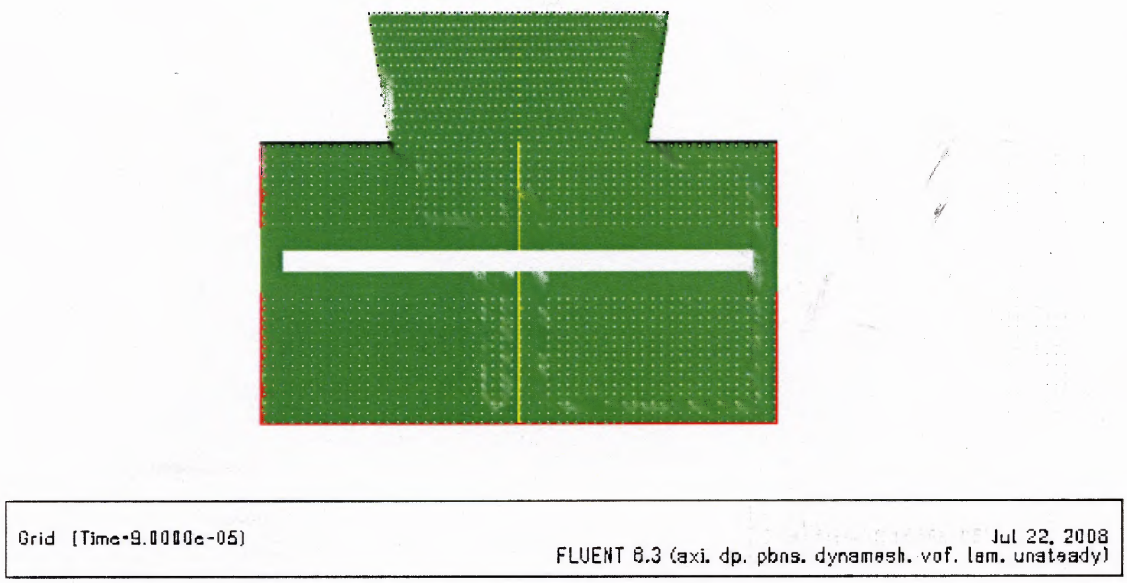

Figure 5.9 Mesh preview at 90 us

Discrete fluid droplets in a continuous gas in this research work is a typical case of multiphase flow regimes which can be modeled by direct method of predicting interface shape between immiscible phases – volume of fluid (VOF) model in FLUENT.

The tracking of the interface between the phases is accomplished by the solution of a continuity equation for the volume fraction of one (or more) of the phases. For the q^{th} phase, this equation has the form of

$$\frac{1}{\rho_q}\left[\frac{\partial}{\partial t}\left(\alpha_q \rho_q\right)+\nabla\cdot\left(\alpha_q \rho_q \mathbf{v}_q\right)=S_{\alpha_q}+\sum_{p=1}^{n}\left(\dot{m}_{pq}-\dot{m}_{qp}\right)\right] \tag{5.6}$$

where $\dot{m}_{qp}$ is the mass transfer from phase q to phase p and $\dot{m}_{pq}$ is the mass transfer from phase p to phase q. By default the source term S_{α_q} is zero. The volume fraction equation will not be solved for the primary phase. Instead, the primary-phase volume fraction will be computed based on the following constraint:

$$\sum_{q=1}^{n}\alpha_q = 1 \tag{5.7}$$

The volume fraction equation is solved through implicit time discretization. When the implicit scheme is used, FLUENT's standard finite-difference interpolation schemes, QUICK, 2nd Order Upwind and 1st Order Upwind, are used to obtain the face fluxes for all cells, including those near the interface.

$$\frac{\alpha_q^{n+1}\rho_q^{n+1}-a_q^n\rho_q^n}{\Delta t}V+\sum_f\left(\rho_q^{n+1}U_f^{n+1}\alpha_{q,f}^{n+1}\right)=\left[S_{\alpha_q}+\sum_{p=1}^{n}\left(\dot{m}_{pq}-\dot{m}_{qp}\right)\right]V \tag{5.8}$$

Since this equation requires the volume fraction values at the current time step, a standard scalar transport equation is solved iteratively for each of the secondary-phase volume fractions at each time step.

The properties appearing in the transport equations are determined by the presence of the component phases in each control volume. In general, the volume-fraction-averaged density for an n-phase system is given by

$$\rho = \sum_{q=1}^{n} \alpha_q \rho_q \tag{5.9}$$

All other properties are computed in the same manner. A single momentum equation is solved throughout the domain, and the resulting velocity vector is shared among the phases. The energy equation is also shared among the phases.

The VOF model also includes the effects of surface tension along the interface between each pair of phases. The model can be augmented by the additional specification of the contact angles between the phases and the walls. The solver will include the additional tangential stress terms that arise due to the variation in surface tension coefficient.

Surface tension arises as a result of attractive forces between molecules in a fluid. The surface tension model in FLUENT is the continuum surface force model with which the addition of surface tension to the VOF calculation results in a source term in the momentum equation. In FLUENT, the surface curvature is computed from local gradients in the surface normal at the interface. Let **n** be the surface normal, defined as the gradient of α_q, the volume fraction of the q^{th} phase.

$$\mathbf{n} = \nabla \alpha_q \tag{5.10}$$

The curvature, κ is defined in terms of the divergence of the unit normal $\hat{\mathbf{n}}$,

$$\kappa = \nabla \cdot \hat{\mathbf{n}} \tag{5.11}$$

The surface tension can be written in terms of the pressure jump across the surface. The force at the surface can be expressed as a volume force using the divergence

theorem. It is this volume force that is the source term which is added to the momentum equation. It has the form of

$$\mathbf{F}_{\text{vol}} = \sum_{\text{pairs } ij, i<j} \delta_{ij} \frac{\alpha_i \rho_i \kappa_j \nabla \alpha_j + \alpha_j \rho_j \kappa_i \nabla \alpha_i}{0.5\left(\rho_i + \rho_j\right)} \tag{5.12}$$

An option to specify a wall adhesion angle in conjunction with the surface tension model is also available in the VOF model. If θ_{wall} is the contact angle at the wall, then the surface normal at the live cell next to the wall is

$$\hat{\mathbf{n}} = \hat{\mathbf{n}}_{\text{wall}} \cos\theta_{\text{wall}} + \hat{\mathbf{t}}_{\text{wall}} \sin\theta_{\text{wall}} \tag{5.13}$$

where $\hat{\mathbf{n}}_{\text{wall}}$ and $\hat{\mathbf{t}}_{\text{wall}}$ are the unit vectors normal and tangential to the wall, respectively. The contact angle is the angle between the wall the tangent to the interface at the wall measured. In this work, the contact angle on the pin wall and the glass slide wall is 30 degree. The backflow volume fraction on the pressure outlet is 0.

5.5.5 Adaption and Solution

The solution-adaptive mesh refinement feature of FLUENT allows user to refine and/or coarsen the grid based on geometric and numerical solution data. In this work, a circle region whose center is at (0, 0.04) mm and radius of 0.05 mm is adapted and filled with water initially, such that the liquid bulge has height of 10 um.

The real iteration of the solver takes variable time step range from 1e-9 s to 1e-8 sec, and 10 as maximum iterations per time step. Figure 5.10 (a) through (f) shows some characteristic states of the simulation.

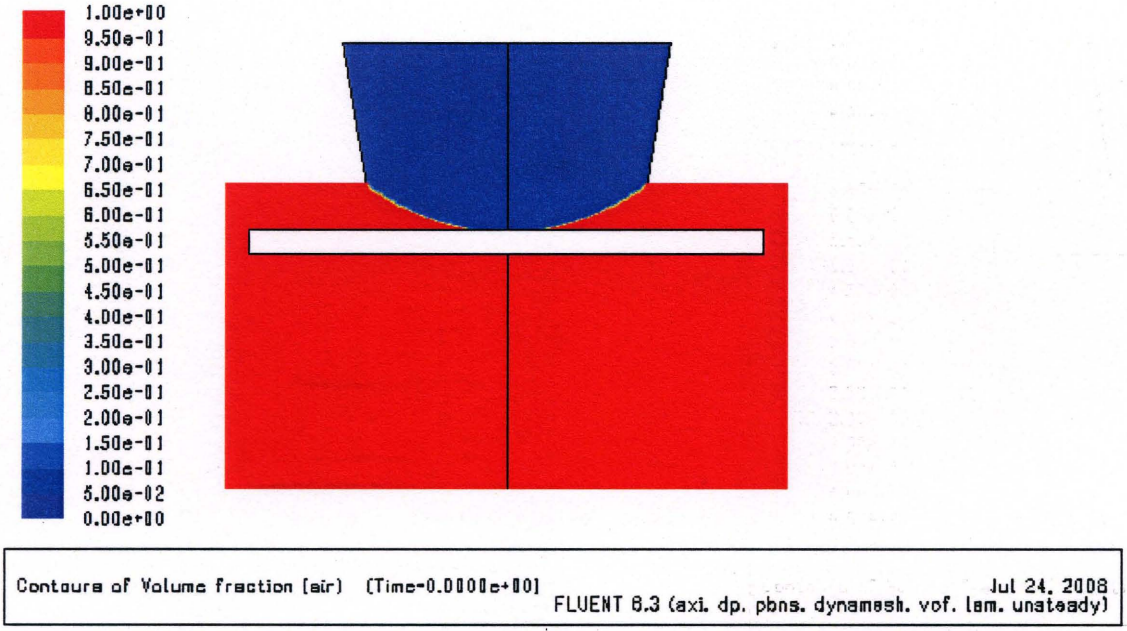

(a) The moment when the liquid bulge touches the glass slide.

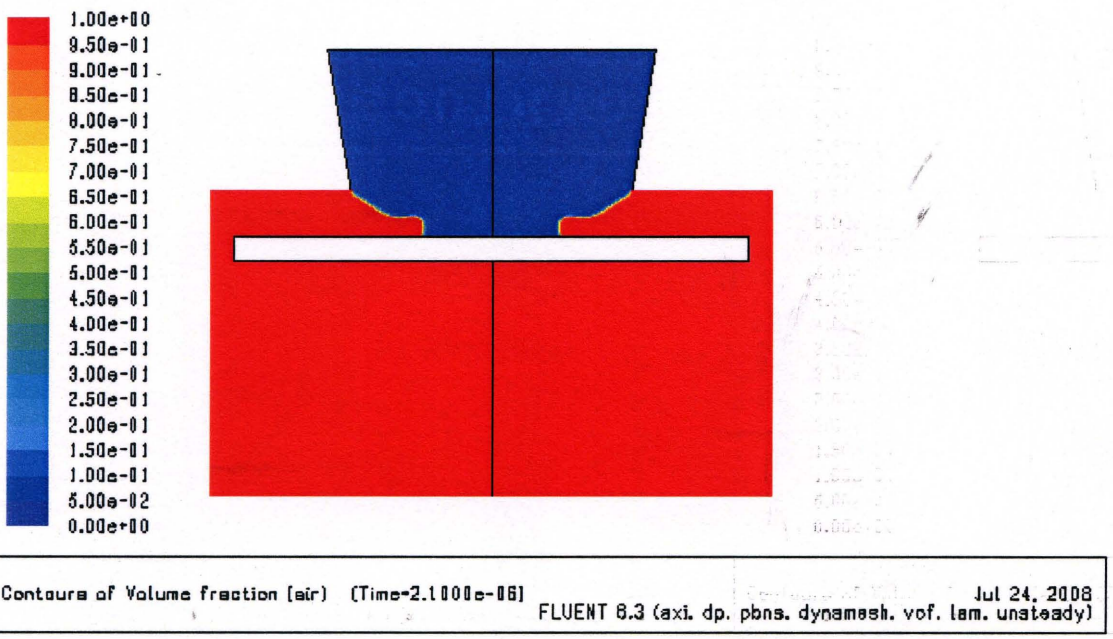

(b) One moment during the liquid bulge is deforming due to surface tension.

Figure 5.10 Snapshots of critical states of liquid dispensing process simulation, (a) and (b).

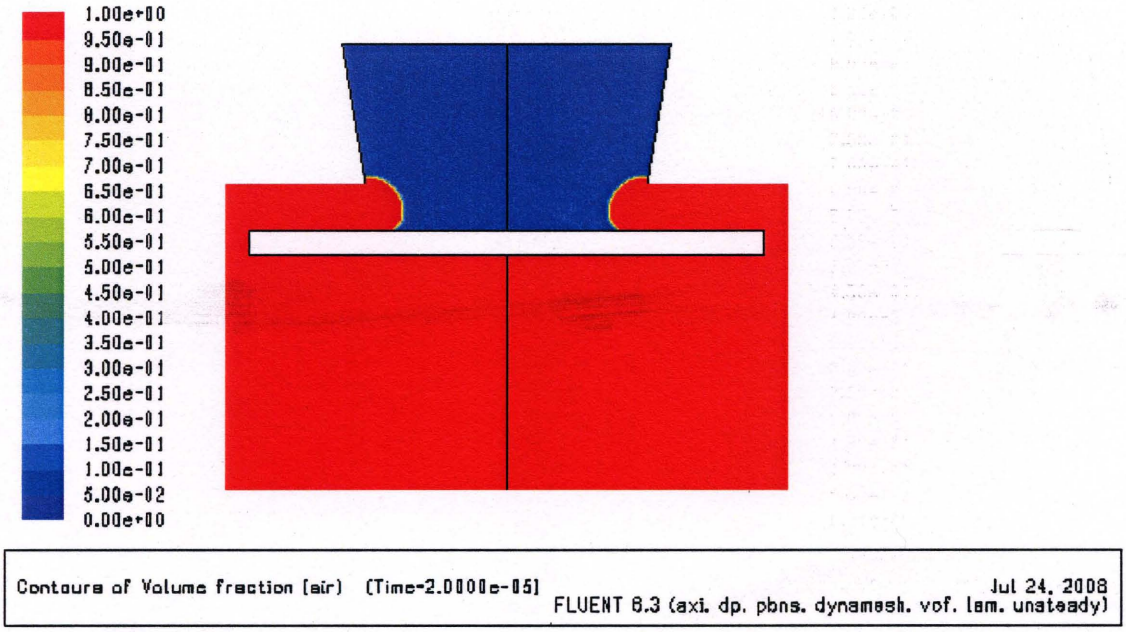

(c) The moment when deformed liquid bulge reaches its equilibrium.

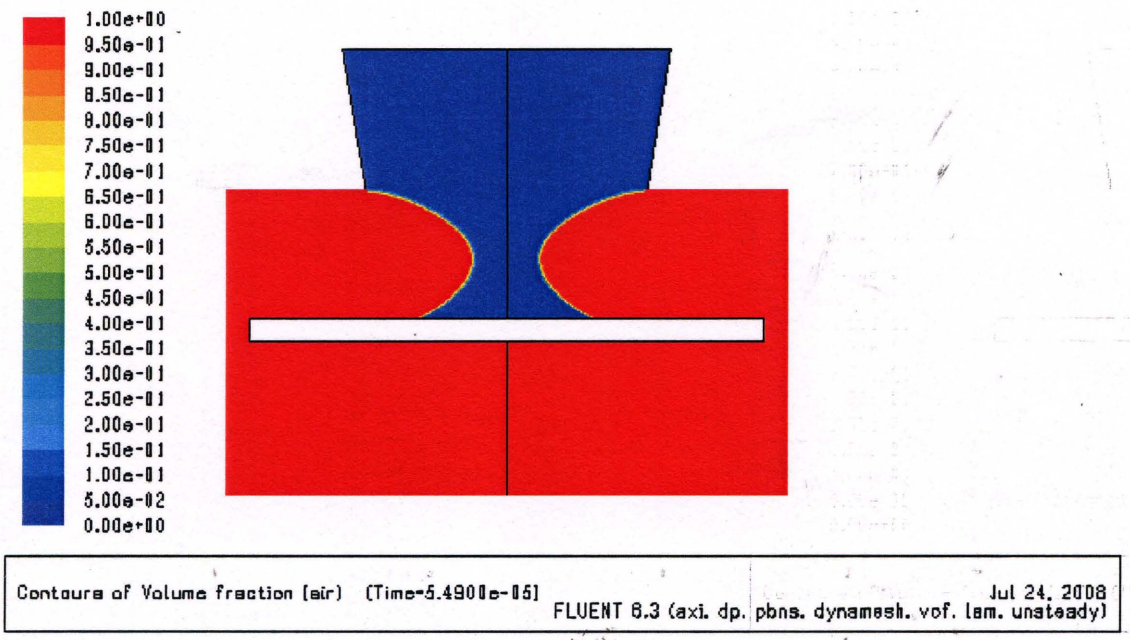

(d) One moment of liquid column elongation.

Figure 5.10 Snapshots of critical states of liquid dispensing process simulation, (c) and (d).

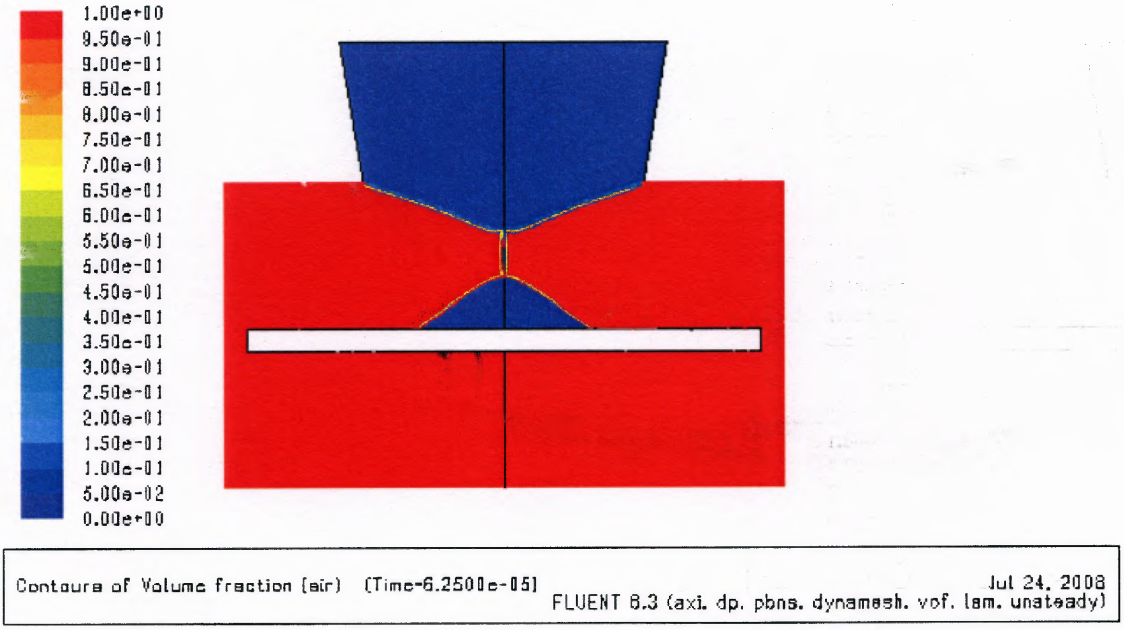

(e) The very moment when liquid column is about to pinch off.

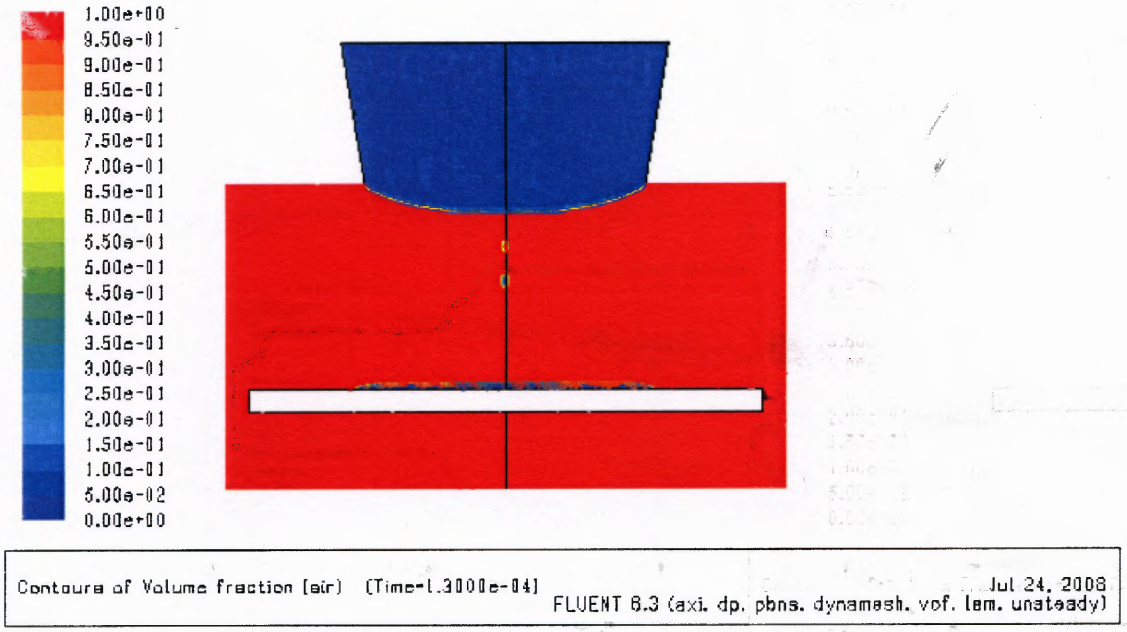

(f) One moment after liquid spot is formed.

Figure 5.10 Snapshots of critical states of liquid dispensing process simulation, (e) and (f).

5.6 Comparison Between Simulation and Experiment Results

The simulation results show that for a pulled glass pin of 60 um orifice and 9.46 degrees of taper angle, when filled with water which forms a 10 um height liquid bulge, can leave a 63.38 um (time= 13 us) spot on glass slide, as shown in Figure 5.11 (a), while the spot size in the experiment is 61 um as shown in Figure 5.11 (b).

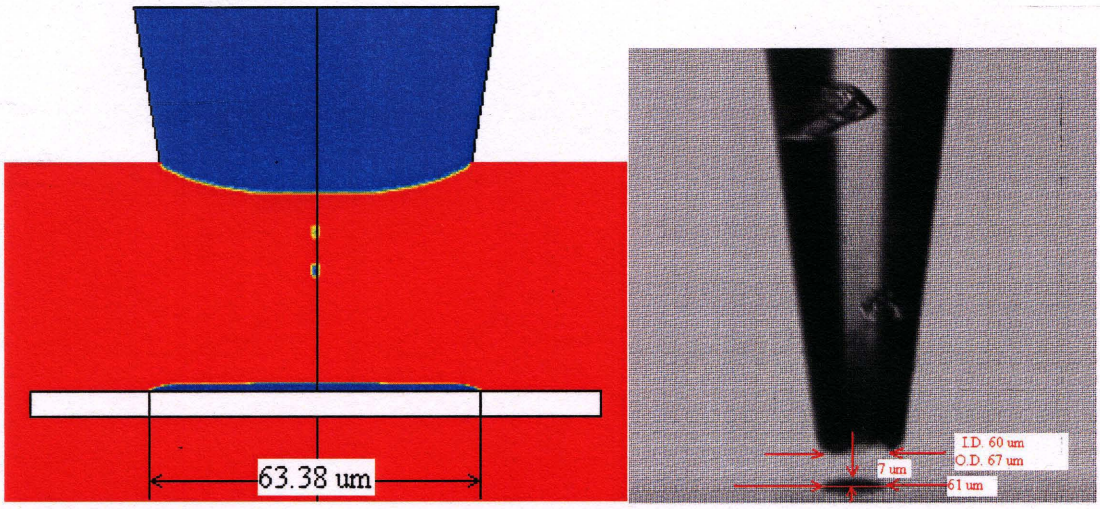

(a) (b)

Figure 5.11 Comparison of spot size.

The volume of the spot in simulation can be calculated easily from the moment when the liquid column is about to pinch off as shown in Figure 5.12 (b), which is about 6.88 pico-liter. The spot volume in experiment shown in Figure 5.11 (b) is about 10 pico-liter.

The liquid column elongates about 21.25 um until it pinch off in the simulation (time = 62.5 us) as shown in Figure 5.12. The maximum elongation of the liquid column in the experiment (shown in Figure 5.13) is 23 um.

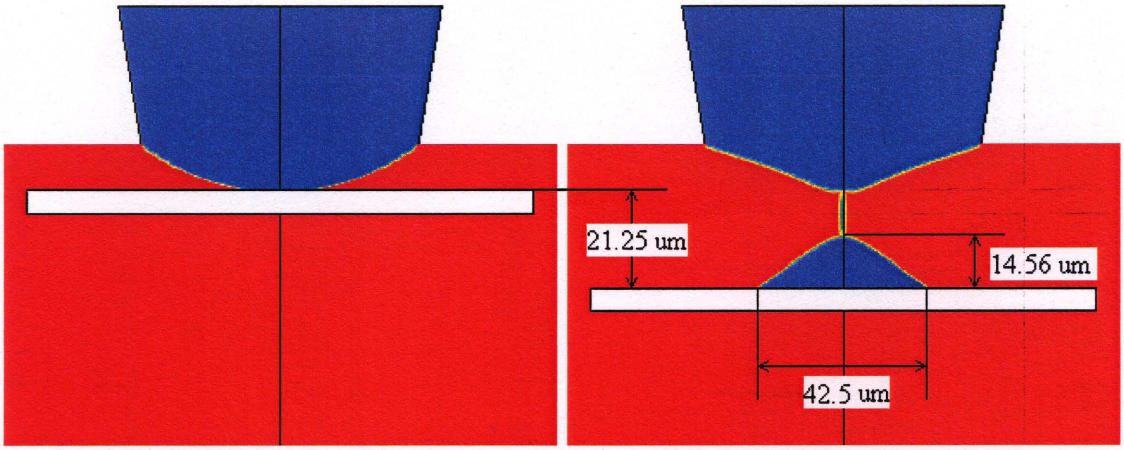

Figure 5.12 Simulation states used for calculation.

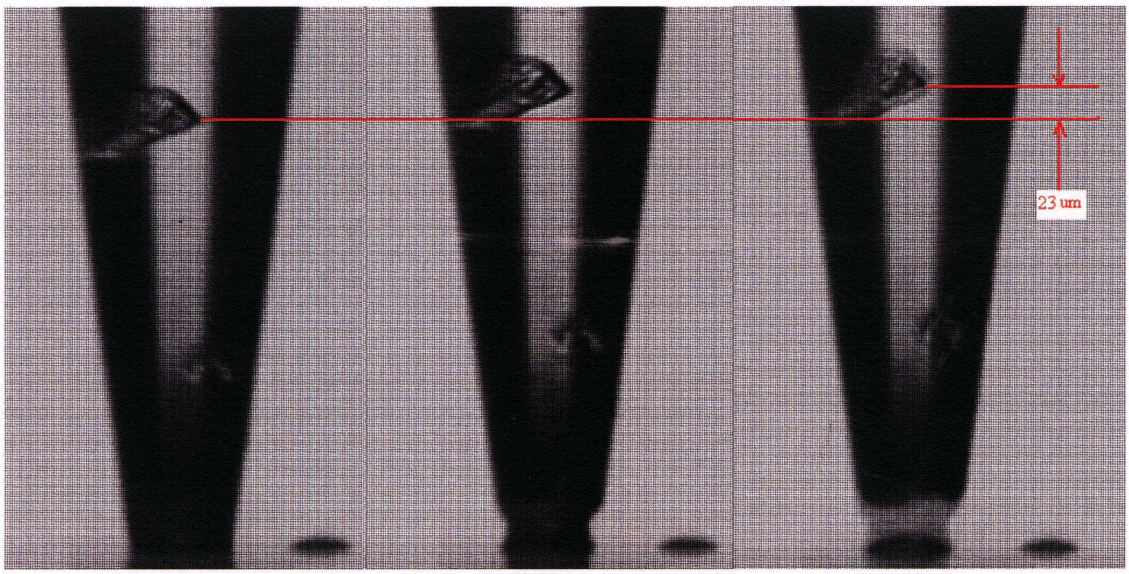

Figure 5.13 Images captured from experiment during liquid column elongation.

As one advantage of CFD simulation, prediction on trends of characteristic data versus critical parameters is of importance. In this work, orifice of the glass pin tip is an important parameter which effects the elongation of liquid column, the spot size, and the liquid volume consumed on each spot. To study the scalability and order of change on these data, simulations of liquid dispensing process with different sized glass pin tip were carried out.

Figures 5.14 and 5.15 show the initial, pinch-off, and final states of liquid dispensing process with glass pins of 30 um and 120 um orifices, respectively. The liquid material is water, and the heights of the liquid bulge at the glass pin tip are the same (10 um) in these two simulations. Figures 5.16, 5.17, and 5.18 show the trends on liquid column elongation, spot size, and liquid volume versus orifice of the glass pin. Finally, the time information revealed by the simulation give us reference on the design of real-time control system.

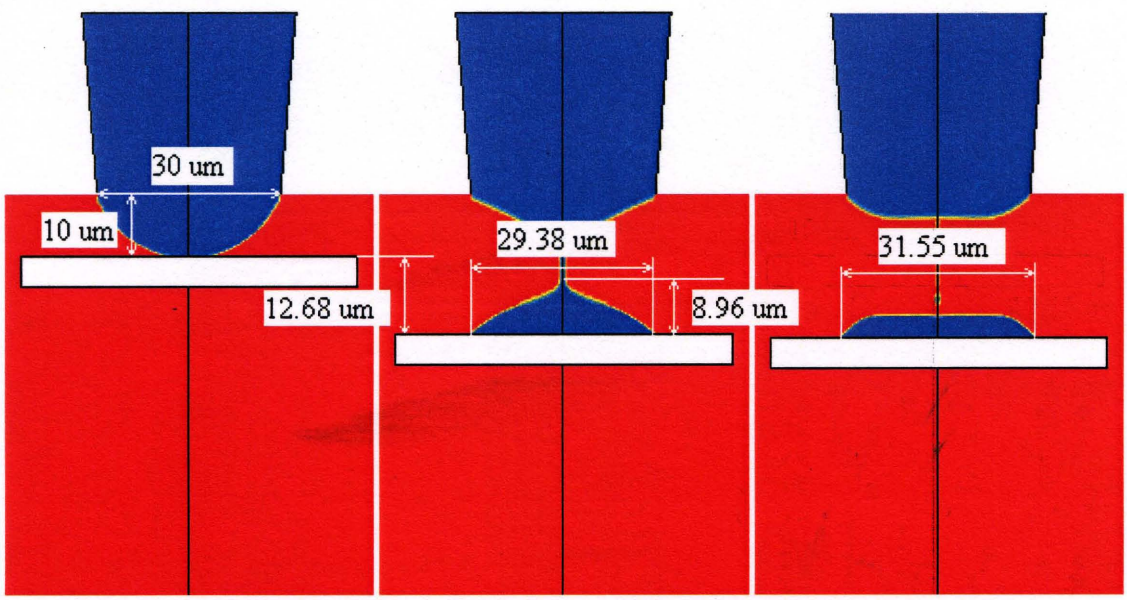

Figure 5.14 Initial, pinch-off, and final state of liquid dispensing process with glass pin of 30 um orifice.

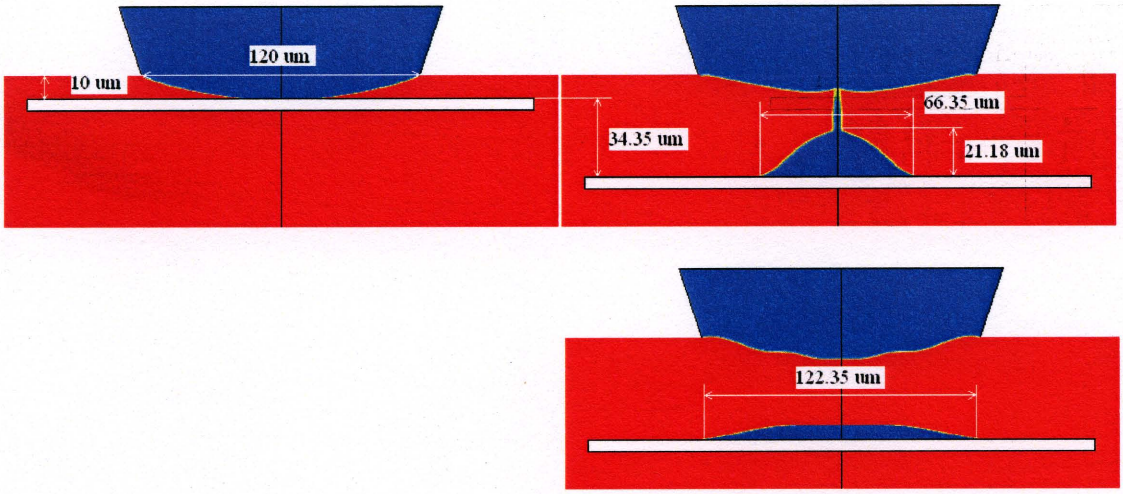

Figure 5.15 Initial, pinch-off, and final state of liquid dispensing process with glass pin of 120 um orifice.

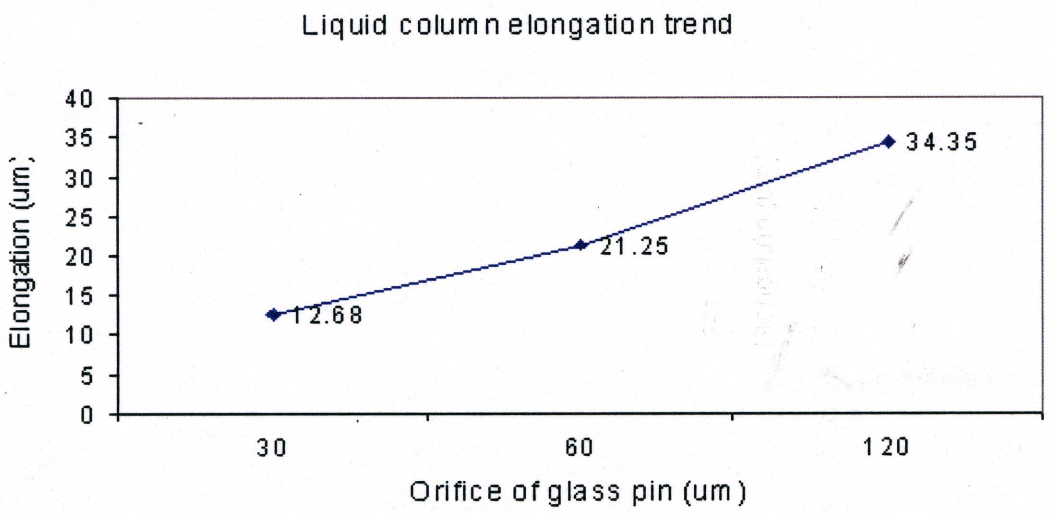

Figure 5.16 Liquid column elongation vs. orifice of glass pin.

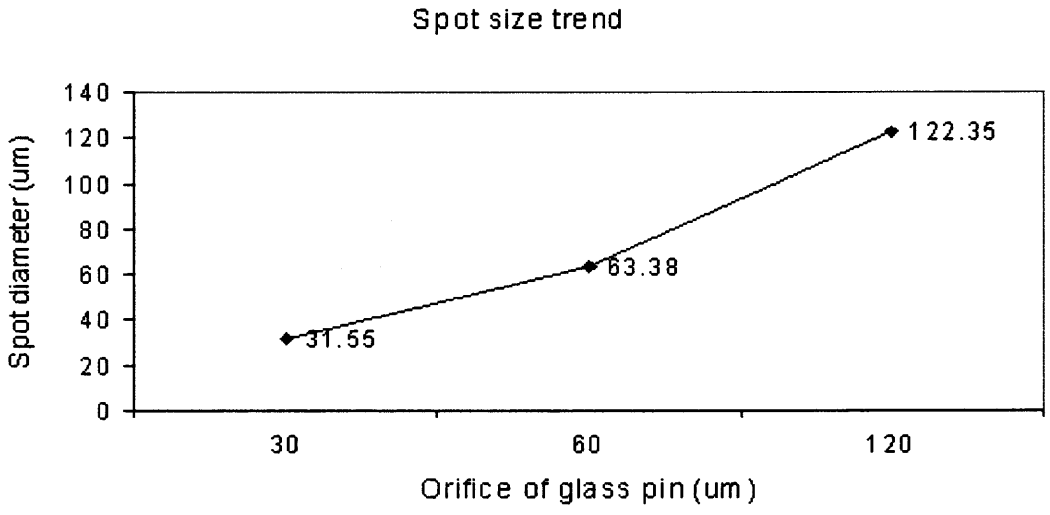

Figure 5.17 Spot size vs. orifice of glass pin.

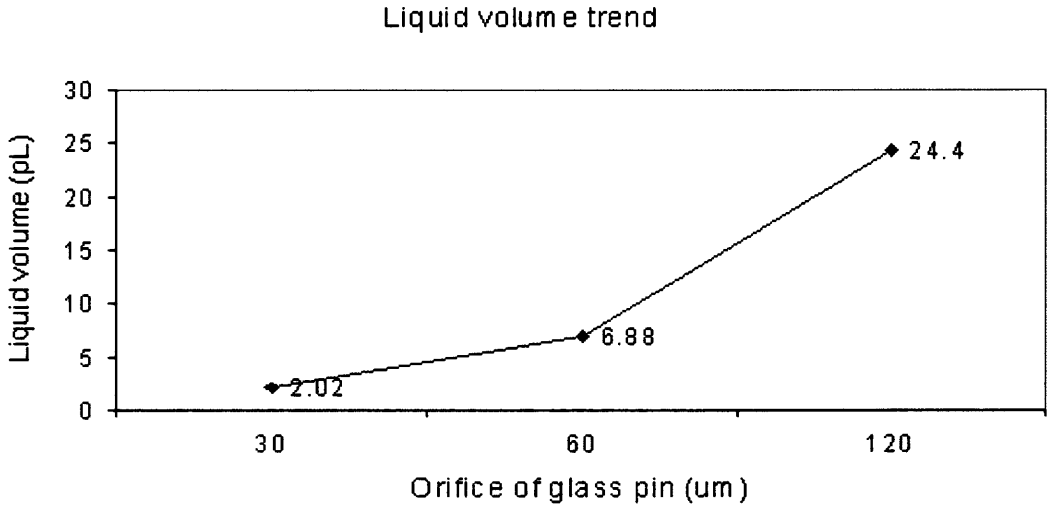

Figure 5.18 Liquid volume vs. orifice of glass pin.

5.7 Discussion

The errors between the simulation results are due to:

1. There exists difference between the simplified dynamics of the glass slide defined by the UDF and the real dynamics of the glass slide.

2. The physical properties of the liquid, such as density, viscosity, the surface tension between the liquid and air, and the contact angle between the liquid and the PLL coated glass slide, are not obtained from strict measurements but standard values of pure water.

3. The particles (salt, Cy-3 dye) in the real 3xSSC buffer solution play roles in affecting the dynamics of the fluid.

Despite the errors, the simulation does give us some insights into the liquid dispensing process which happens so quickly that normal equipments cannot capture. And when parameters (physical properties of the liquid, geometry of the pin) change, the simulation can give us predictive information of the trend and order of change of characteristics of the liquid dispensing process such as on the spot size, spot volume, and elongation time.

CHAPTER 6

CONCLUSIONS AND FUTURE WORK

In this doctoral research, an automated liquid dispensing system is designed, implemented, and tested for applications in life science, semiconductor manufacturing, and nanotechnology. Application of SmartPin technology in DNA microarray fabrication offers exciting prospects for the medical and life science fields. This technology makes it possible to print hundred thousands of DNA samples on one microscope slide. Such high density deposition enables reliable, simultaneous analysis of genes for such applications as drug discovery, cancer research, and disease diagnosis. With the work done in this thesis, the effort to realize the SmartPin technology as a practical way of printing has been advanced. With the spot classification system developed in this thesis, the quantitative analysis of the spots morphology can be done in real time and to determine whether if a spot needs re-deposition. Using the intensity data of the SmartPin sensor, a spot can be determined in situ, to be acceptable or being in need of being reprinted. While the criteria for this classification need to be refined so that a more accurate assessment of each spot can be done, the intermediate data thus far have supported the feasibility of the method described in this thesis.

In this work, an improved pin assembly is integrated with various high precision components and fixtures. A constant humidity-temperature clean chamber has been designed and built to create optimal operating conditions for the system. Significant feature improvements include: sealed reservoir at the tapered pin tip, strong mechanical support for plastic optical fiber, isolation of the Fotonic sensor from the positioning system, and easily adjustable position of the glass pin. All such improvement/innovations

lead to a fully automated DNA microarrayer platform. Multiple time-scale, hierarchical software integration implements the complete procedure of DNA microarray fabrication such as cleaning of the pin tip to avoid cross contamination and clogging, aspiration of tiny amount of DNA samples from standard micro-well plate, spotting on multiple slides with constant amount of liquid dispensing, and change of DNA samples without operator intervention..

Various experimental verifications have been carried out. For the DNA microarray applications, experiments on 14 oligonucleotides have been carried out under the same fabrication protocol as using OmniGrid 100 with SMP3 which is a standard contacting printing system. The hybridization results show that the SmartPin is superior to the Omnigrid in morphology, signal to noise ratio, and intensity. Spotting of 120 K spots has been done to demonstrate the robustness and high-volume capability of this SmartPin microarrayer. A large number of data were also collected, analyzed to form template database for curve fitting and real time diagnostics. The microline drawing capability of the SmartPin has been explored by implementing spot sequence and liquid-column sweeping methods to draw both simple straight lines and framed square boxes. By utilizing CFD softwares, transient states of liquid bulge deformation, liquid column elongation, liquid column pinch-off were discovered. After being validated by experiment results on water, multiple simulation results reveal the trend of liquid elongation, spot size, and liquid volume versus orifice of glass pin. Theses trends can guide the design of control system on real-time requirement, system identifications. The CFD simulation can also be used to discover effects of different liquid material on the elongation, spot size, and liquid volume.

Nevertheless, the current implementation is not a hard real-time system. In another word, the current system is not able to manipulate the spot formation which takes place in order of micro seconds.

Future work includes:

- Definition and analysis of characteristic number representing effects of liquid properties on spotting.
- Improve hard-realtime performance by utilizing DSP platform.
- Find out more efficient system identification algorithm.

APPENDIX A

SOURCE CODE OF UDF DEFINING MOTION OF THE GLASS SLIDE

This appendix lists the source code of the UDF defining motion of the glass slide.

```
/*
   File name: moving_slide.c
   This program will be executed by the FLUENT solver at each iteration
   of computation.
*/
#include "udf.h"           /* Necessary for using predefined macros. */
#define BULGE_TIP 1e-5     /* The height of liquid bulge is 10 um.   */
#define LOWER_BOUND 5.4e-5 /* Lower limit of slide motion is 54 um.  */
#define TOUCH_TIME 2e-5    /* 20 us for liquid bulge to deform.      */
#define PZT_SPEED 0.5      /* Velocity of glass slide is 0.5 m/s     */

/*
   DEFINE_CG_MOTION is a predefined macro which will be expanded into
   Void UDFslide(Dynamic_Thread *dt, real vel[], real omega[],
                 real time, real dtime);
   where
      dt contains information of all grids.
      vel[] and omega[] are linear and angular velocities of the moving
            part about it's center of gravity.
      time is current time of simulation.
      Dtime is step size of time for iteration.
*/
DEFINE_CG_MOTION(UDFslide,dt,vel,omega,time,dtime)
{
  /*
      motion_state = 0: Glass slide is initially stationery.
      motion_state = 1: Transition of liquid bulge deformation
                        finishes, and glass slide starts to move away
                        from pin tip.
  */
  static int motion_state=0;
  static real touch_moment=-1.0; /* The time stamp when glass touches
                                    the liquid bulge. */
  real NV_VEC(vecCG);            /* Define a vector.  */

  /* Since the time/dtime equals number of iteration, the following
     "if" condition block is executed once in the very first iteration.
  */
  if ((time/dtime) < 2.0) {
      NV_S(vel, =, 0.0);
      motion_state = 0;
      touch_moment = time;
      Message("Initialized successfully.\n");
  }
  NV_S(omega, =, 0.0);       /* No angular velocity for glass slide. */
  NV_V(vecCG, =, DT_CG(dt)); /* Retrieve and validate information of
                                The center of gravity.               */
```

```
    if (!Data_Valid_P()) {    /* If errors in retrieving, terminate.  */
        return;
    }

    switch (motion_state) {
    case 0:
        if ((time - touch_moment) < TOUCH_TIME) { /* In transition of
                                                     liquid bulge deformation. */
                    vel[0] = 0.0;
        } else {                          /* End of liquid bulge
                                             deformation period is the
                                             beginning of the glass slide
                                             departure.    */
                    vel[0] = PZT_SPEED;
                    motion_state = 1;
                    Message("State changed to 1");
        }
        break;
    case 1:
        if (vecCG[0] < LOWER_BOUND) {     /* Within range, glass slide
                                             is moving away from pin tip. */
                    vel[0] = PZT_SPEED;
        } else {                          /* Reach lower limit, glass
                                             slide stops moving. */
                    vel[0] = 0.0;
                    Message("Touch the bottom");
        }
        break;
    default:
        break;
    }
}
```

APPENDIX B

ORGANIZATION OF SOURCE CODE FILES OF CONTROL SYSTEM SOFTWARE

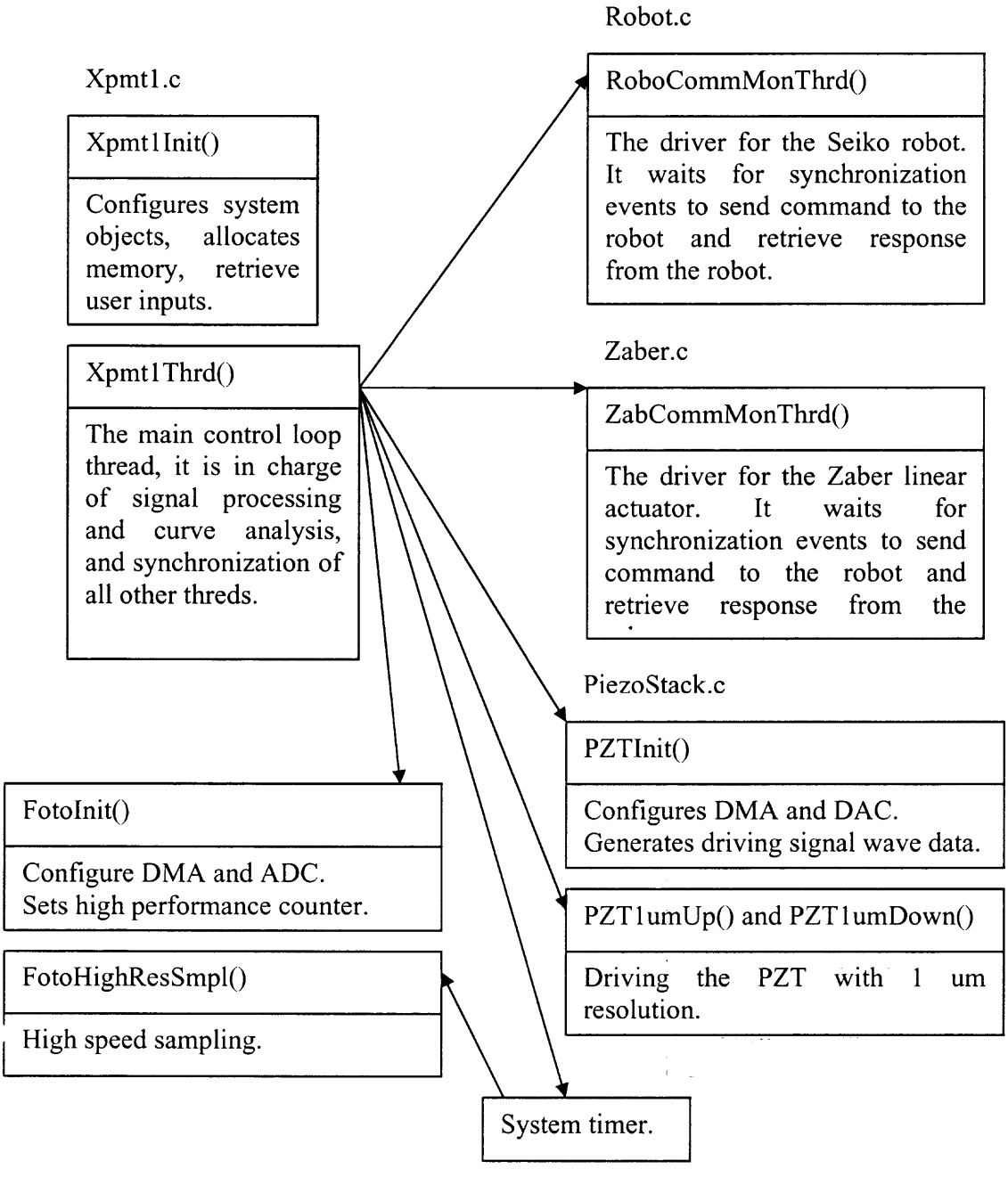

Figure B.1 Organization of source code files of control system software.

REFERENCES

1. Bao, Z., Feng, Y., Dodabalapur, A., Raju, V. R., & Lovinger, A. J. (1997). High-performance plastic transistors fabricated by printing techniques, Chemistry of Materials, Vol. 9, 1299-1301.

2. Bayer, I. S. & Megaridis, C. M. (2006). Contact angle dynamics in droplets impacting on flat surfaces with different wetting characteristics, Journal of Fluid Mechanics, Vol. 558, 415-449.

3. Belblidia, F., Matallah, H., & Webster, M. F. (2008). Alternative subcell discretisations for viscoelastic flow: Velocity-gradient approximation, Journal of Non-Newtonian Fluid Mechanics, Vol. 151, 69-88.

4. Bharathan, J. & Yang, Y. (1998). Polymer electroluminescent devices processed by inkjet printing: I. Polymer light-emitting logo, Applied Physics Letters, Vol. 72, 2660-2662.

5. Blanchard, A. P., Kaiser, R.J., & Hood, L. E. (1996). High-Density Olibonucleotide Arrays, Biosensors & Bioelectronics, Vol. 11, 687-690.

6. Blanchet, G. B., Fincher, C. R., & Gao, F. (2003). Polyaniline nanotube composites: A high-resolution printable conductor, Applied Physics Letters, Vol. 82, 1290-1292.

7. Blanchet, G. B., Loo, Y.-L., Rogers, J. A., Gao, F., & Fincher, C. R. (2003). Large area, high resolution, dry printing of conducting polymers for organic electronics, Applied Physics Letters, Vol. 82, 463-465.

8. Calvert, P. (2001). Inkjet Printing for Materials and Devices. Chemistry of Materials, Vol. 13, 3299-3305.

9. Catalog, Physik Instrumente GmbH & Co. KG, 2008.

10. Catalog Master Source Book, Edmund Optics Inc., 2007.

11. Chang, T.N., Parthasarathy S., Wang, T., Gandhi, K., & Soteropoulos, P. (2006). Automated liquid dispensing pin for DNA microarray applications, IEEE Transactions on Automation Science and Engineering, Vol. 3, 187-191.

12. Chang, T. N. & Tolias, P. (2006). U.S. Patent No. 7,097,810 B2, Delivery of metered amounts of liquid materials, Washington, D.C.:U.S. Patent and Trademark Office.

13. Chang, T. & Parthasarathy, S. (2003). NSF Award No. 0243302, High Resolution, High Density Microarrayer for Genetic Research, Arlington, Virginia: The National Science Foundation.

14. Chen, X. B., Schoenau, G., & Zhang, W. J. (2000). Modeling of time-pressure fluid dispensing processes, IEEE Transactions on Electronics Packaging Manufacturing, Vol. 23, 300-305.

15. Chung, J., Ko, S., Grigoropoulos, C.P., Bieri, N.R., Dockendorf, C., & Poulikakos D. (2005). Damage-Free Low Temperature Pulsed Laser Printing of Gold Nanoinks On Polymers, Transactions of the ASME, Vol. 127, 724-732.

16. Chung, G. Y., Park, S. C., Cho, K., & Ahn, B. T. (1995). Electrical properties of CdTe films prepared by close-spaced sublimation with screen printed source layers, Journal of Applied Physics, Vol. 78, 5493-5498.

17. Cooley, P., Wallace, D., & Antohe, B. (2001). Proceedings, Proceedings of Society of Photographic Instrumentation Engineers Conference on Microfludics and BioMEMS, Vol. 4560, 177-188.

18. Crone, B., Dodabalapur, A., Sarpshkar, R., Gelperin, A., Katz, H. E., & Bao, Z. (2002). Organic oscillator and adaptive amplifier circuits for chemical vapor sensing, Journal of Applied Physics, Vol. 91, 10140-10146.

19. DAQ-PCI E Series Register Level Programmer Manual, National Instrument Corp., 1998.

20. DAQ-STC Technical Reference Manual, National Instruments Corp., 1998.

21. Decre, M. M. J., Schneider, R., Burdinski, D., Schellekens, J., Saalmink, M. & Dona, R. (2004). Wave printing (I): Toward large-area, multilayer microcontact printing, Proceedings of Materials Research Society, Vol. EXS-2, M4.9.1-M4.9.3.

22. Deng, G. & Zhong, J. (2006). Analysis and modeling non-Newtonian fluid transferring process and dot formation in contact dispensing, Proceedings of Conference on High Density Microsystem Design and Packaging and Component Failure Analysis, 4017382.

23. de Wildt, R. M., Mundy, C.R., Gorick, B. D., & Tomlinson, I. M. (2000). Antibody arrays for high-throughput screening of antibody-antigen interactions. Nature Biotechnology, Vol. 18, 989-994.

24. Dhingra, I., Padam, G. K., Singh, S., Tripathy, R. B., Rao, S. U. M., Suri, D. K., Nagpal, K. C., & Das, B. K. (1991). Study of silver addition to YBaCuO screen printed thick films, Journal of Applied Physics, Vol. 70, 1575-1579.

25. Ding, H. & Spelt, P. D. M. (2007). Inertial effects in droplet spreading: a comparison between diffuse-interface and level-set simulations, Journal of Fluid Mechanics, Vol. 576, 287-296.

26. Duthaler, G. (1995). Design of a drop-on-demand delivery system for molten solder microdrops, Master's thesis at MIT.

27. Edzer, H. E., Huitema, A., Gelinck, G. H., Bas, J., van der Putten, P. H., Kuijk, K. E., Hart, K. M., Cantatore, E., & de Leeuw, D. M. (2002). Active-matrix displays driven by solution-processed polymeric transistors, Advanced Materials, Vol. 14, 1201-1204.

28. Elrod, S. A., Hadimioglu, B., Khuri-Yakub, B. T., Rawson, E. G., Richley, E., & Quate, C. F. (1989). Nozzleless droplet formation with focused acoustic beams, Journal of Applied Physics, Vol. 65, 3441-3447.

29. Fejzo, M.S. & Slamon, D. J. (2001). Frozen tumor tissue microarray technology for analysis of tumor RNA, DNA, and proteins, American Journal of Pathology, Vol. 159, 1645-1650.

30. Fuchikami, N., Ishiokal, S., & Kiyono, K. (1999). Simulation of a Dripping Faucet, Journal of Physics Society of Japan, Vol. 68, 1185-1196.

31. Fuller, S.B., Wilhelm, E.J., & Jacobson, J.M. (2002). Ink-jet printed nanoparticle micro-electro-mechanical systems, Journal of Micro-Electro-Mechanical Systems, Vol. 11, 54-60.

32. Garnier, F., Hajlaoui, R., Yassar, A., & Srivastava, P. (1994). All-polymer field-effect transistor realized by printing techniques, Science, Vol. 256, 1684-1686.

33. Gelinck, G. H., Geuns, T. C. T., & de Leeuw, D. M. (2000). High-performance all-polymer integrated circuits, Applied Physicis Letters, Vol. 77, 1487-1489.

34. Gray, C., Wang, J., Duthaler, G., Ritenour, A., & Drzaic, P. (2001). Screen printed organic thin film transistors (OTFT's) on a flexible substrate, Proceedings of Society of Photographic Instrumentation Engineers, Vol. 4466, 89-94.

35. Hayes, D. J., Grove, M. E., Wallace, D. B., Chen, T., & Cox, W. R. (2002). Ink-jet printing in the manufacturing of electronics, photonics, and displays, Proceedings of Society of Photographic Instrumentation Engineers, Vol. 4809, 94-99.

36. Hayes, D. J., Cox, W. R., & Wallace, D. B. (2001). Printing system for MEMS packaging, Proceedings of Society of Photographic Instrumentation Engineers Conference, Vol. 4558, 206-214.

37. Hayes, D. J., Wallace, D. B., & Boldman, M. T. (1992). Picoliter solder droplet dispensing, Proceedings of Integrated Systems Health Management Conference, 1-6.

38. Hayes, D. J., Cox, W. R., & Grove, M. E. (1998). Microjet printing of polymers and solder for electronics manufacturing, Journal of Electronics Manufacturing, Vol. 8, 209-216.

39. Hebner, T. R., Wu, C. C., Marcy, D., Lu, M. H., & Sturm, J. C. (1998). Ink-jet printing of doped polymers for organic light emitting devices, Applied Physics Letters, Vol. 72, 519-521.

40. Hicks, J. S., Harker, B. W., Beattie, K. L., & Doktycz, M. J. (2001). Modification of an automated liquid handling system for reagent-jet, nanoliter-level dispensing, Biotechniques, Vol. 30, 878-885.

41. Hong, Y. -P. & Li, H. -X. (2003). Comparative study of fluid dispensing modeling, IEEE Transactions on Electronics Packaging Manufacturing, Vol. 26, 273-280.

42. Hughes, T. R, Mao, M., Jones, A. R., Burchard, J., Marton, M. J., Shannon, K. W., Lefkowitz, S. M., Ziman, M., Shcelter, J. M., Meyer, M. R., Kobayashi, S., Davis, C., Dai, H., He, Y. D., Stephaniants, S. B., Cavet, G., Walker, W. L., West, A., Coffey, E., Shoemaker, D. D., Stoughton, R., Blanchard, A. P., Friend, S. H., & Linsley, P. S. (2001). Expression profiling using microarrays fabricated by an ink-jet oligonucleotide synthesizer, Nature Biotechnology, Vol. 19, 342-347.

43. Instruction Manual of SEIKO D-TRAN Robot, Seiko Corp., 1990.

44. Instruction Manual of MTI 2100 Fotonic Sensor, MTI Instruments Inc., 2007.

45. Jackson, T. N., Lin, Y. Y., Gundlach, D. J., & Klauk, H. (1998). Organic thin-film transistors for organic light-emitting flat-panel display backplanes, IEEE Journal of Selected Topics in Quantun Electronics, Vol. 4, 100-104.

46. Kawase, T., Sirringhaus, H., Friend, R. H., & Shimoda, T. (2001). Inkjet printed via-hole interconnections and resistors for all-polymer transistor circuits, Advanced Materials, Vol. 13, 1601-1605.

47. Kawase, T., Sirringhous, H., Friend, R.H., & Shimoda, T. (2001). All polymer thin film transistors fabricated by inkjet printing, Proceedings of Society of Photographic Instrumentation Engineers, Vol. 4466, 80-88.

48. Kerboua, Y., Lakis, A. A., Thomas, M., & Marcouiller, L. (2008). Computational modeling of coupled fluid-structure systems with applications, Structural Engineering and Mechanics, Vol. 29, 91-111.

49. Khatavkar, V. V., Anderson, P. D., & Meijer H. E. H. (2007). Capillary spreading of a droplet in the partially wetting regime using a diffuse-interface model, Journal of Fluid Mechanics, Vol. 572, 367-387.

50. Kim, H. -Y. & Chun, J. -H. (2001). The recoiling of liquid droplets upon collision with solid surfaces, Physics of Fluids, Vol. 13, 643-659.

51. Knobloch, A., Bernds, A., & Clemens, W. (2001). Printed polymer transistors, Proceedings of Polytronic, Vol. 1, 0-7803-7220-4.

52. Korlie, M. S., Mukherjee, A., Nita, B. G., Stevens, J. G., Trubatch, A. D., & Yecko, P. (2008). Modeling bubbles and droplets in magnetic fluids, Journal of Physics Condensed Matter, Vol. 20, 204143.

53. Krogmann, F., Qu, H., Moench, W., & Zappe, H. (2006). Light-Actuated Push/Pull Manipulation of Liquid Droplets, IEEE/LEOS International Conference on Optical MEMS and Their Applications, Vol. 1, 175-176.

54. Kumar, A. & Whitesides, G.M. (1993). Features of gold having micrometer to centimeter dimensions can be formed through a combination of stamping with an elastomeric stamp and an alkanethiols 'ink' followed by chemical etching, Applied Physics Letters, Vol. 63, 2002-2004.

55. Lahiri, J., Jonas S. J., Frutos, A.G., Kalal, P., & Fang, Y. (2001). Lipid Microarrays. Biomedical Microdevices, Vol. 3, 157-164.

56. Lam, K. S. & Renil, M. (2002). From combinatorial chemistry to chemical microarray. Current Opinion in Chemical Biology, Vol. 6, 353-361.

57. Lefenfeld, M., Blanchet, G., & Rogers, J. A. (2003). High-performance contacts in plastic transistors and logic gates that use printed electrodes of DNNSA-PANI doped with single-walled carbon nanotubes, Advanced Materials, Vol. 15, 1188-1191.

58. Le, H. P. (1998). Progress and Trends in Ink-jet Printing Technology. Journal of Imaging Science and Technology, Vol. 42, 49-62.

59. Leufgen, M., Lebib, A., Muck, T., Bass, U., Wagner, V., Borzenko, T., Schmidt, G., Geurts, J., & Molenkamp, L. W. (2004). Organic thin-film transistors fabricated by microcontact printing, Applied Physics Letters, Vol. 84, 1582-1584.

60. Loo, Y.-L., Willet, R. L., Baldwin, K.W., & Rogers, J. A. (2002). Interfacial chemistries for nanoscale transfer printing, Journal of the American Chemical Society, Vol. 124, 7654-7655.

61. Loo, Y.-L., Willet, R. L., Baldwin, K.W., & Rogers, J. A. (2002). Additive, nanoscale patterning of metal films with a stamp and a surface chemistry mediated transfer process: Application in plastic electronics, Applied Physics Letters, Vol. 81, 562-564.

62. Love, K. R. & Seeberger, P. H. (2002). Carbohydrate arrays as tools for glycomics. Applied Chemistry, International Edition, English, Vol. 41, 3583-3589, 3513.

63. Lu, J., Pinto, N. J., & MacDiarmid, A. G. (2002). Apparent dependence of conductivity of a conducting polymer on an electric field in a field effect transistor configuration, Journal of Applied Physics, Vol. 92, 6033-6038.

64. MacDiarmid, A. G. (2001). A novel role for organic polymers, Review of Modern Physics, Vol. 73, 701-712.

65. Matallah, H., Sujatha, K. S., Banaai, M. J., & Webster, M. F. (2007). Single and multi-mode modeling for filament stretching flows, Journal of Non-Newtonian Fluid Mechanics, Vol. 146, 92-113.

66. Matallah, H., Banaai, M. J., Sujatha, K. S., & Webster, M. F., (2006). Modelling filament stretching flows with strain-hardening models and sub-cell approximations, Journal of Non-Newtonian Fluid Mechanics, Vol. 134, 77-104.

67. Mikami, Y., Nagae, Y., Mori, Y., Kuwabara, K., Saito, T., Hayama, H., Asada, H., Akimoto, Y., Kobayashi, M., Okazaki, S., Asaka, K., Matsui, H., Nakamura, K., & Kaneko, E. (1994). A new patterning process concept for large-area transistor circuit fabrication without using an optical mask aligner, IEEE Transactions on Electron Devices, Vol. 41, 306-314.

68. Molesa, S., Redinger, D. R., Huang, D. C., & Subramanian, V. (2003). Highquality inkjet-printed multilevel interconnects and inductive components on plastic for ultra-low-cost RFID applications, Proceedings of Material Research Society Symposium, Vol. 769, H8.3.1-H8.3.6.

69. Muller, U.R. & Nicolau, D.V. (2005). Microarray Technology and Its Applications. Springer-Verlag, Berlin, Heidelberg.

70. Papen, R., Croker, K., & Kolb, A. (1998). Nanoliter Dispensing Technology. Genetic Engineering News, Vol. 18, 14-18.

71. Parashkov, R., Becker, E., Riedl, T., Johannes, H. -H., & Kowalsky, W. (2005). Large Area Electronics Using Printing Methods, Proceedings of the IEEE, Vol. 93, 1321-1329.

72. Parashkov, R., Becker, E., Riedl, T., Johannes, H.-H., & Kowalsky, W. (2005). Microcontact printing as a versatile tool for patterning organic field-effect transistors, Advanced Materials, Vol. 17, 1527-1531.

73. Parthasarathy, S. (2005). Automated Liquid Dispensing Pin for DNA Microarray Application, Master's Thesis at NJIT.

74. Paul, K. E., Wong, W. S., Ready, S. E., & Street, R. A. (2003). Additive jet printing of polymer thin-film transistors, Applied Physics Letters, Vol. 83, 2070-2072.

75. Perçin, G., Lundgren, T. S., & Khuri-Yakub, B. T. (1998). Controlled ink-jet printing and deposition of organic polymers and solid particles, Applied Physics Letters, Vol. 73, 2375-2377.

76. Priest, J., Jacobs, E., Smith, Jr., C., DuBois, P., Holt, B., & Hammerschlag, B. (1994). Liquid metal-jetting technology: Application issues for hybrid technology, International Journal of Microcircuits and Electronic Packaging, Vol. 17, 219-227.

77. Purvis, R. & Smith, F. T. (2004). Air-water interactions near droplet impact, European Journal of Applied Mathematics, Vol. 15, 853-871.

78. Reznik, S. N., & Yarin, A. L. (2002). Spreading of a viscous drop due to gravity and capillarity on a horizontal or an inclined dry wall, Physics of Fluids, Vol. 14, 118-132.

79. Ridley, B. A., Nivi, B., & Jacobson, J. M. (1999). All-inorganic field effect transistors fabricated by printing, Science, Vol. 286, 746-749.

80. Roda, A., Guardigli, M., Russeo, C., Pasini, P., & Baraldini, M. (2000). Protein Microdeposition Using A Conventional Ink-Jet Printer. BioTechnigues, Vol. 28, 492-496.

81. Rogers, J. A., Bao, Z., Makhija, A., & Braun, P. (1999). Printing process suitable for reel-to-reel production of high-performance organic transistors and circuits, Advanced Materials, Vol. 11, 741-745.

82. Rozenberg, G.G., Bresier, E., Speakman, S.P., Jeynes, C., & Steinke, J.H.G. (2002). Patterned low temperature copper-rich deposits using inkjet printing, Applied Physics Letters, Vol. 81, 5249-5251.

83. Schellekens, J., Burdinski, D., Saalmink, M., Beenhakkers, M., Gelinck, G., & Decre, M. M. J. (2004). Wave printing (II): Polymer MISFET's using microcontact printing, Proceedings of Materials Research Society Symposium, Vol. EXS-2, M2.9.1-M2.9.3.

84. Schena, M., Shalon, D., Davis, R. W., & Brown, P. O. (1995). Quantitative monitoring of gene expressionpatterns with a complementary DNA microarray, Science, Vol. 270, 467-470.

85. Schweitzer, B. & Kingsmore, S. F. (2002). Measuring proteins on microarrays, Current Opinion in Biotechnology, Vol. 13, 14-19.

86. Sirringhaus, H., Kawase, T., Friend, R.H., Shimoda, T., Inbasekaran, M., Wu, W., & Woo, E.P. (2000). High-resolution inkjet printing of all-polymer transistor circuits, Science, Vol. 290, 2123-2126.

87. Sujatha, K. S., Matallah, H., Banaai, M. J., & Webster, M. F. (2008). Modeling step-strain filament-stretching (CaBER-type) using ALE techniques, Journal of Non-Newtonian Fluid Mechanics, Vol. 148, 109-121.

88. Sujatha, K. S., Matallah, H., Banaai, M. J., & Webster, M. F. (2006). Computational predictions for viscoelastic filament stretching flows: ALE methods and free-surface techniques (CM and VOF), Journal of Non-Newtonian Fluid Mechanics, Vol. 137, 81-102.

89. Szczech, J.B., Megaridis, C.M., Gamota, D.R., & Zhang J. (2002). Fine-Line Conductor Manufacturing Using Drop-On-Demand PZT Printing Technology, IEEE Transactions on Electronics Packaging Manufacturing, Vol. 25, 26-33.

90. Teng, K. F. & Vest, R.W. (1988). Application of ink jet technology on photovoltaic metallization, IEEE Electron Device Letters, Vol. 9, 591-592.

91. Teng, K. F. & Vest, R.W. (1988). A microprocessor-controlled ink jet printing system for electronic circuits, IEEE Transactions on Industrial Electronics, Vol. 35, 407-412.

92. T-Series Positioning Products User's Manual. Zaber Technologies Inc., 2007.

93. Tsumura, A., Koezuka, H., & Ando, T. (1996). Macromolecular electronic device: Field effect transistor with a polythiophenes thin film, Applied Physics Letters, Vol. 49, 1210-1212.

94. Valencia, S., Castano, O., Fontcuberta, J., Martinez, B., & Balcells, L. (2003). Enhanced low field magnetoresistive response in (LaSrMnO)=(CeO) composite thick films prepared by screen printing, Journal of Applied Physics, Vol. 94, 2524-2528.

95. Walton, A. J., Stevenson, J. T. M., Haworth, L. I., Fallon, M., Evans, P. S. A., Ramsey, B. J., & Harrison, D. (1999). Characterization of offset lithographic films using microelectronic test structures, The Institute of Electronics,